Short-Term Climatic Fluctuations Forced by Thermal Anomalies

by
Adel Fahim Hanna

Department of Atmospheric Science
Colorado State University
Fort Collins, Colorado

Colorado State University

Department of Atmospheric Science

Paper No. 360

SHORT-TERM CLIMATIC FLUCTUATIONS

FORCED BY THERMAL ANOMALIES

by

Adel Fahim Hanna

Research supported by the
Department of Energy under grant
DE-AS02-76EV01340 and the
National Aeronautics and Space Administration
under grant NAG 5-136
and the National Science Foundation
under grant ATM-80-16867

Department of Atmospheric Science
Colorado State University
Fort Collins, Colorado

November 1982

Atmospheric Science Paper No. 360

ABSTRACT

SHORT-TERM CLIMATIC FLUCTUATIONS

FORCED BY THERMAL ANOMALIES

The aim of this research is to study the response of the atmosphere to thermal anomalies using a low order spectral model. Thermal anomaly patterns may exist either in sea and land surface temperatures or in the tropospheric diabatic heating.

A two-level, global, spectral model using pressure as a vertical coordinate has been developed. The system of equations describing the model is nonlinear and quasi-geostrophic (linear balance). Static stability is variable in the model. A moisture budget is calculated in the lower layer only. Convective adjustment is used to avoid supercritical temperature lapse rates. The mechanical forcing of topography is introduced as a vertical velocity at the lower boundary. Solar forcing is specified assuming a daily mean zenith angle. The differential diabatic heating between land and sea is parameterized. On land- and sea-ice surfaces, a steady state thermal energy equation is solved to calculate the surface temperature. On the oceans, the sea surface temperature is specified as the climatological average for January. The model is used to simulate the January, February and March circulations.

Experiments are designed to study the response of the atmosphere to thermal anomalies at the lower boundary or in the midtroposphere. The "memory" in the atmosphere of such anomalies, after they have decayed,

is also studied. Three patterns of sea surface temperature anomalies are tested. The first pattern represents a cold anomaly in the North Pacific, the second a warm anomaly in the equatorial Pacific and the third pattern contains both of the two anomaly patterns acting together. The results suggest that the coupled pattern is the only one that produces the type of geopotential anomalies associated with the negative phase of the Southern Oscillation. In contrast to the results of linear models, warm sea surface temperature anomalies in the equatorial Pacific cannot produce such geopotential response on their own. In the case of this tropical anomaly pattern the variance of temperature resulting from transient eddies tends to increase, whereas in the case of the coupled anomaly pattern the variance of temperature resulting from stationary eddies increases. This behavior suggests that with both anomalies acting together the atmosphere is inclined to produce quasi-permanent responses, such as blocking, in contrast with the other case, in which the transient activity increases.

The mid-tropospheric anomaly is introduced as an easterly propagating wave over the equatorial Pacific and over the Gulf of Bengal. The amplitude and memory of the response is larger than for the sea surface temperature case. The mid-tropospheric thermal anomalies show continuous large areas of long memory in the subtropical and middle latitude regions of the Northern Hemisphere.

ACKNOWLEDGEMENTS

I am indebted to Dr. Duane E. Stevens for his guidance and supervision throughout this research and thesis preparation. I also would like to express my deep gratitude to Professor Elmar R. Reiter, my co-advisor, for his support, valuable discussions and the chance to complete my graduate studies in the United States. The cooperation and assistance of my committee members Professor Thomas H. Vonder Haar, Dr. Wayne H. Schubert and Professor Lewis L. Huff is highly appreciated.

The acknowledgement is also extended to Mr. Jan Behunek for editing and Mrs. Machel Sandfort for typing the manuscript.

Special thanks are due to my wife Suzan, and my sons Botrus and Hani for their encouragement during my graduate studies.

Computing time offered by the National Center for Atmospheric Research (NCAR) is gratefully acknowledged (NCAR is sponsored by the National Science Foundation).

This research was sponsored by the Department of Energy under grant DE-AS02-76EV01340 and the National Aeronautics and Space Administration under grant NAG 5-136 and the National Science Foundation under grant ATM-80-16867.

TABLE OF CONTENTS

LIST OF TABLES

LIST OF FIGURES

LIST OF SYMBOLS

a	radius of the earth
a_o	mean distance between the earth and the sun
a_s	instantaneous distance between the earth and the sun
AP	available potential energy
$(AP)_n^m$	spherical harmonic mode of AP
B	Stefan-Boltzmann constant
BG	Burger number
c	fractional amount of low and medium clouds (tenths)
c_d	surface drag coefficient
c_p	specific heat at constant pressure
D_n^m	$D_n^m = (n^2-m^2/4n^2-1)^{\frac{1}{2}}$
E	evaporation rate
f	the Coriolis parameter
F_h	rate of change of vorticity due to horizontal diffusion
F_v	rate of change of vorticity due to vertical diffusion
h_s	relative humidity near the surface
H	scale height of the atmosphere
H_o	hour angle of the sun
H_Q	height scale of the heat source
H_u	height scale of the zonal velocity
i	grid point zonal index, or $i = \sqrt{-1}$

I	thermal conductivity of ice per unit length
I_s	number of Guass latitudes applied in the transform method
j	grid point meridional index
J	highest wave number of n- m retained in the truncated series, or Jacobian
k	vertical unit vector
k_d	friction coefficient
k_h	lateral eddy diffusion coefficient
k_s	surface friction coefficient
KE	kinetic energy
$(KE)_n^m$	spherical harmonic mode of KE
ℓ	index of the vertical level
L	latent heat of condensation, or horizontal length scale
L_2	net long wave flux at 500 mb
L_3	net long wave flux at the top of the atmosphere
L_s	net long wave flux at the surface
m	zonal wave number
M	highest zonal wave number retained in the truncated series
$(M_o)_{ij}$	memory parameter at grid point (ij)
n	degree of a spherical harmonic component
N	number of days measured from day 0 to 00Z 1 January, or Brunt-Vaisala frequency
N_g	number of grid points used in an integration around a latitude circle
p	pressure
p_s	surface pressure
P_c	precipitation rate

P_n^m	associated Legendre functions of the first kind
q	moisture mixing ratio
q_s	saturation mixing ratio
Q	rate of heating per unit mass
Q_e	surface latent heat flux
Q_s	surface sensible heat flux
$(QL)_1$	heating rate by longwave radiation in the lower layer
$(QL)_3$	heating rate by longwave radiation in the upper layer
r	stress due to vertical diffusion
r_a	atmospheric albedo
r_s	surface albedo
R	gas constant for dry air
R_i	Richardson number
R_o	Rossby number
R_r	gas constant for water vapor
S_c	solar constant
S_h	rate of change of mixing radio due to horizontal diffusion
S_o	incident solar radiation at the top of the atmosphere
S_r	solar radiation absorbed by the earth's surface
$(S_t)_{ij}$	standard deviation (w.r.t. time) at grid point ij
SX	variance resulting from stationary eddies
t	time
T	air temperature
T_2	air temperature at 500 mb
T_a	air temperature at 1000 mb
T_c	thermal conductivity of ice
T_g	surface ground temperature

TX	variance resulting from transient eddies
u	zonal wind speed
U	horizontal velocity scale
v	meridional wind speed
$\underline{v}$	horizontal wind vector
$\underline{v}_s$	rotational part of the horizontal wind vector at level 1
W_h	rate of change of potential temperature due to horizontal diffusion
W_v	rate of change of potential temperature due to vertical diffusion
x	absorptivity of the atmosphere
X	a general parameter
X_n^m	spherical harmonic coefficient of X
Y_n^m	spherical harmonic
$\bar{Z}$	daily average zenith angle
Z_z	geopotential height of 500 mb
α	radiation constant
β	radiation constant or $\partial f/a\partial\phi$
γ	critical relative humidity in the lower layer
Γ	temperature lapse rate
Γ_s	moist adiabatic lapse rate
δ	declination angle
ε_2	longwave emissivity at 500 mb
ε_4	longwave emissivity at the top of the atmosphere
ε_s	longwave emissivity at the surface
ξ	normalized difference
ζ	vorticity

η	normalized ground pressure
θ	potential temperature
θ_n^m	spherical harmonic coefficient of θ
κ	$\kappa = R/c_p$
λ	geographic longitude
μ	$\mu = \sin(\phi)$
ν	frequency, or e-folding time
π	$\pi = 3.141593$
ρ	density of air
ρ_s	density of air near the surface
σ	static stability
σ_n^m	spherical harmonic coefficient of σ
τ	rotational shear between the two levels
τ_n^m	spherical harmonic coefficient of τ
ϕ	geographic latitude
χ	velocity potential
χ_s	surface velocity potential
χ_n^m	spherical harmonic coefficient of χ
$\chi_{sn}^{\ m}$	spherical harmonic coeffieient of χ_s
ψ	stream function
ψ_s	surface stream function
ψ_n^m	spherical harmonic coefficient of ψ
$\psi_{sn}^{\ m}$	spherical harmonic coefficient of ψ_s
ω	vertical pressure velocity

Ω	angular velocity of rotation of the earth
∇	horizontal del-operator $\nabla \equiv (\partial/a\cos\phi\ \partial\lambda,\ 1/a\partial\phi)$
$()^*$	the asterisk * denotes the complex conjugate, or departure from the time average
	absolute value

1. INTRODUCTION

Climate is a subject of considerable importance to human lives. The impact of different climatic regimes on the economy, health and wealth of individuals and nations cannot be denied. Of the same importance is the variability of climate. This variability has been observed, directly or indirectly, over a wide band of time scales ranging from seasons to thousands and millions of years. Theories have been proposed in order to explain the phenomena associated with climatic variability on different time scales. These theories could be categorized into two main groups, depending on terrestrial or extraterrestrial forcing mechanisms. The terrestrial-forcing climate change theories have been concerned with continental drifts, mountain building, volcanism, variations of sea level and sea temperature, and variations in the carbon dioxide content of the atmosphere. The second category of theories has been concerned with the variations in the intensity of solar radiation and variations in the earth's orbit around the sun (Milankovitch, 1941). No completely acceptable explanation of climatic change has ever been presented. The problem will remain until we gain a complete understanding of the interactions between the earth, atmosphere, oceans, and the solar and planetary system. Lorenz (1968) explored the possibility that the atmosphere may be an almost "intransitive system". In such a system the statistics taken over long, but finite, intervals differ considerably from one interval to another. If this is the case, there is a possibility that long-term climatic changes

may result from the nearly intransitive nature of the atmosphere, rather than from environmental changes. However, this theory applies to cases where environmental influences are not affected, in turn, by the system. The atmosphere by itself is not a system of this sort since the oceans, and also glacial ice areas, are affected by the atmospheric conditions.

In this thesis we will be focusing on short-term climatic variability, namely the variability through a month or season. The response of the atmosphere to sea surface temperature anomalies (SSTA) and to tropospheric thermal anomalies will be explored.

1.1 Observational Studies

The sensitivity of the atmosphere to long-lasting perturbations in the lower boundary has been the subject of many investigations. SSTA and areas of ice coverage are the most important of these perturbations.

Observational studies show possible teleconnections between SSTA and the atmospheric circulation. From analyses of three winter cases (1957-1958, 1963-1964 and 1965-1966), Bjerknes (1969) showed that positive SSTAs, in the equatorial central and eastern Pacific Ocean in late fall were accompanied by an anomalous strength of the midlatitude westerlies over the northeast Pacific. According to his hypothesis, these positive SSTAs increase the local vertical motions, thus enhancing the Hadley circulation, which in turn transports more than the average angular momentum to middle latitudes. Observations have shown that such wind anomalies are much more pronounced in the Northern Hemisphere than in the Southern Hemisphere. Nonlinear interactions of the velocity and thermal fields are more significant in the Northern Hemisphere midlatitudes than in the Southern Hemisphere. The former has higher and

broader mountains than the latter, as well as larger differential diabatic heating between land and oceans. Canton Island data showed a maximum rainfall. Thus the atmosphere has shown both local and remote response to equatorial SSTA.

Namias (1969, 1980) studied the effects of midlatitude SSTAs in the central Pacific on the weather in the United States of America during the following season. It was found that positive SSTAs in the central Pacific that occurred from 1961 through the winter of 1967-1968 enhanced and displaced the region of cyclogensis southward. This pattern caused a blocking ridge over the western United States. The ridge, with its maximum amplitude at 160° W, was accompanied by cold advection over the eastern United States, with mild temperatures prevailing over the central and western states. Cold SSTAs during the summer of 1978 in the central northern Pacific were followed by below-normal temperatures over all the United States in winter. The same studies showed that the response of atmospheric pressure to cold SSTAs would be a higher than normal pressure at the surface and aloft during the following fall. Uniform temperature anomalies over the entire United States usually are rare since the dominant long waves usually have smaller dimensions than the lateral extent of the United States. Thus the western and eastern parts of the country often display opposite temperature anomalies.

Reiter (1978) confirmed the feedback between the Intertropical Convergence Zones (ITCZ), the trade winds and sea surface temperatures. That study further indicated that this feedback is only a part of a global atmosphere-ocean interaction, among many other factors. Analysis of two severe winters (1976-1977 and 1977-1978) in the eastern United States, by Harold (1980) indicated that transient eddy activity during

abnormal winters usually is not significantly different from such activity during normal winters. The height and temperature anomalies were in phase, resulting in a structure equivalent to that of barotropic waves. Deviation of the jet stream from its normal position explained the observed precipitation patterns during the two winters.

The sea surface temperatures over the North Atlantic and North Pacific have roughly the same variance as surface air temperature on monthly, seasonal and annual time scales (Cayan, 1980). Wan-cheng et al. (1981) showed that increased (decreased) SSTA in the equatorial Pacific is associated with a delay by two months and possibly also with simultaneous, strengthening (weakening) of the upper-tropospheric westerlies in the eastern Pacific subtropics. They did not find any association between SSTA and anomalies of the northward momentum transport in the subtropical upper tropospheric flow over the eastern Pacific.

So far, the response of the atmosphere to SSTAs has been shown to be both local and remote. For the atmosphere to respond in such a manner, there must be planetary zonal or meridional oscillations that control and organize the phase and amplitude of such a response. Correlations between geopotential heights on a given pressure surface at widely separated points on the earth confirmed the presence of at least four patterns which might be indicative of standing oscillations in the planetary waves during the Nothern Hemisphere winter (Wallace and Gutzler, 1981). Examples are found over the North Atlantic, the North Pacific, polar temperate latitudes, and between the Pacific and North America. The North Atlantic oscillation was first identified by Walker and Bliss (1932) and confirmed by many studies using different indices for the oscillation (Van Loon and Rogers, 1978; Kutzbach, 1970; Wallace

and Gutzler, 1981). Positive values of the index are indicative of a strong Icelandic low, high pressure along 40°N, strong westerlies across the North Atlantic, below normal temperatures in the Greenland Labrador area as well as in the Middle East, and above-normal temperatures in the eastern United States and northwestern Europe. The North Pacific oscillation is an analogue of the North Atlantic oscillation (Walker and Bliss, 1932; Rogers 1981). Both the North Atlantic and North Pacific oscillations are characterized by north-south seesaws or standing oscillations in the sea level pressure with a node located near 50° latitude. The zonally symmetric seesaw (Lorenz, 1951) is basically the negative correlation between sea level pressure at polar and temperate latitudes. This correlation also exists in the absence of the North Atlantic and North Pacific oscillations. The last oscillation of this kind is the Pacific/North American pattern (Wallace and Gutzler, 1981), which essentially describes the blocking phenomena. Blocking high pressure is identified by the persistence of a quasi-stationary positive anomaly in the 500 mb geopotential height field. This anomaly persists for a period of at least 10 days (i.e., has a time scale longer than the typically associated with synoptic-scale variability) over at least one location (Dole, 1978). This phenomenon often happens during winter along the west coast of North America. The blocking is accompanied by a strong Aleutian low over the central Pacific and below normal geopotential heights over the southeastern United States.

To complete the discussion of the teleconnection patterns around the globe we must include two important oscillations that dominate the tropical and subtropical regions. The correlation in the surface pressure between eastern and western hemispheres at low latitudes was

recognized a long time ago in what is called the Southern Oscillation (Walker, 1923, 1924, 1928). It is defined as the tendency of the sea level pressure at stations in the Pacific (San Francisco, Tokyo and South America), and of rainfall in India to increase, while pressure in the region of the Indian Ocean decreases. The positive index of the oscillation is recognized as negative sea level pressure anomalies in the Indonesian belt with respect to positive sea level pressure anomalies in the Pacific belt. The existence of the Southern Oscillation was proved after Walker's discovery (Troup, 1965; Berlage, 1966; Horel and Wallace 1981). The Southern Oscillation has a period between 3 and 6 years, and it is not confined to tropical and subtropical latitudes, but it is linked to midlatitude systems and long waves in the westerlies (Trenberth, 1976). The Southern Oscillation is a manifestation of a nearly global variation in circulation, temperature, clouds and precipitation. Such a low frequency oscillation is linked to the fluctuations in sea level pressure in the equatorial Pacific. The ocean temperature is a triggering influence in developing the oscillation. When Walker discovered the Southern Oscillation in the twenties he did not realize the source of "memory" for such a very low frequency phenomenon, since all the atmospheric fluctuations are of much shorter periods. The question remained without answer until the work by Bjerknes (1969), mentioned above, where he emphasized that the oscillation draws its memory from the long-lasting ocean temperature anomalies in the equatorial Pacific. El Nino is a surface oceanic phenomenon recognized as warm water accumulated near the coast of Peru just before or after Christmas. This warm water interrupts the normal upwelling. El Nino is preceded by strong southeast trades at the center of the Pacific ocean,

which intensify the subtropical gyre of the South Pacific, strengthen the South Equatorial Current, and increase the east-west slope of sea level by building up water in the western equatorial Pacific. As soon as the wind stress in the central Pacific relaxes, the water flows eastward. An El Nino event lasts for about 16 months (that is, two summers and one winter) (Wyrtki, 1975).

The Walker circulation is a counterpart of the Southern Oscillation in the wind field. It is characterized by large scale rising motion over the warm zone in the west Pacific, near Indonesia, and sinking motion over regions of cold water in the east Pacific. The main forcing mechanism for the Walker circulation is the release of latent heat of condensation over the equatorial west Pacific. The release of latent heat enhances the vertical motion and results in upper-level divergence. The upper-level westerlies and the low-level easterlies over the Pacific ocean force a large scale subsidence over the cooler water of the south-east Pacific. The tropical circulation is not zonally symmetric due to the existence of such a circulation. Gill (1980), using a linear primitive equation model, speculated on the idea that Kelvin waves emanating from the Indonesian region would create an extensive region of easterlies to the east (which extend over the whole equatorial Pacific), while planetary waves would create a more limited region of westerlies to the west (over the Indian Ocean).

Many studies have shown possible teleconnections between the Southern Oscillation, Walker Circulation, El Nino and tropospheric pressure patterns at different areas. Horel and Wallace (1981) identified the atmospheric pattern associated with both the local and remote response of the atmosphere during seven warm episodes, within the period

1951-1978, in the Pacific Ocean surface temperatures. The 200 mb geopotential was taken as an indication of the tropospheric thickness in the tropical region. Fluctuations in mean tropospheric temperatures and 200 mb heights were shown to vary simultaneously with equatorial Pacific sea surface temperature fluctuations, not only in the Pacific sector, but at stations throughout the tropics. Negative SSTA in the northwestern and central Pacific at latitude 50°N occurred coincident with the east Pacific warm equatorial SSTA. The mid-tropospheric pattern associated with this sea surface temperature distribution showed below normal heights in the North Pacific and southeastern United States and above normal heights over western Canada. The extratropical response was dependent on the southward shift of the midlatitude jet stream to reach the lower latitudes. Fritz (1982) analyzed the same data of Horel and Wallace, but using the 700 mb average height difference between years of warm SSTA and years of cold anomalies. The analysis was done using a monthly average instead of a winter average. The pattern was most pronounced during January and February, rather than December. The stronger correlation during those months between the 700 mb height and sea surface temperature over the Pacific may be attributed to snow and ice distribution, which affect the atmospheric circulation. Analyses by Egger et al. (1981) of satellite data collected between February 1965 and July 1973 revealed a minimum amount of cloudiness near the date line (180°) when the Southern Oscillation index was positive. At the same time, the wind maps showed an anomalous easterly flow.

A positive Southern Oscillation index and a strong Walker circulation are associated with a southwest shift of the South Pacific Convergence Zone (SPCZ) from its position between 125°E, 0°S and

150°E, 23°S (Gruber, 1972). The ITCZ is displaced away from the equator into the Northern Hemisphere (Trenberth, 1976). Satellite cloud pictures show two tropical convergence zones in the west and central Pacific, south and north of the equator, respectively. The Indonesian continent and eastern Australian regions have a strong surge of precipitation, while the area east of 160°E is dry. On the other hand, with a negative index of the Southern Oscillation, the SPCZ is pushed from its mean tropical position towards the equator and the ITCZ moves into a near equatorial position (Ramage, 1975). Cold water upwelling at the equator is replaced by positive SSTA in the equatorial central and eastern Pacific (El Nino). The equatorial dry zone east of 160°E experiences one of its prolonged precipitation surges. On satellite photographs one extended convergence zone marked by a cloud band near the equator extends across almost the entire width of the Pacific ocean.

These tropical phenomena seem to have a teleconnection with midlatitude and extratropical geopotential height fields. Reiter (1981) showed that low height anomalies dominate the 500 mb central North Pacific pattern for months, with precipitation maxima in the Line Islands. The 500 mb planetary wave anomalies in midlatitude can serve as triggers for tropical precipitation patterns, especially during January. Deep troughs over the central North Pacific during that month apparently have a tendency to push the ITCZ equatorward. A similar conclusion was reached by Van Loon and Rogers (1981). The negative phase of the Southern Oscillation is associated with a high zonal-mean poleward flux of sensible heat, and the 700 mb temperature and heights tend to be lower between 30°N and 60°N with a minimum value at 45°N.

The interannual variability of precipitation in the tropics has been attributed to the variability of the ITCZ (Kraus, 1977; Hastenrath, 1976; Hastenrath and Heller, 1977). A recent study by Stoeokenius (1981) showed that this hypothesis failed to explain many important rainfall anomalies in the tropics. In other words the zonally averaged Hadley circulation does not seem to be able to account for most of the observed interannual rainfall variations, and hence of general circulation variations, in the tropics. East-west circulations like the Southern Oscillation and the Walker Circulation have an important influence.

1.2 Theoretical Investigations

The quasi-stationary ultra-long waves (zonal wave number 1-4) are of major importance in determining the large scale characteristics of the atmosphere. The interannual variability of their phase and amplitude is an indication of the change of the behavior of the atmosphere and, therefore, of regional climate. In the Northern Hemisphere wave number 2 is the dominant energy peak, while in the Southern Hemisphere it is wave number 1 (Holton, 1975). The development of atmospheric ultra-long waves is due to lower boundary forcing, namely the earth's surface. Differential heating between land and sea together with the distribution of topography are the two main mechanisms that force the ultra-long waves (Sankar-Rao, 1965; Sankar-Rao and Saltzman, 1969). This also was confirmed by Ashe (1979) using a spectral model which solved a time average asymmetric flow induced by topography and diabatic heating. When the forcing of topography was considered alone, it was

found that most of the features were displaced from their true positions. In middle latitudes the latent heating (calculated from precipitation averages) tends to be in phase with the sensible heating. The opposite is true in the subtropics, particularly in desert regions, where strong positive departures of sensible heating are balanced by strong negative departures of latent heating. Tung and Lindzen (1979) stressed the importance of the non-linear interactions, and forcing by the topography and diabatic heating in simulating the major circulation features. During a normal year the two kinds of forcing act out of phase. This is because the major north-south mountains in the Northern Hemisphere (e.g., the Rockies and Alps) lie along the eastern side of the Pacific and Atlantic oceans, respectively. The major warm ocean currents, like the Kuroshio and Gulf Stream, flow in the western side of the Pacific and Atlantic. With this normal forcing structure, the two mechanisms seem to act against each other. The zonal wind speed at 500 mb is larger than the phase speed of the ultra-long waves and the pattern propagates eastward with the zonal flow. Since the topographic distributions are quasi-permanent, if the diabatic heating due to land and sea distribution was altered, then we would expect the two kinds of forcing to act in harmony to reinforce, instead of cancelling, each other. If the wind circulation in the lower atmosphere is such that the phase speed of the wave is reduced to zero, a nearly resonant state may be reached by the amplifying planetary waves, causing a blocking phenomenon. In all the previous studies the mean zonal flow was specified; not calculated by the models.

We notice in the preceding discussion that the fundamental feature of the forcing of stationary waves in the atmosphere is that the forcing

is largely implicit, depending on the wind circulation in the atmosphere itself. Charney and DeVore (1979) and Hart (1979) stressed this fact. In their theory of "multiple equilibrium states", blocking was found to be one of many equilibrium states that can be reached by the system itself. Roads (1980), using a nonlinear quasi geostrophic model in which orography and zonal heating are calculated, has found multiple equilibrium states. The states are either near a resonance point in the system or at the zonal forcing equilibrium point. The multiplicity of the solution occurs because the heat transport and mountain torque are nonlinear functions of the zonal stream function. More analysis was done by Charney et al. (1981) using a barotropic nonlinear channel model incorporating observed zonal topography. Multiple stationary equilibria were obtained. From the observed 34 blocking events of the 500 mb geopotential, only 19 could be explained as one or another of the equilibrium states, whereas 5 events could be explained due to forcing or geometry. What is not explained is the localized position of the ridges and troughs and mechanisms of transition to and from the blocking configuration. In other words, the theory could not prove whether or not there is (are) a certain mechanism(s) responsible for forcing, or ending, any or all of these multiple solutions, including blocking.

Linear models with steady state solutions have been used to identify certain responses of the atmosphere to large scale forcing. There is some agreement between the linear model results and the observed anomalies. However, the linear theory is questionable for such types of studies due to the strong nonlinearity of the atmosphere itself. It is doubtful that the positions of the actual extrema caused by large scale anomalies could be accurately predicted. Egger (1977) tested the effect

of tropical SSTA in both the eastern Pacific and the Atlantic using a linear two-level hemispheric model. In the Pacific case the response of the midlatitude atmosphere to the tropical anomalies was negligible. This result was not supported by observations. However, the tropical Atlantic anomalies showed a larger response by the midlatitude atmosphere.

The sphericity of the earth could be an important factor in determining the correct response of the atmosphere to the large scale anomalies, in particular the propagation of Rossby waves on a sphere. The results suggest that the nature of the response is quite different between the different zonal sectors of the globe. Webster (1981) presented the argument that, in low latitudes, where the convective activity and the diabatic heating are the dominant factors in the thermal energy equation, the response of the atmosphere to the anomalies seems to be of a direct nature. In other words, the warm SSTA in the tropical oceans enhances the vertical velocity, which in turn increases the poleward momentum flux in the upper layer of the troposphere and strengthens the midlatitude westerlies. In this case the teleconnections between low and midlatitudes are strong and clear. On the other hand advection is of primary importance in the thermo-dynamic energy equation in middle latitudes, and the anomalies cause an indirect circulation (rising of cold air and sinking of warm air) rather than a direct circulation as in the low latitude case. Therefore, the local response to the midlatitude anomalies is smaller than that for the low latitude case. The teleconnection between the midlatitude atmosphere and midlatitude SSTAs depends upon the nature of the atmospheric circulation. An example is whether the anomalies are in a region of rising or sinking motion.

Subtropical SSTA has an effect on the atmosphere in middle and high latitudes since the response of the atmosphere to the tropical heating can have a substantial influence on the middle and high latitudes, provided that part of the heating is in the belt of westerly winds (Opsteegh and Van Den Dool, 1980). In this case, modes with meridional components to the group velocity vector will be excited which will allow a substantial response at higher latitudes (Webster, 1982). The propagation of the long wave lengths as a result of subtropical thermal heating was shown to be polewards as well as eastwards, while shorter wavelengths were trapped equatorward of the poleward flank of the jet (Hoskins and Karoly, 1981).

The question of the generally larger response of the atmosphere to the tropical anomalies than to midlatitude anomalies still has no satisfactory answer. The previous linear models (Opsteegh and Van Den Dool, 1980; Webster, 1981, 1982; Hoskins and Karoly, 1981) are constrained by the assumption of zonal symmetry in the basic state. Observational studies of general circulation statistics indicate that quasi-stationary modes in the extratropical regions and the tropics provide significant longitudinal perturbations in the mean state of the atmosphere. Such quasi-stationary perturbations probably will alter the character of both the teleconnection propagation and the local form of the atmospheric response.

The importance of nonlinear aspects of the atmosphere has been demonstrated by many investigators. The amplitude of baroclinic waves, and to a lesser extent the amplitude of their transports of heat and momentum, are sensitive to the barotropic component in the basic flow (Simmons and Hoskins, 1980). Some of this sensitivity has been traced

to distinctly barotropic effects, which arise during the nonlinear evolution of the waves. Frederiksen and Sawford (1981) used a spherical equivalent barotropic model to study the linear and non-linear solutions for the effects of topography in forcing the stationary eddy field. There are considerable differences between the two types of solutions, which arise largely from the fact that linear solutions are resonant or near resonant, whereas the nonlinear solutions are not. Comparison with observed fields show nonlinear effects to be most important at low latitudes.

1.3 General Circulation Models

Apart from the simplified linear theory discussed before, many efforts have been devoted towards finding the sensitivity of the atmosphere to environmental anomalies using large scale general circulation models (GCMs). Several important studies of this type were the experiments done by Rowntree (1972, 1976b). He used a nine-level hemispheric model of the atmosphere developed at the Geophysical Fluid Dynamics Laboratory (GFDL) to test Bjerknes hypothesis that fluctuations of ocean temperatures in the tropical east Pacific are responsible for major variations in the position and intensity of the Aleutian surface low. The experiments were done with both warm and cold SSTA with a maximum difference of 3.5°C. The results of the experiments showed that tropical ocean temperatures have important effects on the model atmosphere, in the tropical and extratropical regions. The warm ocean induced a surface low over the area of maximum temperature, and the associated low level convergence and ascent gave increased tropical rainfall over the central and east Pacific, with decreases over the west Pacific and parts of South America. An upper-tropospheric subtropical

jet stream was generated with persistent trough-development to the north over the midlatitude east Pacific. The Aleutian low shifted east and deepened, confirming Bjerknes hypothesis. In such a hemispheric model with boundary conditions imposing symmetry about the equator, it was argued that the equatorial wall in Rowntree's model was responsible for the anomalous precipitation calculated in the tropical region (Ramage and Murakami, 1973; Ramage, 1975). However, the experiments using a global 5 layer GCM (United Kingdom meteorological office) (Corby et al., 1977) gave results consistent with the hemispheric experiment. Experiments with SSTA over the Atlantic agree with those done over the Pacific. Decreases of surface pressure were obtained over the warm tropical water and extended north to at least 60°N over the eastern Atlantic (Rowntree, 1976b). In many experiments it was noticed that warm anomalies gave more significant atmospheric response than cold anomalies (Houghton et al., 1974).

Many experiments were done for testing the effect of middle latitude and extratropical SSTA. In most of these experiments it was difficult to detect the signal above the noise level, but compositing of several experiments with different anomalies suggests a tendency for pressure falls on the equatorward side of the anomalies (Rowntree, 1979). In other experiments testing North Pacific SSTA, the results suggest that a statisfically significant signal can be detected in the immediate vicinity of large ocean surface temperature anomalies, but that teleconnections of this signal downstream over the United States can be identified only with a small statistical confidence (Chervin et al., 1976). As a matter of fact, extremely cold or warm extratropical SSTAs, were needed in both the Pacific and Atlantic Oceans to

detect a signal with a high confidence level (Kutzbach et al., 1977; Chervin et al., 1980). In the last series of experiments by Chervin et al. (1980), experiments were done assuming a dipole-type anomaly distribution with warm anomalies in the west of the North Pacific and cold SSTA to the east. This pattern may not resemble the observed pattern (Horel and Wallace, 1980). At the same time the atmospheric response may be reduced since the cold (warm) anomalies are under a region of rising (sinking) air.

Simpson and Downey (1975) used the NCAR model to find the sensitivity of the atmosphere to SSTA in the middle latitudes in the Southern Hemisphere. They used two patterns of SSTA in addition to that used in the control run. The SSTAs were associated with completely different atmospheric circulations. The atmosphere responded more to one pattern than the other. This may suggest that the response of the atmosphere to SSTA may depend upon the initial atmospheric circulation associated with the location of the anomalies. While many numerical models failed to support Namias' (1969, 1980) hypothesis, the results of a recent experiment using the GLAS (Goddard Laboratory for Atmospheric Science) model (Shukla and Bangaru, 1981) supported his hypothesis. The SSTA and atmospheric circulation for this experiment were similar to those observed during January 1977. It was shown that a cold SSTA over the Pacific produces a strong southward flow over the United States and colder temperatures in eastern Canada and the United States, as was observed during winter 1977. Contrary to the previous numerical experiments, the results indicated that the SSTA over the Pacific can produce a significant downstream effect over the continental United States. The different results between the NCAR experiment (Kutzbach et al., 1977;

Chervin et al., 1976, 1980) and the GLAS experiment may be attributed to the spatial structure of the SSTA.

The more significant response of the atmospheric models to tropical SSTAs than to midlatitude and extratropical SSTAs still has no completely satisfactory explanation. It is believed that both the physical and dynamical characteristics of the interaction between the ocean and atmosphere should be explored further. Kraus (1972) claimed that, via an enhanced air-sea interaction, the role of SSTA should be of most significance in the tropics for the following reasons:

1) Perturbations induced by changes in the zonal wind stress will have a much faster response in the tropics due to the higher group velocity of oceanic Rossby waves at lower latitudes.

2) Local upwelling should produce larger surface temperature variations because of the shallower thermocline in the warm sea areas.

3) Surface temperature variations in the tropics can produce larger variations in the heat supply than is possible in higher (colder) latitudes.

If ocean-atmosphere feedbacks are not considered, the middle latitude SSTA could be inefficient in significantly changing the global diabatic heating. The atmosphere over these areas behaves in a highly nonlinear fashion and is affected by transient eddies and baroclinic instability. Ashe (1978) discussed an indirect offset of middle latitude SSTA. The anomalies would change the static stability parameter near the surface, which in turn would affect the baroclinic instability of the atmosphere. The advection of unstable eddies of this kind could cause a significant effect on the longwave pattern, and this large scale

change could feed back to affect the diabatic heating itself (Ashe, 1978). Cyclogensis at middle latitudes is created by land and sea surface temperature contrast, the zonal wind, the mountain chains and the latent heat released. So the relation between middle latitude SSTA and the atmosphere is more complicated than a simple direct response of the atmosphere to the anomalies.

The complex and nonlinear interactions between different variables describing the ocean-atmosphere circulations are an important factor in obtaining significant results from different experiments. A change in the lower boundary surface temperature may affect the cloud distribution, which again has a feedback to the atmospheric circulation. The results of a simple, coupled air-sea model (Lau, 1979) indicated that sea surface temperature distribution, which is strongly controlled by the oceanic upwelling, is the primary factor in determining the location and movement of the tropical rainbelt. The strongest convective activity in the ITCZ, however, depends mainly on the moisture supply from horizontal convergence and the static stability of the lower atmosphere, but do not necessarily coincide with the occurrence of maximum sea surface temperatures. The increase of sea surface temperature, while increasing the evaporation, condensation and precipitation, was found to be associated with a decrease in the global cloudiness and relative humidity (Schneider and Dickinson, 1974; Roads, 1978). Sellers (1976) suggested that a possible reason for these results was that an increase in temperature may correspond to an increase in convective cloudiness, a decrease in stratus cloudiness, and a decrease in total cloud area, along with an increase in condensation from increased evaporation.

Stephens and Webster (1981) concluded that surface temperature and vertical temperature structure is acutely sensitive to the cloud amount and cloud form. Low clouds cool the surface and high clouds warm it. A study by Wetherald and Manabe (1980) showed that if the solar constant was increased, clouds diminish in the upper and middle troposphere at most latitudes and increase in the lower stratosphere and near the earth's surface. The area mean change in the net incoming solar radiation is compensated by the outgoing terrestrial radiation at the top of the atmosphere. Owing to this compensation, the change of cloud cover has a relatively minor effect on the sensitivity of the area mean climate. Meanwhile another study by Shukla and Sud (1981), using the GLAS model to investigate the effect of cloud radiation feedback, showed a significant change in the simulated large scale circulations of the model.

Ramage (1977) suggested that interpretation of the precipitation patterns from numerical models must be made with caution because most numerical models are non-interactive; the sea surface temperature is prescribed and does not change as a result of the atmospheric conditions above it. Even with interactive models, the problem still exists with convective parameterization. The most complex parameterization schemes still cannot resemble the complicated nature of convection, especially in the tropics. The results may give a realistic picture of the actual atmosphere. As an example of this problem, Ramage tested an empirical formula given by Rowtree (1976a). The empirical formula correlates precipitation with SSTA in the Pacific region east of the date line and from the equator to 20°N. In this region the area-averaged sea surface temperature increased 1.7°C between December 1971 and December 1972 .

According to the empirical formula of Rowntree's model, the rainfall should have increased 5.8 mm/day. But the observations showed that rainfall decreased by 3.4 mm/day.

1.4 Scope of the Present Study

The present research has two main phases. The first is the development of a global spectral model. The second is to examine theoretical arguments using such a model. We intend to gain more understanding of the dynamical response of the atmosphere to possible existing patterns of SSTA and mid-tropospheric thermal anomalies. The points of investigation are:

1) The atmospheric response to SSTA at different locations. For example, how does the atmosphere respond to a cold SSTA in the North Pacific, a warm SSTA in the equatorial eastern Pacific, or to both at the same time? The response of the atmosphere to negative SSTA in the North Pacific and positive SSTA in the equatorial region was not examined before. A recent study by Horel and Wallace (1981) suggested that this pattern of the SSTA has a significant influence on Northern Hemisphere weather.

2) The effect of mid-tropospheric thermal anomalies which may exist as a result of anomalous release of latent heat. Atmospheric thermal anomalies are more likely to occur as propagating waves which resemble the atmospheric motion in a certain region. We will be concerned with thermal anomalies in the tropical region which are triggered by the interannual variability of the location of the ITCZ.

3) The atmosphere may have a different memory of the thermal anomalies at different locations. In other words, if the anomalies

were removed there would be different recognition of such an effect by the atmosphere, depending on their location and the associated atmospheric circulation.

The experiments are designed to examine both the local and remote atmospheric response to SSTA or mid-tropospheric thermal anomalies. The analysis includes the horizontal wind, geopotential height, temperature, vertical motion, and evaporation fields. The average tropospheric amplitudes of the transports and variances resulting from stationary and transient eddy components also are analysed.

For this purpose a low order spectral global model in linear balance was developed. Nonlinear interactions, topographic forcing and sea-land differential heating were included. There are no assumptions of zonal symmetry or specification of the zonal flow. This type of medium complexity model, in which the dynamical and physical processes are simplified without contradicting important observations of the atmosphere, provide a further insight into the results of the complicated general circulation models, which usually have more degrees of freedom. The model developed has an advantage over steady state linear models or non-steady state linear models in that the time dependent nonlinear interaction of heating and motion can be simulated. On the other hand, the simplicity of the model relative to large scale general circulation models gives the advantage of an easier interpretation of the model's results.

The economic computer runs of medium complexity models have the advantage of examining more hypotheses and running for longer periods of integration without excessive cost. In the present study the model was used for a 3 month simulation of the winter circulation for the control

and anomaly cases. The completion of 30 days integration takes about 50 seconds using the NCAR CRAY I machine. The model could be used economically for extended periods of integration. Kraus and Lorenz (1966) used a model by Lorenz (1960) for very long periods of integration to study the variability and predictability of the atmosphere. Models of such design have been used for climate sensitivity studies. Salmon and Hendershott (1976) used a quasi-geostrophic model to study the effect of SSTA on the atmospheric circulation. Kikuchi (1979) used a model similar to the one presented here, except that in the present model we assume a variable static stability and a hydrologic cycle in the lower layer for studying the influence of orography and land-sea distribution on the Northern Hemisphere winter circulation. Held and Suerz (1978) developed a two level primitive equation model which was used to examine the response of the atmosphere to perturbations of the solar constant (Held et al., 1981).

Chapter 2 presents the model description and formulation. In Chapter 3 the simulated January climate of the model is compared with observations. Experiment design and results are explained in Chapters 4 and 5.

2. A TWO-LEVEL GENERAL CIRCULATION MODEL

2.1 Introduction

A two level global, spectral model using pressure as a vertical coordinate has been designed. The system of equations retains the nonlinear interactions between the dependent variables. The system is quasi-geostrophic in a linear balance form (Lorenz, 1960). The mechanical effects of orography have been introduced in the form of a lower boundary vertical velocity. The differential diabatic heating due to the distribution of land and sea also are parameterized. Both orography and differential heating between land and sea are important mechanisms for producing a correct amplitude and phase of the middle latitude ultra-long waves (wave numbers 1-4) (Sankar-Rau and Saltzman, 1969; Bates, 1977). The solar radiation budget is specified as a function of latitude and time. Longwave emissivities also are included. Static stability is variable in the model. This condition is necessary for conserving the sum of energies of the model. Also, it is important for our purpose of sensitivity studies. The model uses a moisture budget equation in its lower layer only, with a convective adjustment to prevent super-critical lapse rates. Under reversible adiabatic processes, the equations conserve the sum of kinetic energy and available potential energy.

In the horizontal domain a rhomboidal spectral truncation is assumed (truncated at zonal wave number 9) (Fig. 2.1). The dependent variables are expanded in terms of their harmonic coefficients with spherical harmonics as basis functions.

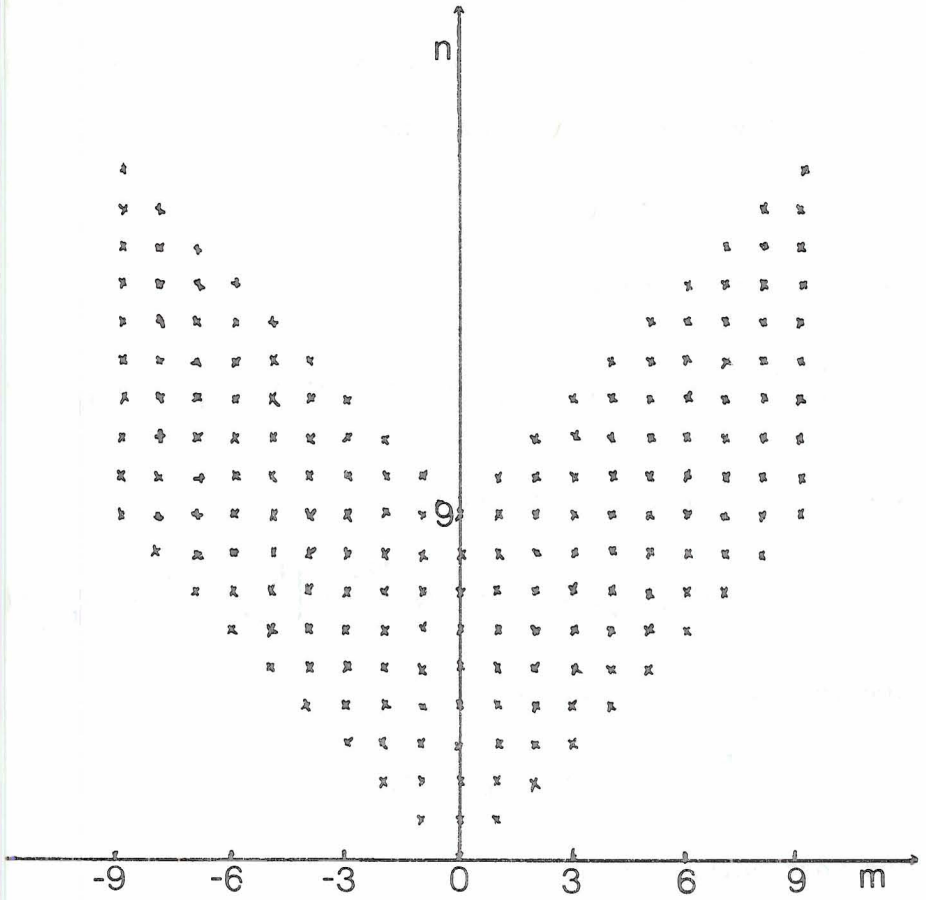

2.1 Schematic representation of the model's rhomboidal spectral resolution, m is the zonal wave number and n is the degree of the spherical harmonic.

2.2 Basic Equations

The following system of equations forms the basic structure of the model. The velocity field at each level is split into its rotational and divergent parts. For a certain level, ℓ, the system of equations representing the model's atmosphere is given by

$$\underline{v}_\ell = kx\nabla\psi_\ell + \nabla\chi_\ell, \tag{2.1}$$

the vorticity equation

$$\frac{\partial}{\partial t}\nabla^2\psi_\ell = -J(\psi_\ell, \nabla^2\psi_\ell+f) - \nabla\chi_\ell\cdot\nabla f + f\frac{\partial\omega_\ell}{\partial p} + (F_h)_\ell + (F_v)_\ell, \tag{2.2}$$

the thermodynamic energy equation

$$\frac{\partial\theta_\ell}{\partial\tau} = -J(\psi_\ell,\theta_\ell)-\nabla\chi_\ell\cdot\nabla\theta_\ell-\omega_\ell\frac{\partial\theta_\ell}{\partial p} + \left[\frac{p_o}{p_\ell}\right]^K \frac{Q_\ell}{c_p} + (W_h)_\ell + (W_v)_\ell, \tag{2.3}$$

the thermal wind equation

$$c_p\, p_o^{-K}\nabla^2\theta_\ell = -\nabla\cdot\frac{\partial}{\partial p^K}(f\nabla\psi_\ell), \tag{2.4}$$

the Continuity equation

$$\frac{\partial\omega_\ell}{\partial p} + \nabla^2\chi_\ell = 0, \tag{2.5}$$

and the moisture budget equation (at the lower level only)

$$\frac{\partial q}{\partial t} = -\nabla\cdot(\underline{v}_1 q) + E - P_c + (S_h)_1. \tag{2.6}$$

In (2.1) to (2.6), $\underline{v} = (u,v)$ is the horizontal velocity, ω the vertical pressure velocity, ψ the stream function, χ the velocity potential, θ the potential temperature, and q the water vapor mixing ratio. (F_h) and (F_v) are the horizontal and vertical friction respectively.

f is the Coriolis parameter; $\kappa = R/c_p$, where R is the gas constant for dry air, and c_p is the specific heat at constant pressure. p_o is the pressure at the lower boundary (1000 mb). (W_h) and (W_v) are the horizontal and vertical temperature diffusion, respectively. W_v is included in the diabatic heating rate, Q, after parameterizing the vertical heat fluxes. $(S_h)_1$ is the horizontal diffusion of moisture. Q is the sum of diabatic heating rates per unit mass. E is the evaporation rate from the surface to the lower layer and P_c is the precipitation rate.

The diffusion and diabatic heating functions need to be parameterized in terms of the dependent variables ψ_ℓ, θ_ℓ, ω_ℓ, χ_ℓ, v_ℓ and q in order to form, with the necessary boundary conditions, a closed system of equations.

The two levels represented in the model are 750 mb (ℓ=1) and 250 mb (ℓ=3). The average values of the modeled variables are calculated at the lower and upper layers. An intermediate level, 500 mb (ℓ=2) also is used for calculation of the vertically averaged conditions of the model's atmosphere. The lower boundary is the 1000 mb level (ℓ=0) (Fig. 2.2).

The upper layer is heated by short- and long-wave radiation, by the lateral diffusion of heat, and by the heat released by convective adjustment. The lower layer is heated by short and longwave radiation, lateral diffusion of heat, sensible heat flux from the surface, and latent heat release due to condensation, and is cooled by the heat transferred upward by the convective adjustment. Evaporation from the surface is the only source of moisture to the lower layer. Condensed water is assumed to fall as precipitation, without any re-evaporation into the lower layer.

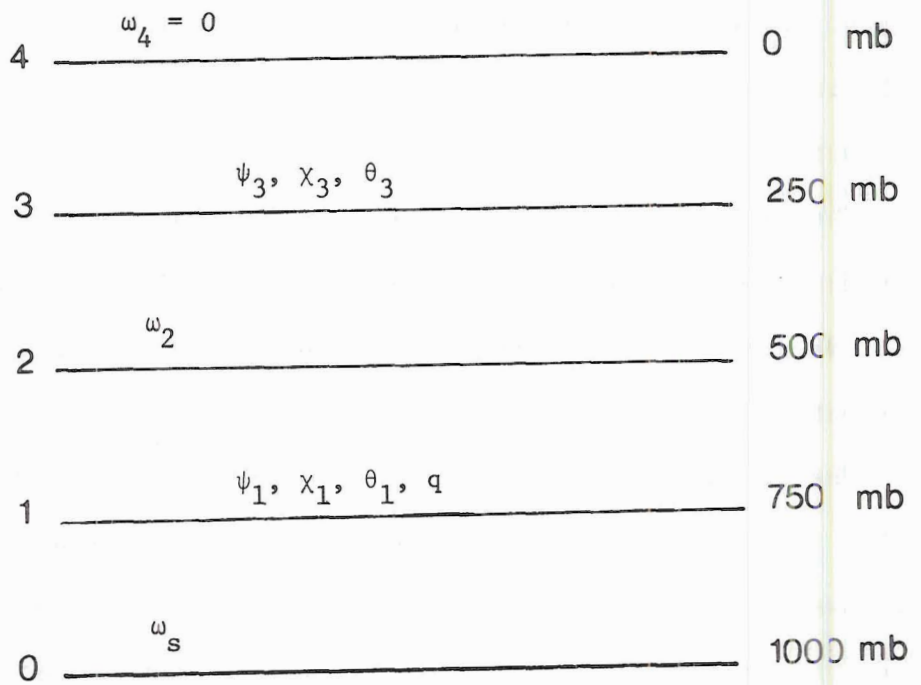

2.2 Schematic representation of the vertical structure of the model.

2.3 Boundary Conditions

In the horizontal resolution all wave number modes up to wave number 9 have been retained, in order to maintain the interaction between the two hemispheres. A wall at the equator was not assumed.

The boundary condition for the vertical velocity in a pressure-coordinate system, ω, at the top of the model's atmosphere is

$$\omega_4 = 0.$$

The mechanical influence of orography is introduced in the model as a vertical velocity at the lower boundary (1000 mb), $\omega_s \neq 0$. Rather,

$$\omega_s = \underline{v}_s \cdot \nabla p_g,$$

where $\underline{v}_s$ is the rotational part of the 750 mb wind velocity. The contribution from the divergent part is at least one order of magnitude less, hence is neglected. p_g is the surface pressure due to orography. Applying the continuity equation (2.5) at different levels, the vertical pressure velocities at the different levels are given by

$$\omega_2 = -\Delta p \nabla^2 \chi_3, \tag{2.7}$$

$$\omega_3 = -\frac{\Delta p}{2} \nabla^2 \chi_3, \tag{2.8}$$

$$\omega_1 = -\frac{\Delta p}{2} \nabla^2 (2\chi_3 + \chi_1), \tag{2.9}$$

and $$\omega_s = -\Delta p \nabla^2 (\chi_3 + \chi_1), \tag{2.10}$$

where Δp is the difference between the upper and lower levels $\cong$ 500 mb.

We define χ_s, the velocity potential at the surface, such that

$$\omega_s = -\Delta p \nabla^2 \chi_s. \tag{2.11}$$

Then

$$-\nabla^2 \chi_s = 2(\underline{v}_s \cdot \nabla \eta) \tag{2.12}$$

where η is the normalized pressure = p_g/p_o, $p_o = 2\Delta p$

from (2.10) and (2.11), and we obtain

$$\chi_s = \chi_1 + \chi_3. \tag{2.13}$$

For computing the surface pressure, p_g, the continental elevations, smoothed over 5° latitude × 5° longitude "squares" are used (Berkofsky and Bertoni, 1955). The conversion from elevation heights to pressure is done assuming an atmosphere with a constant lapse rate of 6.5×10^{-3} °K m^{-1}.

The low order truncation used in the model is considered as a further filter to satisfy the quasi-geostrophic approximation, where the vertical velocity should be three orders of magnitude less than the horizontal wind (Haltiner, 1971). Fig. 2.3 shows the smoothed orography distribution used in the model.

2.4 Horizontal Diffusion

The horizontal diffusion terms are not necessary for computational stability when using a spectral model. They are required to inhibit spurious growth of amplitude at scales close to the point of truncation due to spectral blocking (Puri and Bourke, 1974). At a level ℓ the diffusion terms are given by

$$(F_h)_\ell = k_h(\nabla^2(\nabla^2\psi_\ell) + 2\frac{(\nabla^2\psi_\ell)}{a^2}), \tag{2.14}$$

$$(W_h)_\ell = k_h \nabla^2\theta_\ell, \tag{2.15}$$

and $$(S_h)_\ell = k_h \nabla^2 q. \tag{2.16}$$

where $k_h = 1.0 \times 10^5$ $m^2 sec^{-1}$ (Phillips, 1956) is the lateral eddy diffusion coefficient, and a is the radius of the earth. The last term on the right side of (2.14) is due to the effect of a spherical earth.

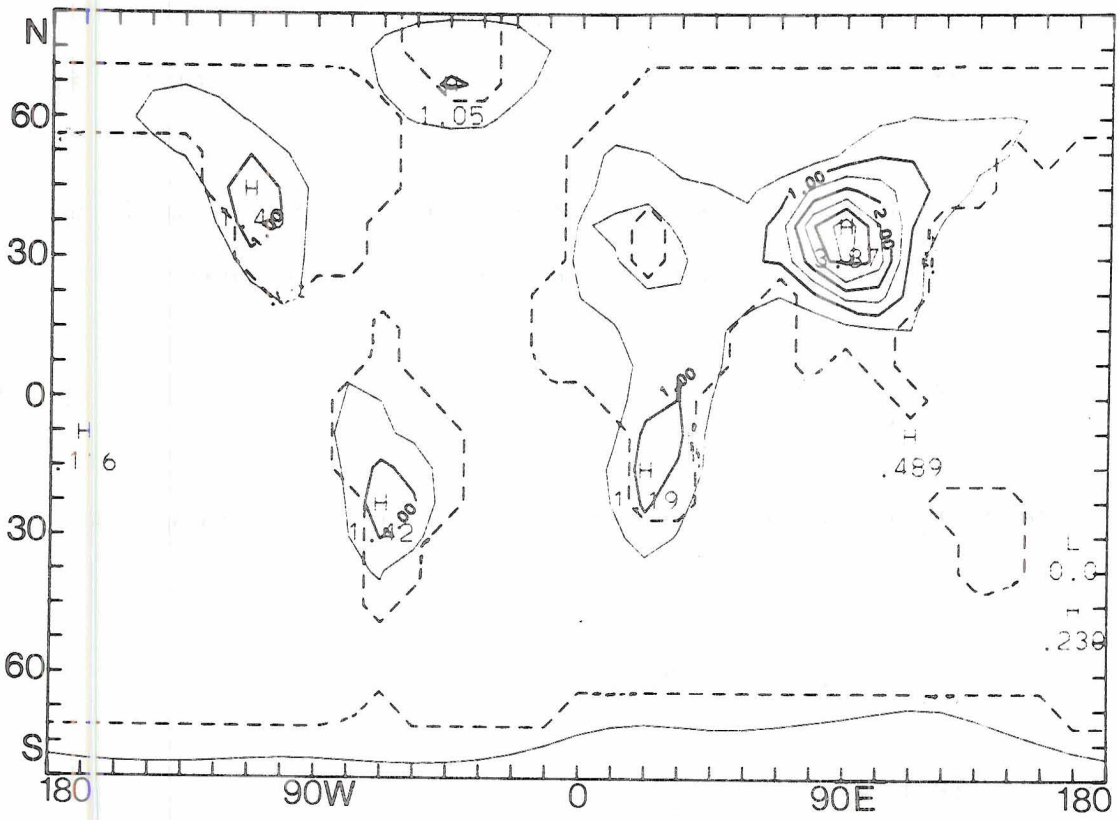

2.3 Orography truncated at wavenumber 9 (Km).

2.5 Vertical Diffusion

2.5.1 Parameterization of Frictional Dissipation

The two assumptions used for parameterizing the frictional dissipation are as follows (Lorenz, 1961):

a) Surface frictional drag is proportional to the flow in the surface layer;

b) friction between the two layers is proportional to the difference between the flow of the two layers.

$$(F_v)_\ell = - g \frac{\partial r_\ell}{\partial p} \tag{2.17}$$

where r_ℓ is the rotation stress due to vertical diffusion at level ℓ.

$$(F_v)_3 = \frac{g}{\Delta p} (r_4 - r_2) \tag{2.18}$$

$$(F_v)_1 = \frac{g}{\Delta p} (r_2 - r_0). \tag{2.19}$$

The rotational stress at the top of the model's atmosphere, r_4, is assumed to be equal to zero. The coefficients of friction at the underlying surface and the surface separating the layers are denoted by k_s and $2k_d$, respectively.

$$r_0 = + \frac{\Delta p}{g} k_s \nabla^2 \psi_s \tag{2.20}$$

and $$r_2 = \frac{\Delta p}{g} k_d (\nabla^2 \psi_3 - \nabla^2 \psi_1), \tag{2.21}$$

where ψ_s is the surface stream function extrapolated from the values at levels 250 mb and 750 mb, assuming ψ is linear with respect to height. Substituting (2.20) and (2.21) into (2.18) and (2.19), we obtain

$$(F_v)_3 = -k_d \nabla^2 (\psi_3 - \psi_1), \tag{2.22}$$

and

$$(F_v)_1 = k_d \nabla^2(\psi_3 - \psi_1) - k_s \nabla^2\psi_s, \tag{2.23}$$

where $k_d = \mu\rho_\ell \left(\frac{g}{\Delta p}\right)^2$ and $k_s = \mu\rho_s \left(\frac{g}{\Delta p}\right)^2$, μ is the small scale vertical eddy stress coefficient, and ρ_ℓ and ρ_s are the air densities at level ℓ and at the surface respectively. The two coefficients (Kikuchi, 1969 and Charney, 1959) are given by

$$k_s = 4 \times 10^{-6} \text{ sec}^{-1},$$

and $$k_d = 5 \times 10^{-7} \text{ sec}^{-1}.$$

2.5.2 Surface Sensible and Latent Heat Fluxes

The heat and moisture fluxes are calculated in the same way as was described by Bourke et al. (1977). The sensible heat flux at the lower layer is calculated using the bulk formula

$$Q_s = \rho_s c_p c_d |v_s| (T_g - T_a), \tag{2.24}$$

where T_a is the surface air temperature at anemometer level, T_a is extrapolated from the temperature values at 250 mb and 750 mb to level 1000 mb, c_d is the drag coefficient, and T_g is the surface temperature, which is determined from the surface thermal energy balance. Over water, the sea surface temperatures are specified.

The evaporation from the surface to the lower layer is given by

$$E = \rho_s c_d |v_s| GW(q_s(T_g) - h_s q_s(T_a)). \tag{2.25}$$

The amount of latent heat lost from the surface due to evaporation is

$$Q_e = LE, \tag{2.26}$$

where h_s is a measure of the relative humidity in the layer. The wetness parameter, GW, is equal to unity on water surfaces. Over land

surfaces

$$GW = 0.25.$$

The drag coefficent c_d is assumed to be constant over land and oceans. Over land $c_d = 0.004$ and for the ocean case $c_d = 0.001$ (Bourke et al., 1977). q_s is the saturation mixing ratio at 1000 mb.

2.6 Radiation Budget

2.6.1 Solar Radiation

The incoming solar radiation at the top of the model's atmosphere is calculated as a function of daily mean zenith angle (Wetherald and Manabe, 1972). Diurnal variation of the solar energy is excluded.

The mean zenith angle $\bar{z}$ is given by

$$\cos\bar{z} = \sin\phi \sin\delta + (\cos\phi \cos\delta \sin H_o)/H_o, \tag{2.27}$$

where ϕ is the latitude angle, δ is the declination angle and H_o is the hour angle given by

$$H_o = \cos^{-1}(-\tan\phi \tan\delta) \tag{2.28}$$

$$\delta = 23.45 \sin 2\pi \left(\frac{N-80}{360}\right).$$

N is the number of days measured from day 0 at 00Z 1 January.

The incoming solar radiation at the top of the atmosphere is given by

$$S_o = \bar{S} H_o/\pi, \tag{2.29}$$

where

$$\bar{S} = \begin{cases} \left[\frac{a_o}{a_s}\right]^2 S_c \cos\bar{z} & \phi - \delta < \frac{\pi}{2} \\ 0 & \phi - \delta > \frac{\pi}{2} \end{cases} \tag{2.30}$$

S_c is the solar constant, assumed as 1400 W/m^2. Recent measurements of solar irradiance from earth orbiting satellites (Smith et al., 1982) give an average value about 1375 W/m^2.

a_s and a_o are the instantaneous and mean distances of the earth from the sun, respectively,

$$\frac{a_s}{a_o} = 1 + .01676 \sin 2\pi \left(\frac{N-94}{360}\right). \tag{2.31}$$

The solar radiation absorbed by the atmosphere (Saltzman, 1967), S_r, is given by

$$S_r = x(1-r_a)\bar{S}, \tag{2.32}$$

where x is the absorptivity of the atmosphere, assumed to be constant = 0.26 in this study.

r_a is the albedo of the atmosphere. This parameter was calculated using a formula by Vernekar (1975), which includes the mean zonal amount of clouds.

$$r_a = (\alpha + \beta c)c \tag{2.33}$$

β is a constant equal to 0.38, α is a function of latitude, c is the amount of low and medium clouds in tenths of sky cover. Although the model has no explicit modulation of the clouds, they are implicitly included through the atmospheric albedo and the solar energy budget.

The net solar energy absorbed by the earth's surface is given by

$$S_s = (1-x)\ (1-r_a)\ (1-r_s)\ \bar{S},$$

where r_s is the January zonal-average albedo of the earth's surface (oceans are not included). The surface albedos are categorized as areas of permanent ice (albedo = 0.8), partial snow or ice cover (Albedo = 0.4 to 0.6), deserts or patchy snow in middle and low latitudes (Albedo =

0.2 to 0.3), dense forests (Albedo = 0.10 to 0.15). The values of different parameters used for the January solar radiation calculations are given in Table (2.1).

The above formulae give a global average planetary albedo ≅ 34%. Stephens et al. (1981), using satellite observations, estimated the global average planetary albedo for January to be 31%. Fig. 2.4 reveals the calculated solar radiation absorbed by the atmosphere and the earth's surface at the first of January.

2.6.2 Longwave Radiation

The calculation of the longwave radiative cooling makes use of a simple non-interactive scheme. The computations are performed by taking longwave flux differences across each layer. The upward and downward emissivities were estimated from values given by Stone and Manabe (1968). Those values were calculated using an 18 level radiation model. Average vertical profiles of temperature, water vapor, ozone and carbon dioxide were used for calculation of the longwave fluxes.

The atmosphere in the present model is divided into two layers. The net longwave flux at the surface is given by

$$L_s = \varepsilon_s \, B \, T_g^4. \tag{2.34}$$

The net longwave flux at 500 mb is

$$L_2 = \varepsilon_2 \, B \, T_2^4, \tag{2.35}$$

and the net longwave flux at the top of the model's atmosphere is

$$L_3 = \varepsilon_4 \, B \, T_2^4. \tag{2.36}$$

B is the Stefen-Boltzman constant. ε_s, ε_2 and ε_4 are the net emissivities at the surface, 500 mb and the top of the atmosphere, respectively.

Table 2.1

Parameters Used for Solar Radiation Calculations

Parameter Latitude	Clouds c	Atmospheric Albedo (r_a)	Surface Albedo (r_s)
84.1	0.35	0.096	0.8
76.5	0.41	0.129	0.8
68.9	0.48	0.179	0.8
61.3	0.54	0.305	0.4
53.6	0.56	0.343	0.3
45.9	0.54	0.316	0.2
38.3	0.45	0.248	0.2
30.6	0.37	0.185	0.18
23.	0.28	0.131	0.15
15.3	0.29	0.145	0.14
7.7	0.32	0.167	0.14
0.	0.38	0.207	0.14
-7.7	0.36	0.193	0.12
-15.3	0.35	0.183	0.1
-23.0	0.34	0.166	0.1
-30.6	0.36	0.179	0.1
-38.3	0.42	0.227	0.1
-45.9	0.51	0.293	0.1
-53.6	0.60	0.377	0.5
-61.3	0.62	0.369	0.5
-68.9	0.55	0.6	0.6
-76.5	0.47	0.6	0.6
-84.1	0.40	0.6	0.6

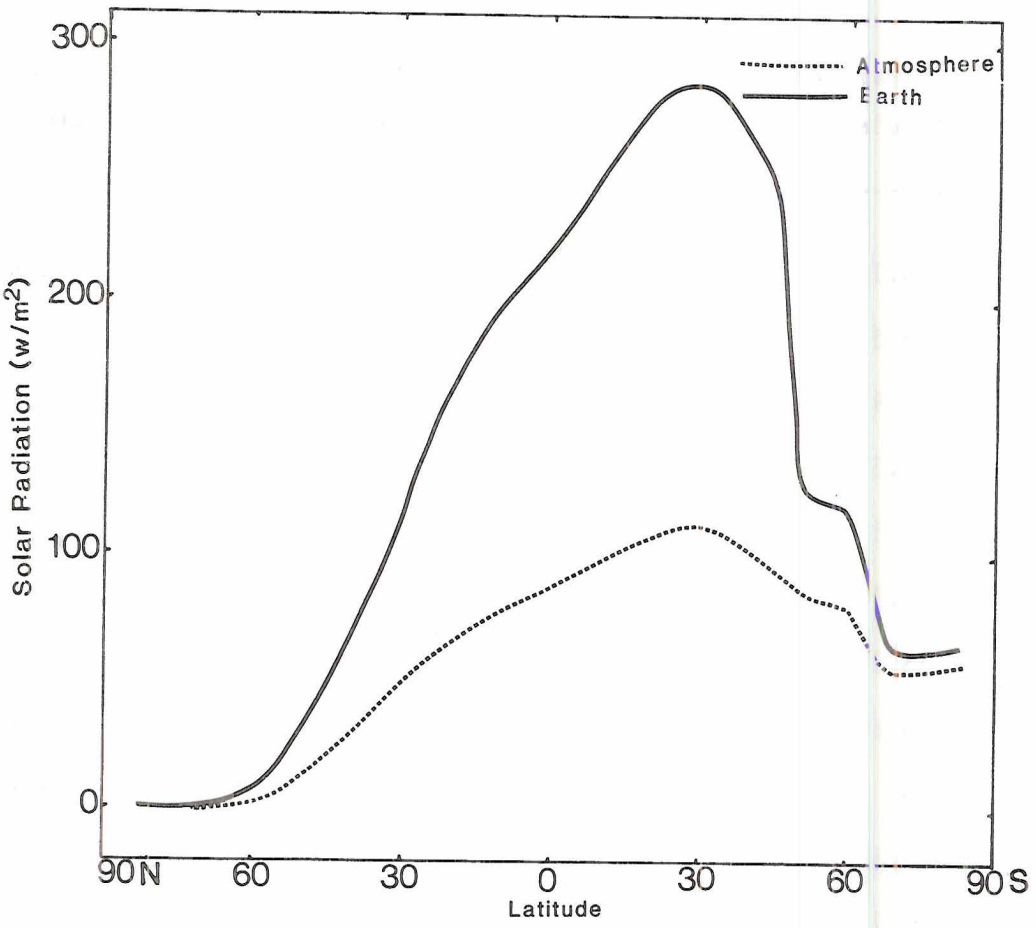

2.4 The zonal average of the calculated solar radiation (W/m^2) absorbed by the atmosphere (dotted line) and the earth (full line) for the first of January.

Based on the Stone-Manabe model, the net emissivities were assigned the values

$\varepsilon_s = 0.26$,

$\varepsilon_2 = 0.74$,

and $\varepsilon_4 = 0.11$.

Thus, the longwave heating rate of the lower layer is

$$(QL)_1 = \frac{g}{\Delta p} (L_s - L_2), \tag{2.37}$$

and the longwave heating rate of the upper layer is

$$(QL)_3 = \frac{g}{\Delta p} (L_2 - L_3). \tag{2.38}$$

2.7 Surface Temperature

The bulk formulae (2.24) and (2.25) require the surface temperature T_g. Over land and ice surfaces the temperature is calculated from the thermal energy equilibrium on the surface, assuming negligible heat capacity of the earth (Holloway and Manabe, 1971). The net solar radiation absorbed by the earth's surface (S_s), the sensible heat exchange with the lower layer (Q_s), the longwave emission of the earth's surface and the latent heat due to evaporation from the surface (Q_e) are in balance;

$$S_s = \varepsilon_s B T_g^4 + Q_s + Q_e + I(T_g - 271.2°). \tag{2.39}$$

The last term on the right side represents the conduction of heat from unfrozen water below sea ice in the polar latitudes of the winter hemisphere. Assuming a thermal conductivity of ice, $T_c = 2.1$ J m^{-1} °K^{-1} sec^{-1}, a temperature of the underlying water of 271.2°K, and an ice depth, $d = 2$ m, then the constant $I = T_c/d = 1.05$ W/m^2°K^{-1}. This term is needed to prevent unrealistically cold temperatures in the Northern Hemisphere polar regions during winter.

Equation (2.39) is solved over land and sea ice areas using Newton's iteration method (Appendix I).

Over the oceans the sea surface temperatures are specified using the mean January climatological values. Since the variation of sea surface temperatures between late winter and early spring is small, we keep these temperatures unchanged during the three month simulation (January, February and March).

2.8 Large Scale Precipitation and Convective Adjustment

The model has a moisture content in the lower layer (level 1) only. The procedure for large scale precipitation and the convective adjustment starts after completing each time step of integration. The mixing ratio harmonics are transformed to physical space, and then the model's atmosphere is examined for super saturation at each grid point.

If $q(T_1) < \gamma q_s(T_1)$, then no precipitation or convective adjustment takes place. The parameter γ represents a specified critical relative humidity ($\gamma = 0.85$ in this study), T_1 is the temperature at any grid point in level 1, and q and q_s are the mixing ratio and the saturation mixing ratio, respectively.

On the other hand, if $q(T_1) \geq \gamma q_s(T_1)$, condensation occurs with the associated latent heat release. The temperature T_1 will be agumented by an increment ΔT, such that

$$\Delta T = \frac{L}{c_p} \left(q(T_1) - q_s'(T + \Delta T)\right), \tag{2.40}$$

where q_s' is the new saturation mixing ratio at the temperature $T + \Delta T$,

$$q_s' = \gamma q_s + \gamma \frac{\partial q_s}{\partial T} \Delta T. \tag{2.41}$$

Using the Clausius-Clapeyron equation, (2.41) takes the form

$$q_s' = \gamma q_s + \gamma \frac{L q_s}{R_v T^2} \Delta T \tag{2.42}$$

where R_v is the water vapor gas constant. The rate of condensation (precipitation) per unit mass, P_c, is given by

$$P_c = (q - q_s')/\Delta t,$$

where Δt is the time step of integration. Using (2.40) and (2.42)

$$P_c = \frac{q - \gamma q_s}{\Delta t} / \left(1 + \frac{\gamma L^2}{c_p R_v T^2} q_s\right). \tag{2.43}$$

It is clear that a relevant form of (2.40) is

$$\Delta T = \frac{L}{c_p} P_c \Delta t. \tag{2.44}$$

After the release of latent heat in the lower layer as a result of the condensation of water vapor, the atmosphere is tested to see if convective adjustment is required. Convection is assumed to develop if the atmosphere is unstable relative to the moist adiabatic lapse rate Γ_s. If the temperature lapse rate is greater than Γ_s, then the temperature of the two levels are adjusted to stabilize the model's atmosphere by cooling the lower layer and warming the upper layer, with the vertically averaged temperature conserved. The new lapse rate is the same as Γ_s.

2.9 Model Equations

The system of equations (2.1 - 2.6) together with the vertical boundary conditions discussed before (Section 2.3) are expanded at levels 1 and 3 of the model. We use the average values $\psi = (\psi_1 + \psi_3)/2$ and $\theta = (\theta_1 + \theta_3)/2$ by adding the two systems of equations at the two

levels. The difference equations for $\tau = (\psi_3 - \psi_1)/2$ and $\sigma = (\theta_3 - \theta_1)/2$ are calculated by subtracting the equations in both layers. For consistency of notation we introduce χ_1 such that $\chi \equiv \chi_1$. Thus, the system (2.1 - 2.6) will reduce to the following:

$$\frac{\partial}{\partial t}(\nabla^2\psi) = -J(\psi,\nabla^2\psi+f) - J(\tau,\nabla^2\tau) - \tfrac{1}{2}\nabla\cdot f\nabla\chi_s + \bar{F}_h + \bar{F}_v, \tag{2.45}$$

$$\frac{\partial}{\partial t}(\nabla^2\tau) = -J(\psi,\nabla^2\tau) - J(\tau,\nabla^2\psi+f) + \nabla\cdot f\nabla\chi - \tfrac{1}{2}\nabla\cdot f\nabla\chi_s + \hat{F}_h + \hat{F}_v, \tag{2.46}$$

$$\frac{\partial\theta}{\partial t} = -J(\psi,\theta) - J(\tau,\sigma) + \nabla\cdot(\sigma\nabla\chi) - \tfrac{1}{2}(\nabla\chi_s\cdot\nabla\theta + \nabla\chi_s\cdot\nabla\sigma + 3\sigma\nabla^2\chi_s) + \bar{Q} + \bar{W}_h, \tag{2.47}$$

$$\frac{\partial\sigma}{\partial t} = -J(\psi,\sigma) - J(\tau,\theta) + \nabla\chi\cdot\nabla\theta - \tfrac{1}{2}(\nabla\chi_s\cdot\nabla\theta + \nabla\chi_s\cdot\nabla\sigma - \sigma\nabla^2\chi_s) + \hat{Q} + \hat{W}_h, \tag{2.48}$$

$$\frac{\partial q}{\partial t} = -\nabla\cdot((\kappa\times\nabla(\psi-\tau)+\nabla\chi)q) + E - P_c + (S_h)_1, \tag{2.49}$$

$$bc_p\nabla^2\theta = \nabla\cdot(f\nabla\tau), \tag{2.50}$$

and

$$\nabla^2\chi_s = -2\underline{v}_s\cdot\nabla\eta, \tag{2.51}$$

where $b = \frac{1}{2}[(\frac{3}{4})^\kappa - (\frac{1}{4})^\kappa] = .124$.

This is a system of seven equations with seven unknowns

$$\psi,\ \tau,\ \theta,\ \sigma,\ \chi_1,\ \chi_s,\ q.$$

All the budget values $\bar{F}_h$, $\hat{F}_h$, $\bar{F}_v$, $\hat{F}_v$, $\bar{W}_h$, $\hat{W}_h$, S_1, E, P_c, $\bar{Q}$ and $\hat{Q}$ are either specified or calculated, as discussed previously.

$$\bar{F}_h + \bar{F}_v = -\frac{k_s}{2}\nabla^2\psi_s + k_h(\nabla^4\psi + 2\frac{\nabla^2\psi}{a^2}) \tag{2.52}$$

$$\hat{F}_h + \hat{F}_v = \frac{k_s}{2}\nabla^2\psi_s - 2k_d\nabla^2\tau + k_h(\nabla^4\tau + \frac{2}{a^2}\nabla^2\tau) \tag{2.53}$$

$$\bar{W}_h = k_h\nabla^2\theta \tag{2.54}$$

$$\hat{W}_h = k_h \nabla^2 \sigma \tag{2.55}$$

$$(S_h)_1 = k_h \nabla^2 q \tag{2.56}$$

$\bar{Q}$ is the vertically averaged diabatic heating per unit mass, and $\hat{Q}$ is the difference in the diabatic heating between the two levels.

$$\bar{Q} = \tfrac{1}{2}\left[\left[\frac{p_o}{p_1}\right]^K Q_1 + \left[\frac{p_o}{p_3}\right]^K Q_3\right] \tag{2.57}$$

$$\hat{Q} = \tfrac{1}{2}\left[\left[\frac{p_o}{p_3}\right]^K Q_1 - \left[\frac{p_o}{p_1}\right]^K Q_3\right] \tag{2.58}$$

The surface stream function is extrapolated from the values at the two levels assuming that ψ is linear with height (Salmon and Hendershott, 1976).

$$\psi_s = \psi - 1.6\tau \tag{2.59}$$

The above system represents the structure of the model. This system will be transformed to the spectral space using the spherical harmonics as basis functions.

2.10 Spectral and Finite Difference Methods

The conventional spectral method is Galerkin's method based on expanding the different variables with a truncated series of surface spherical harmonics. The method is used for the numerical integration of the hydrodynamical equations. Two types of expansion are often used, the triangular and rhomboidal truncations. The advantages of the spectral method over the usual finite difference methods are summarized as follows (Machenhauer, 1974):

1) The non-linear terms are alias free, which prohibits the existence of the non-linear instability described by Phillips (1959).

2) Quadratic area integral invariants like the kinetic energy and enthalpy also are invariant for the truncated system, since the error fields are orthogonal to the variables.

3) Linear terms are computed without any truncation error.

4) No special treatment is required for dealing with the polar region when using the vorticity and divergence fields. By contrast, in the finite difference method the horizontal wind components are discontinuous at the pole.

5) The friction term of the finite difference methods is necessary to prevent aliasing instability. It also is necessary for the removal of energy from the shortwave end of the spectrum. When using the spectral method, it also is important to prevent blocking of energy at the highest wave numbers retained, but in this case the purpose is only a simulation of the effect of the small scales not retained in the representation.

A study by Hoskins and Simmons (1974) compared finite difference and spectral models. The study showed that no one method has a superiority in all respects. In comparison with the finite difference model, the spectral model gave much improved solutions for the amplitudes and phases of the predicted waves. On the other hand, the finite difference model gave a more accurate representation of the frontal systems.

It is of interest to compare the two types of truncation mentioned before, namely the rhomboidal and triangular. For the same zonal wave number truncation, the triangular representation has fewer degrees of freedom than the rhomboidal and hence requires less computing time. If we retain the same degrees of freedom in both the triangular and rhomboidal truncations, the former will be more appropriate for mean zonal

fields than the latter. At the same time the rhomboidal truncation could introduce higher wave numbers, namely the eddies. The same study by Hoskins and Simmons (1974) did not give a definite conclusion concerning the comparison between rhomboidal and triangular truncation. In some experiments the rhomboidal truncation gave a more accurate approximation to the solution than the triangular truncation. In other experiments the triangular truncation gave a more efficient description of Rossby wave instability.

In this study we used the rhomboidal truncation since it gives a comparable resolution in both horizontal directions.

2.11 Spectral Method

The dependent variables ψ, τ, χ, χ_s, θ, σ, q are expanded in truncated series of the form

$$X(\mu,\lambda) = \sum_{m=-M}^{M} \sum_{n=|m|}^{|m|+J} X_n^m \, Y_n^m \, (\mu,\lambda) \tag{2.60}$$

where X is any variable being studied, X_n^m are harmonic coefficients, λ is longitude, μ is the sine of latitude, m is the zonal wavenumber, n is the degree of a spherical harmonic component, $|n-m|$ is a meridional wavenumber in the sense that there are $|n-m|$ zero crossings of Y_n^m between equator and pole, M is the highest zonal wave number retained in the truncated series, and J is the highest value of $|n-m|$ retained in the truncated series. Y_n^m are spherical harmonic functions defined by

$$Y_n^m = P_n^m (\mu) \, e^{im\lambda}. \tag{2.61}$$

P_n^m are the Associated Legendre functions of the first kind

$$P_n^m(\mu) = \left(\frac{(2n+1)}{4\pi} \frac{(n-m)!}{(n+m)!}\right)^{\frac{1}{2}} \frac{(1-\mu^2)^{m/2}}{2^n n!} \frac{d^{n+m}}{d\mu^{n+m}} (\mu^2-1)^n \tag{2.62}$$

A spherical harmonic coefficient is defined by

$$X_n^m = \frac{1}{4\pi} \int_0^{2\pi} \int_{-1}^{+1} X \, Y_n^{m*} \, d\mu d\lambda \tag{2.63}$$

where Y_n^{m*} is the complex conjugate of Y_n^m.

Y_n^m are orthogonal over the surface of the sphere, i.e

$$\frac{1}{4\pi} \int_0^{2\pi} \int_{-1}^{+1} Y_n^m \, Y_{n_1}^{m_1*} \, d\mu d\lambda = \begin{cases} 1 \text{ for } (m_1,n_1) = (m,n) \\ 0 \text{ for } (m_1,n_1) \neq (m,n) \end{cases}, \tag{2.64}$$

and are eigenfunctions of the Laplacian operator

$$\nabla^2 Y_n^m = - n \frac{(n+1)}{a^2} Y_n^m, \tag{2.65}$$

where a is the radius of the sphere. The coefficients for negative and positive values of m are related in the following way:

$$X_n^{-m} = (-1)^m X_n^{m*}.$$

Nonlinear terms are transformed from grid point space to spectral space using the full transform method (Machenhauer and Rasmussen, 1972; Orszag, 1970). The method is computationally highly efficient relative to the interaction coefficient method for $J \geq 9$.

The procedure for calculating the spectral coefficients of the nonlinear terms using the full transform method is as follows:

1) Calculate the nonlinear terms at each grid point in physical space.

2) Transform to the Fourier space at each Gaussian latitude, using fast Fourier transform routines.

3) Transform to the spectral space using the Gaussian quadrature formula.

Highly nonlinear terms, like diabatic heating terms cause problems in finding their spectral transforms. This problem is resolved by using the full transform method. They are calculated in physical space, then added to the nonlinear dynamic terms, and the whole sum is transformed to spectral space.

To guarantee an alias-free solution, there are two conditions that must be fulfilled (Machenhauer and Rasmussen, 1972). These conditions specify the minimum number of zonal grid points, N_g, and the minimum number of Gaussian latitudes, I_s, on the sphere:

$$N_g > 3\,M + 1$$

$$I_s > M + 3/2\,J.$$

In case of the rhomboidal truncation (M = J) used here, the latter condition is

$$I_s > 5/2\,M.$$

For the simulation with wavenumber 9, $N_g = 32$ and $I_s = 23$.

To transform the system (2.45 - 2.51) to its spectral form, each variable is expanded using (2.60). The resulting equations are multiplied by Y_n^{m*} and integration of both sides is performed using equations (2.63 - 2.65). The nonlinear terms are calculated using the transform method mentioned before.

The system of equations in its spectral form is given by

$$\dot{\psi}_n^m = -\frac{a^2}{n(n+1)}\{-J(\psi,\nabla^2\psi) - J(\tau,\nabla^2\tau)\}_n^m + \frac{2\Omega m}{n(n+1)}\,i\,\psi_n^m -$$

$$\Omega\left(\frac{n+2}{n+1}\,D_{n+1}^m\,\chi_{s\,n+1}^{\;m} + \frac{n-1}{n}\,D_n^m\,\chi_{s\,n-1}^{\;m}\right) \qquad (2.66)$$

$$-\frac{k_s}{2}\,\psi_{s\,n}^{\;m} - K_h\,n\,\frac{(n+1)}{a^2}\,\psi_n^m + \frac{2k_h}{a^2}\,\psi_n^m\,,$$

$$\dot{\tau}_n^m = \frac{-a^2}{n(n+1)} \{(-J(\tau,\nabla^2\psi) - J(\psi,\nabla^2\tau))\}_n^m + \frac{2\Omega m}{n(n+1)} i\ \tau_n^m -$$

$$\Omega\ (\frac{n+2}{n+1}\ D_{n+1}^m\ \chi_{s\ n+1}^{\ m} + \frac{n-1}{n}\ D_n^m\ \chi_{s\ n-1}^{\ m})$$

$$+ \frac{k_s}{2}\ \psi_{s\ n}^{\ m} - 2k_d\ \tau_n^m - k_h\ n\ \frac{(n+1)}{a^2}\ \tau_n^m + \frac{2k_h}{a^2}\ \tau_n^m \qquad (2.67)$$

$$+ 2\Omega\ (\frac{n+2}{n+1}\ D_{n+1}^m\ \chi_{n+1}^m + \frac{(n-1)}{n}\ D_n^m\ \chi_{n-1}^m),$$

$$\dot{\theta}_n^m = \{-J(\psi,\theta) - J(\tau,\sigma) - \tfrac{1}{2}(\nabla\chi_s\cdot\nabla\theta + \nabla\chi_s\cdot\nabla\sigma + 3\sigma\nabla^2\chi_s)\}_n^m$$

$$- n\ \frac{(n+1)}{a^2}\ k_h\ \theta_n^m + (\nabla\cdot(\sigma\nabla\chi))_n^m + \bar{Q}_n^m\ , \qquad (2.68)$$

$$\dot{\sigma}_n^m = \{-\ J(\psi,\sigma) - J(\tau,\theta) - \tfrac{1}{2}(\nabla\chi_s\cdot\nabla\theta + \nabla\chi_s\cdot\nabla\sigma - \sigma\nabla^2\chi_s)\}_n^m$$

$$+ (\nabla\chi\cdot\nabla\theta)_n^m - n\ \frac{(n+1)}{a^2}\ k_h\ \sigma_n^m + \hat{Q}_n^m\ , \qquad (2.69)$$

$$\dot{q}_n^m = -\ (\nabla\cdot((k\times\nabla(\psi-\tau) + \nabla\chi)q))_n^m - n\ \frac{(n+1)}{a^2}\ k_h\ q_n^m + (E-P_c)_n^m, \qquad (2.70)$$

$$b\ c_p\ \theta_n^m = 2\Omega(\frac{n+2}{n+1}\ D_{n+1}^m\ \tau_{n+1}^m + \frac{(n-1)}{n}\ D_n^m\ \tau_{n-1}^m), \qquad (2.71)$$

$$\psi_{s\ n}^{\ m} = \psi_n^m - 1.6\ \tau_n^m, \qquad (2.72)$$

and

$$\chi_{s\ n}^{\ m} = \frac{a^2}{n(n+1)}\ (\underline{v}_s\cdot\nabla\eta)_n^m, \qquad (2.73)$$

where $i = \sqrt{-1}$. The spectral transform of terms of the form $\nabla\cdot(f\nabla\tau)$ or $\nabla\cdot(f\nabla\chi)$ is shown in Appendix (II).

It must be noted that by solving (2.67), (2.68) and (2.71) we can obtain an equation for χ. The equations are simplified and solved as a system of tridiagonal matrices to find the spectral coefficients of χ that satisfy the linear balance approximation. The simplification is needed to treat the term $(\nabla\cdot\sigma\nabla\chi)$ in (2.68). To do this, we split σ into its global average $[\sigma]$, and the deviation from this average σ',

$$\sigma = [\sigma] + \sigma'.$$

Then

$$\nabla\cdot(\sigma\nabla\chi) = [\sigma]\nabla^2\chi + \nabla\cdot(\sigma'\nabla\chi).$$

The first term on the right side of the above equation is of a larger order of magnitude and is added to the other unknown terms, which include χ. The smaller, second term, is considered as a known parameter and calculated using the values of χ at the previous time step. The method is found to be stable. It significantly reduces the number of calculations at this stage.

2.12 Energetics of the Model

The two layer model discussed here conserves the sum of kinetic and available potential energy under reversible adiabatic processes (Lorenz, 1960). If one introduces the topographical forcing as a lower boundary vertical velocity, it is hard to verify the energy conservation (Burger and Riphagen, 1979). It is only the very simple lower boundary condition $\omega_s = 0$ (used by Lorenz) at $p = 1000$ mb that guarantees an energy-conserving system.

The kinetic and available potential energies, KE and AP, respectively, are expressed in the forms

$$KE = \frac{\Delta p}{g}(\nabla\psi\cdot\nabla\psi + \nabla\tau\cdot\nabla\tau) \tag{2.74}$$

and

$$AP = \frac{2b\ c_p\ \Delta p}{g}\ \frac{[(\theta')^2 + (\sigma')^2]}{[\sigma] + [\sigma^2 + (\theta')^2 + (\sigma')^2]^{\frac{1}{2}}}\ . \tag{2.75}$$

The square brackets [ ] indicate the global area average and the 's indicate the deviation from that average.

In spectral space the kinetic and available potential energy within a spherical harmonic mode are given by

$$(KE)_n^m = \frac{\Delta p}{ga^2}\ (\psi_n^{m\ 2} + \tau_n^{m\ 2})\ n(n+1)\ (2-\delta_{om}),\ \text{for } m \geq 0 \tag{2.76}$$

and

$$(AP)_n^m = \frac{2b\ c_p\ \Delta p}{g}\ \frac{(\theta_n^{m\ 2} + \sigma_n^{m\ 2})\ (2-\delta_{om})}{\sigma_o^o + \{\sum\sum_{rs} \theta_s^{r\ 2} + \sigma_s^{r\ 2} - \theta_o^{o2}\}^{\frac{1}{2}}}\ , \tag{2.77}$$

for $n \neq 0$ $m \geq 0$, where $\delta_{oo} = 1$ and $\delta_{om} = 0$ for $m > 0$.

2.13 Initial Conditions and Time Integrations

The model integration starts from a hypothetical, horizontally isothermal, atmosphere at rest with a moist adiabatic lapse rate. The model runs for sixty days assuming perpetual solar forcing (first of January). This initialization procedure is used in order to reach a statistically steady state. After that the solar declination is changed daily to simulate the climates of January (days 61-90), February (days 91-120), and March (days 121-150). These runs are considered as control runs for the comparable periods within the experiments.

The time difference method used is the centered (leap-frog) scheme. To avoid the growth of unnecessary computational modes, a time smoother was used on the prognostic variables (Asselin, 1972) at every time step.

The diffusion terms were calculated using values at the previous time step to ensure computational stability. The time step used was 2 hours.

2.14 The Quasi-Geostrophic Versus Primitive Equation Model

The dominant energies of the ultra-longwaves (zonal wave numbers 1-4) and longwaves (wave numbers 5-9) are quasi-geostrophic. The quasi-geostrophic approximation assumes near-balance between the Coriolis force and the pressure gradient force. This balance between the two forces enables us to ignore the time variation of the horizontal divergence among other terms in the divergence equation. The magnitude of the velocity potential (χ) is about an order of magnitude less than that of the stream function (ψ). This also was noticed in results of the present model concerning the two variables. The relatively high frequency gravity waves are filtered. The filtering of the gravity waves gives the advantage of using a large time step when the prognostic equations are numerically integrated. Using the primitive equations requires a much smaller time step to satisfy the stability conditions, unless the semi-implicit scheme is used. Even with that procedure, the time step is less than the one used in filtered models of the same resolution. The quasi-geostrophic models have been used for prediction of middle latitude circulations where the ultra-longwaves and longwaves are well defined by the balance between the two forces mentioned above.

2.14.1 Scale Analysis

The conditions under which the primitive equations could be reduced to the quasi-geostrophic system can be summarized as (e.g., Phillips, 1963)

1) $R_o \ll 1$

2) $BG \equiv R_o^2 R_i \sim 1$,

where R_o and R_i are the Rossby and Richardson numbers, respectively, and BG is the Burger number. These nondimensional numbers are defined as follows:

$$R_o = \frac{U}{fL},$$

$$R_i = \frac{gH}{U^2}\left(\frac{\Delta\rho}{\rho}\right),$$

$$BG = \frac{gh}{4\Omega^2 L^2}\left(\frac{\Delta\rho}{\rho}\right).$$

In these equations, U is the horizontal velocity; L is the horizontal scale; H is the vertical scale; Ω is the angular velocity of the earth; f is the Coriolis parameter; g is the acceleration of gravity, and $\left(\frac{\Delta\rho}{\rho}\right)$ refers to the vertical density stratification. The second condition implies that $R_o \cong \frac{1}{\sqrt{Ri}}$ which cannot be fulfilled in the tropics since R_i has a typical value of nearly 40 for atmospheric long and ultra long-waves.

In this model the variability of f with latitude is retained. Due to the larger values of R_o in the equatorial regions, the quasi-geostrophic model cannot detect many features of the tropical circulation.

2.4.2 Effect of Filtering the Gravity Waves

Besides the question of validity of the geostrophic approximation in tropical regions, it is also necessary to discuss the effect of filtering gravity waves on the tropical circulation. The most important type is the Kelvin wave. In the longitude-height plane a Kelvin wave is simply an ordinary internal gravity wave which propagates downward and eastward in the tropical stratosphere. Kelvin waves may provide a westerly momentum source for the semiannual oscillation. There is no

direct observational evidence linking the stratospheric Kelvin waves to any weather disturbances in the troposphere (Holton, 1976). There are some theoretical studies, using linear primitive equation models, that tend to explain the east-west tropical Walker Circulation in terms of propagation of Kelvin waves (e.g., Gill, 1980). In all such studies, the Rayleigh friction in the troposphere was assumed to be very high as compared to the observed values.

2.14.3 Validity of the Model for the Proposed Study

Although a nonlinear quasi-geostrophic model will not represent the tropical circulation as accurately as a primitive-equation model, the former can be used efficiently as a general circulation model to study the response of the midlatitude atmosphere to lower boundary forcing in the tropics. A nonlinear quasi-geostrophic model will be more applicable than a linear primitive equation model for such studies. This statement is deemed true since the atmosphere itself is highly nonlinear. Also, for a quasi-geostrophic model the fulfillment of the energy constraints and the large time step used are both desirable in long term integrations. Semi-implicit schemes give the advantage of using large time steps in the case of the primitive equation models. However, they still use smaller time steps than those used by a quasi-geostrophic model of the same resolution. The planetary Rossby waves, which are the major modes representing motions away from the equator, are quasi-geostrophic in character. At the same time, it is not yet clear how the Kelvin waves affect, or interact with, the midlatitude planetary waves. In other words, the response of the midlatitude atmosphere to thermal heating in the tropics may not be affected by the

propagation of the Kelvin waves there. In the tropics the local response to the heating seems to be a direct type of circulation. In either case, many features of the tropical circulation could not be represented accurately with a two level model.

Based on the previous discussion, the present model appears to be suitable and efficient for studying the response of the large scale midlatitude atmosphere to thermal anomalies in the tropical regions.

3. COMPARISON OF THE MODEL'S WINTER CLIMATE WITH OBSERVATIONS

In order to gain an understanding of the limitations of the model, it is important to compare the model's climate with the observed large scale circulation. The simulated January climate is the 30 day average of days 61 through 90. February and March simulations are the integrations from day 91 to day 120 and from day 121 to day 150, respectively. In this period of integration from day 61 to day 150, the solar declination is changed daily as a function of the mean zenith angle mentioned in Chapter 2. These simulated monthly averages are considered as control runs for the proposed anomaly experiments.

In this chapter we will compare the simulated January circulation with the corresponding climatological fields for the same month. The Northern Hemisphere observed fields were taken from tables given by Oort and Rasmusson (1971). For some fields the values from 10°S to the south pole are taken from the observed December-February average values (Newell et al., 1972).

When comparing the simulated and observed fields we must keep in mind the type of approximations and simplifications assumed in constructing the model and also the aim and nature of this research. The dynamical simplifications include use of the linear balance model in order to filter out the gravity waves present in the system of primitive equations. The low order of truncation (truncated at zonal wave no. 9) excludes the higher wave numbers, which certainly affects the eddy statistics of the model. The vertical resolution of two levels is the

minimum required to allow baroclinic development. The physical simplifications include using zonal average values for the radiative forcing. For example, we assume a January climatological average for the surface albedo, atmospheric albedo, and cloud amount. The moisture budget was considered in the lower layer only. Such simplifications have their effects on the simulated climate of the model. Since we are mainly concerned with the response of the planetary and long waves in middle and high latitudes to different locations of the thermal anomalies, the model appears to be adequate The analysis of the experiments was done using the differences between the anomaly cases and the control run. Therefore the absolute values of the different fields are of secondary concern.

3.1 Average Zonal Values and Variances Resulting from Stationary and Transient Eddies

In this section we will consider the 30 day averages representing January, for different fields. The zonal averages and the variances resulting from stationary and transient eddies are compared with observations. In a two level model, the tropospheric average for linear parameters is represented by the values on the intermediate level (500 mb in the present model). Nonlinear parameters, like variances and transports, are calculated at each level; then are vertically averaged to represent the simulated tropospheric values.

To clarify the analysis, we define the following statistical relations for a certain variable X (Oort and Rasmusson, 1971):

The time average

$$\bar{X} = \frac{1}{\Delta t} \int_{t1}^{t_2} X dt \qquad (3.1)$$

Departure from the time average

$$X' = X - \bar{X} \tag{3.2}$$

Zonal Average

$$[X] = \frac{1}{2\pi} \int_0^{2\pi} X d\lambda \tag{3.3}$$

Departure from zonal average

$$X^* = X - [X] \tag{3.4}$$

The variance of X resulting from transient eddies

$$TX = \overline{[X'^2]} \tag{3.5}$$

The variance of X resulting from stationary eddies

$$SX = [\bar{X}^{*2}] \tag{3.6}$$

The calculation of the transient variances gives an indication of the development of disturbances in the model (i.e. the weather associated with the month of simulation). Naturally this variance will be more dominant in the middle and extratropical latitudes of the winter hemisphere. The stationary eddy component reflects the effects of the permanent forcing. This results mainly from the diabatic heating differences due to land and sea distributions and also the topographical gradients.

3.1.1 Zonal Wind Component

In the Northern Hemisphere the simulated 500 mb mean zonal wind is stronger than the observed values (Fig. 3.1). The maximum value appears at 30°N in agreement with observations, but it is 6 m sec^{-1} more than the observed maximum. In tropical latitudes the simulated belt of easterlies is shifted to the Southern Hemisphere, with an amplitude about 4 m sec^{-1} stronger than the observed. The simulation of the easterlies in the winter hemisphere seems to be a problem when using balance or quasi-

geostrophic dynamics (e.g. Wielicki and Hendershott, 1979; Kikuchi, 1969, 1979). In the Southern Hemisphere the simulated maximum westerlies are less than those revealed by observations. The characteristics of the simulated pattern in both hemispheres may be a result of the simulated temperature fields and the associated thermal wind components.

In general, the variance in the horizontal wind field is a measure of the eddy kinetic energy in the atmosphere, and, therefore, it is one of the basic parameters in the description of the climate. The simulated, vertically averaged variance of zonal wind resulting from the transient eddies has less amplitude than the observed pattern (Fig. 3.2). In the Northern Hemisphere, both the simulated and observed profiles have the same latitude of maximum variability (about 50°N). In the Southern Hemisphere (summer hemisphere) the simulated variance is generally small. The variance resulting from the stationary eddies (Fig. 3.3), has an amplitude which is comparable with observations, although its maximum is shifted about 10° equatorward within the Northern Hemisphere. Although the observational data are not available, the simulated stationary variances in the southern hemisphere seem to be in the correct position. Also they have less amplitude than the simulated Northern Hemisphere values.

3.1.2 Meridional Wind Component

The mean meridional circulation plays a central role in the operation of the general circulation of the atmosphere. Unfortunately, as stated by Oort and Rasmusson (1971), it has been a very difficult task to obtain a reliable estimate of the intensity of the mean meridional circulation. This results from the fact that the zonally averaged meridional wind component must be estimated from the divergent part of the

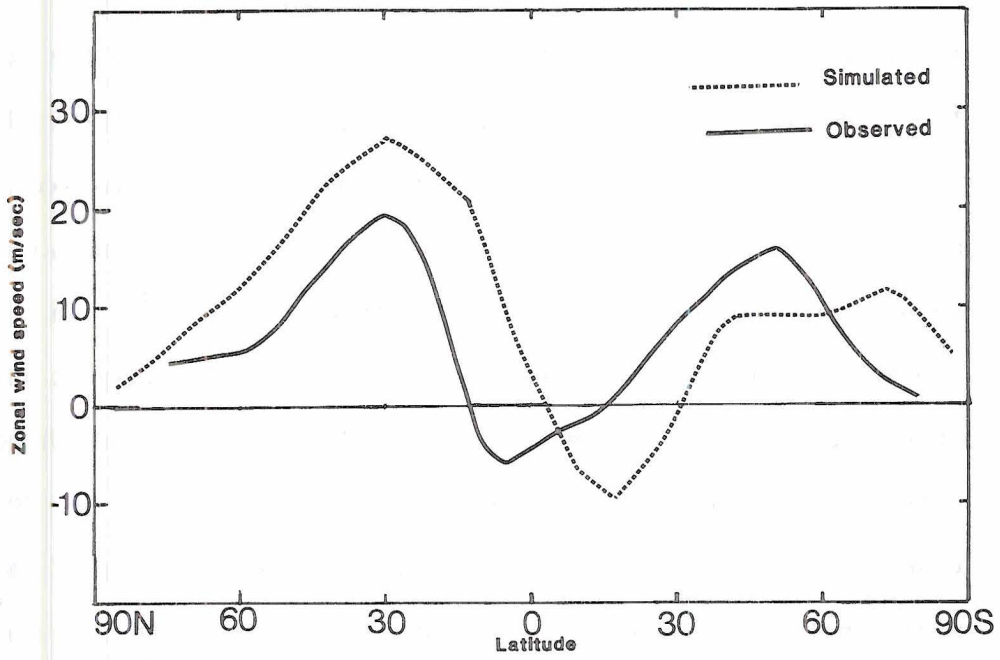

3.1 The zonal average of the observed (full line) and simulated (dotted line) zonal wind (m sec^{-1}) at 500 mb for January.

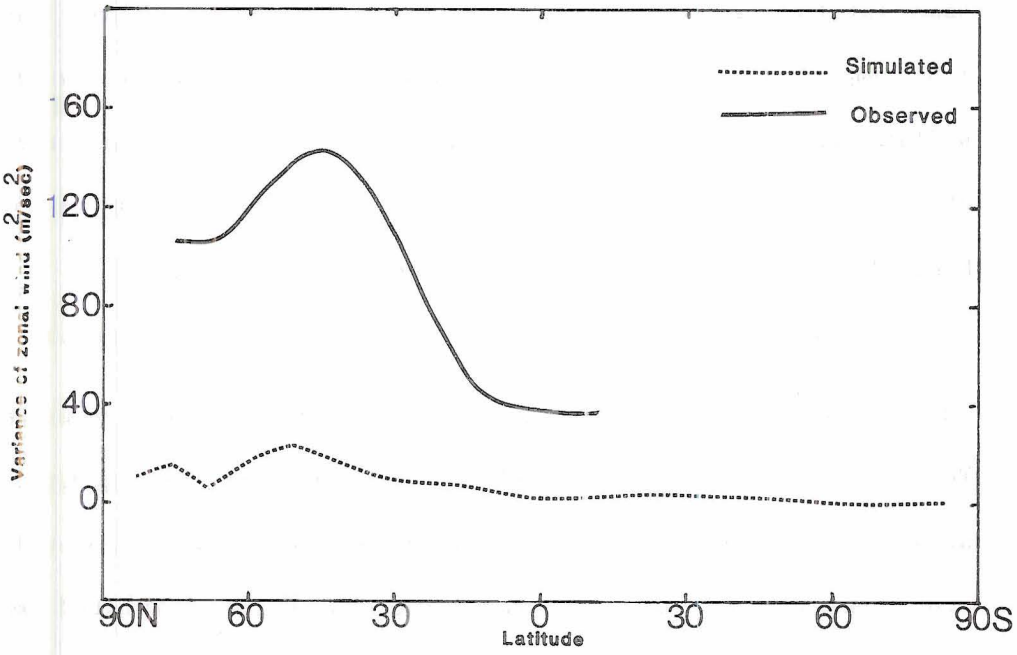

3.2 The tropospheric average of the observed (full line) and simulated (dotted line) zonally averaged variance of zonal wind ($m^2 sec^{-2}$) resulting from transient eddies for January.

wind field, which is generally of a lower order of magnitude than the rotational part in the middle and high latitudes. At the same time, in the tropical region, the zonally averaged velocity potential is hard to detect in the observed wind fields. The observed maximum 500 mb mean meridional wind compenent is about four times larger than the simulated value (Fig. 3.4), but still less than 1 m sec^{-1}. In the Northern Hemisphere, the simulated maximum southward mass transport is at 38.5°N, which agrees with observations. In the Southern Hemisphere the simulated pattern changes from southerlies to northerlies at 20°S, whereas observations show the change at 30°S. The small values of the simulated meridional wind component are partially a result of zonal average forcing used in the model, which underestimates the actual east-west differences.

The calculated variance due to transient eddies (Fig. 3.5) has the same latitudinal position of the maximum as the observed one, but with less amplitude. Both, the position and amplitude of the variance resulting from stationary eddies (Fig. 3.6) show a better agreement with observation. The positions of the simulated values in the Southern Hemisphere also seems to be in reasonable agreement.

It is of interest to note, the close similarity of the patterns of $[\overline{u'^2}]$ and $[\overline{v'^2}]$ for both the simulated and observed transient eddies. This indicates that the kinetic energy of the developing disturbances seems to be almost equally distributed among the zonal and meridional wind components. At the same time, both the simulated and observed fields do not show such similarity in the case of variances resulting from stationary eddies. In the Northern Hemisphere middle and extratropical latitudes, both the model and observations reveal that the transient components are larger than the standing components.

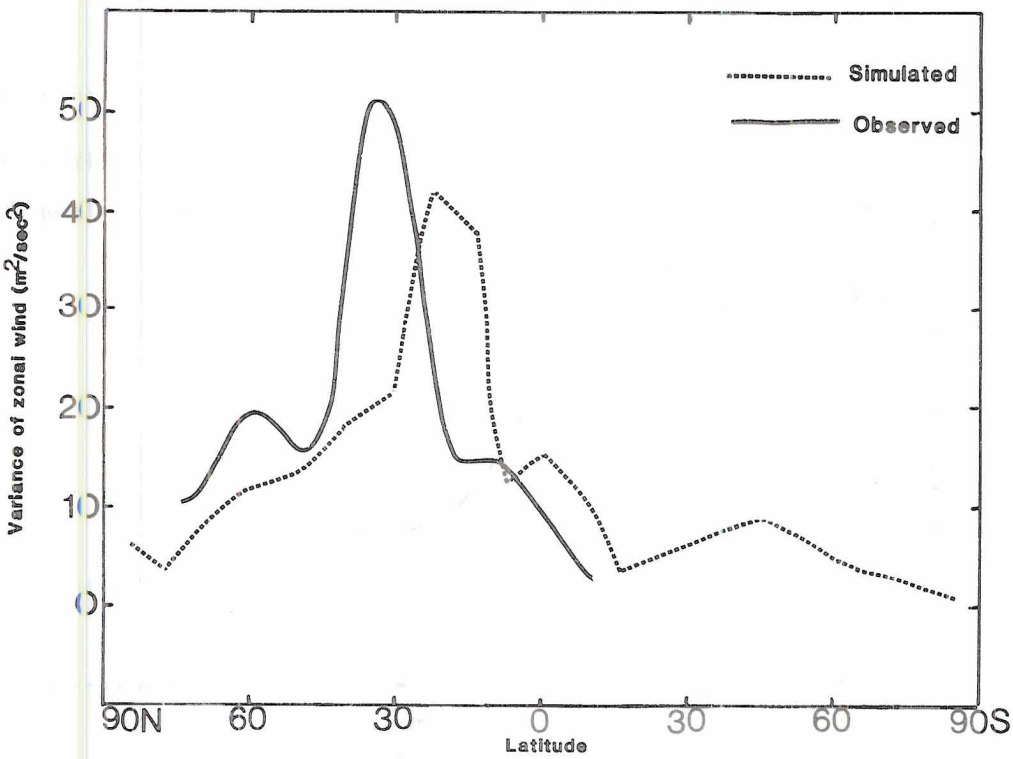

3.3 The tropospheric average of the observed (full line) and simulated (dotted line) zonally averaged variance of zonal wind ($m^2 sec^{-2}$) resulting from stationary eddies for January.

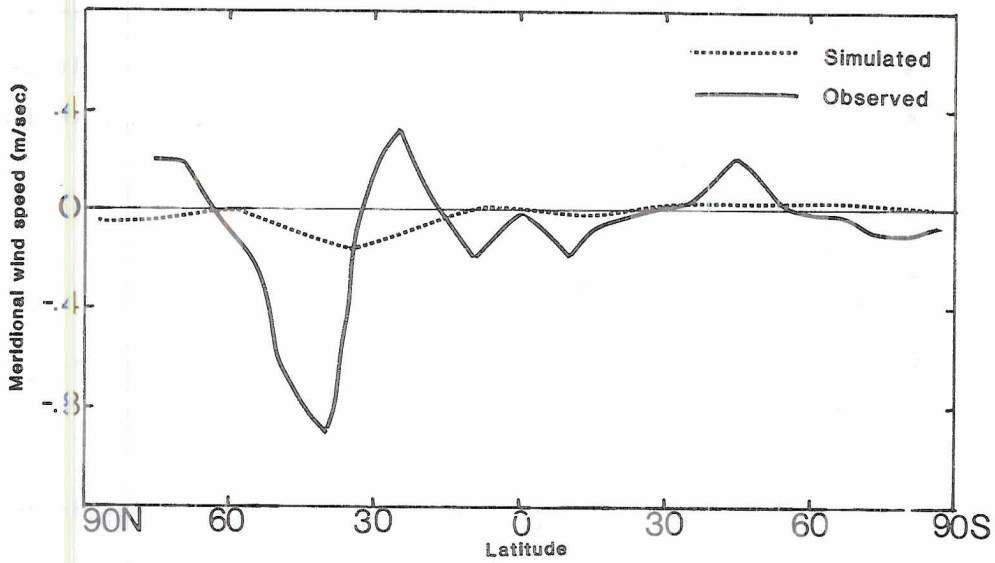

3.4 The zonal average of the observed (full line) and simulated (dotted line) meridional wind (m sec^{-1}) at 500 mb for January.

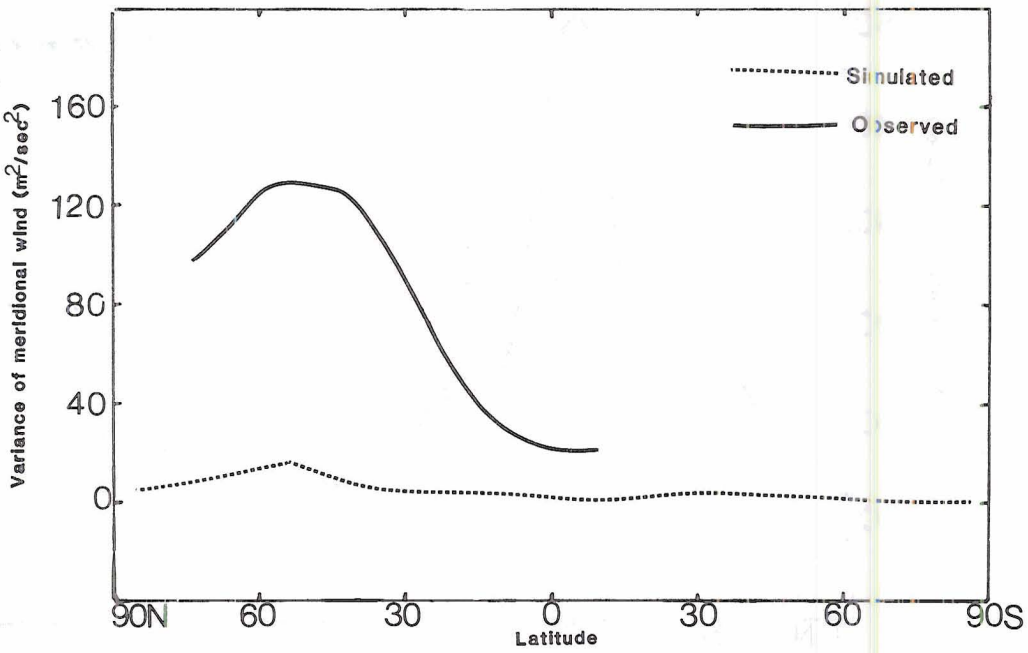

3.5 The tropospheric average of the observed (full line) and simulated (dotted line) zonally averaged variance of meridional wind ($m^2 sec^{-2}$) resulting from transient eddies for January.

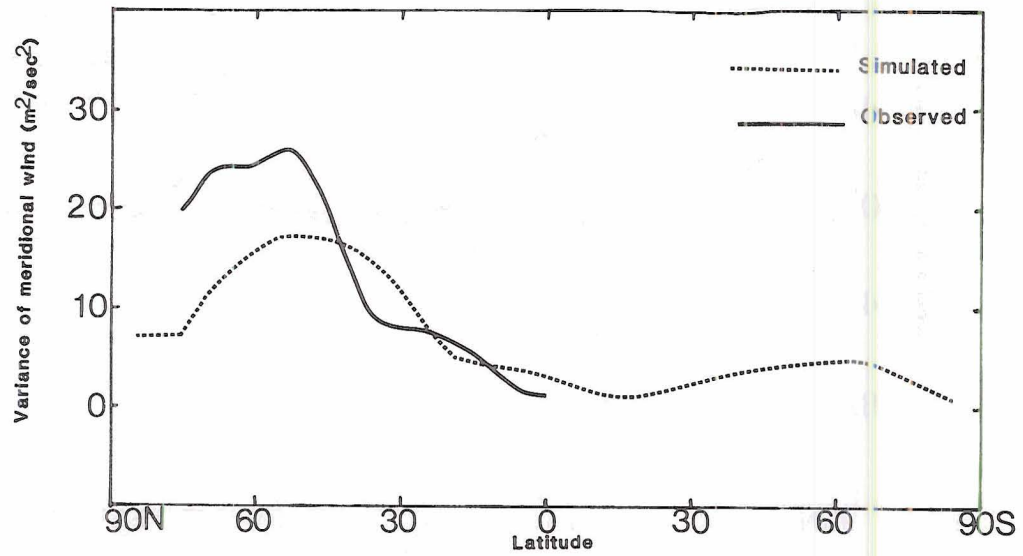

3.6 The tropospheric average of the observed (full line) and simulated (dotted line) zonally averaged variance of meridional wind ($m^2 sec^{-2}$) resulting from stationary eddies for January.

The simulated variance of horizontal wind resulting from transient eddies is smaller than that revealed by observations (nearly about 1 to 6). A part of this deficiency is due to the north-south horizontal resolution used in the model (Manabe et al., 1965).

3.1.3 Vertical Pressure Velocity

The observed values were calculated assuming a zero lower boundary pressure velocity. In other words, the effect of topography was not taken into account for the observed fields. In the Northern Hemisphere the major areas of subsidence appear to be in the subtropics for both the simulated and observed fields (Fig. 3.7). The simulated rising motion in the tropical Southern Hemisphere associated with the active convection there is broadened, but with lower magnitude, than shown by observations. However, the main differences between the observed and simulated zonal average vertical velocity are apparent in the extra-tropical latitudes of both hemispheres. In the winter hemisphere the latitude of maximum vertical motion seems to be shifted poleward about 12° from the observed maximum.

The geographic map for the simulated vertical motion (Fig. 3.8) shows that the model correctly simulates the position of the maximum rising motion over the eastern Pacific and Atlantic Oceans due to the effects of the Rocky Mountains and Alps, respectively. The Himalayas cause a rather noisy pattern over eastern Eurasia and the western Pacific. In the Southern Hemisphere the effect of the Andes also is clear over the South American continent. One should also note, the upward motion over the tropical western Pacific and the sinking motions over the eastern Pacific adjacent to the South American continent. This motion pattern may be interpreted as the vertical branch of a Walker

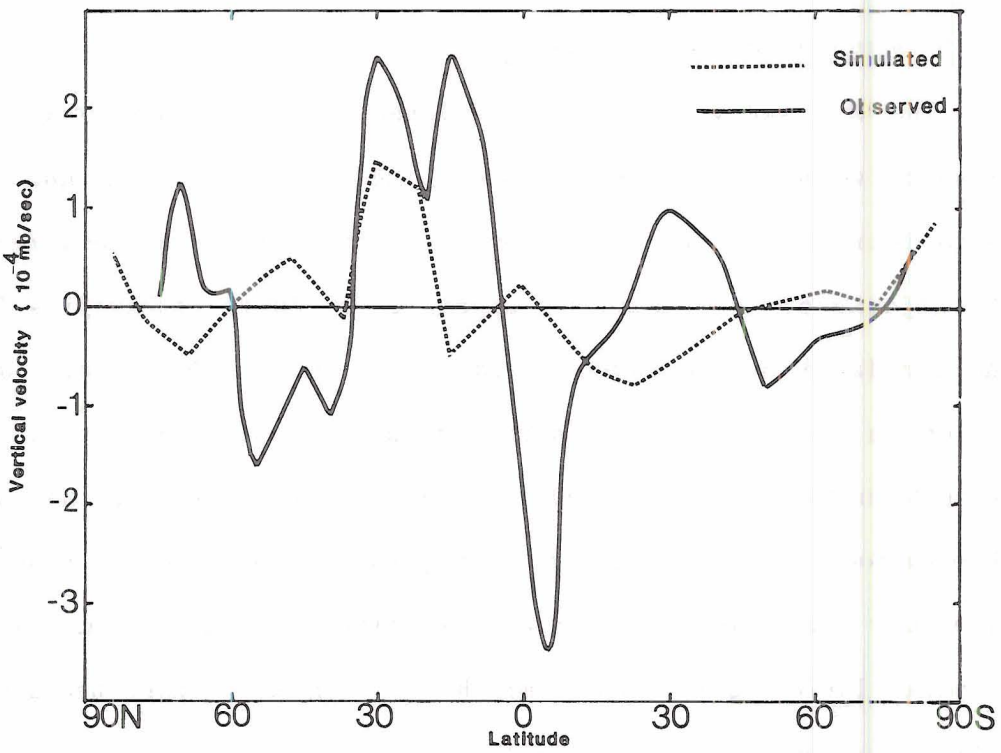

3.7 The zonal average of the observed (full line) and simulated (dotted line) vertical pressure velocity (10^{-4} mb sec^{-1}) at 500 mb for January (negative values upward, positive values downward).

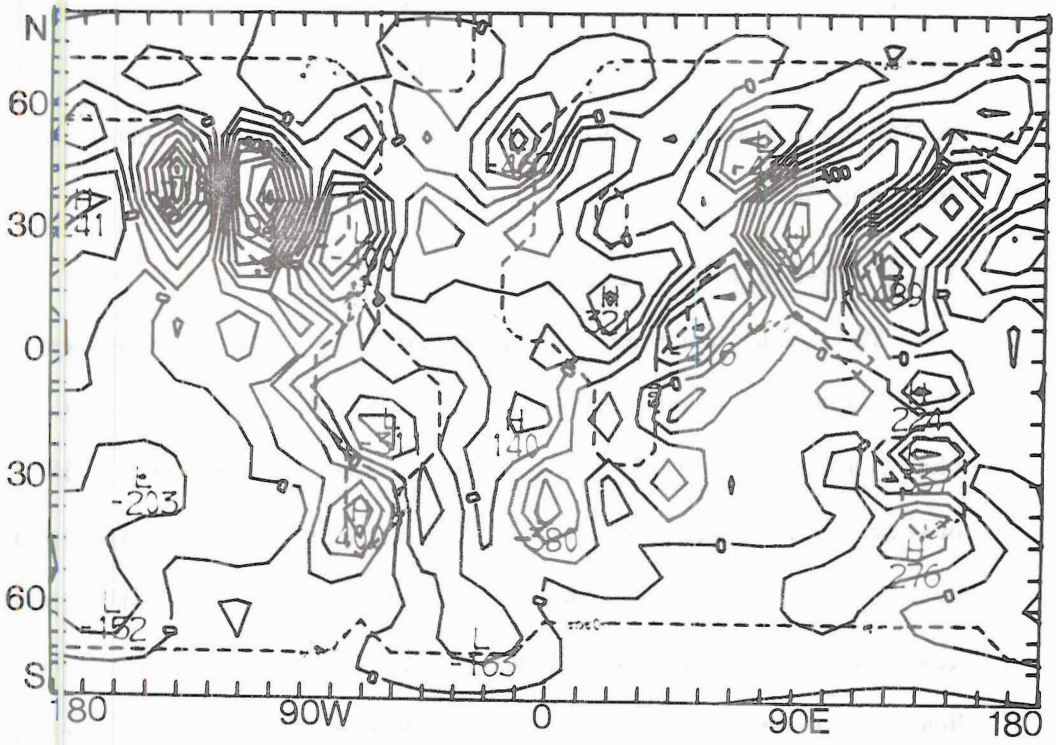

3.8 The simulated vertical pressure velocity at 500 mb (10^{-6} mb sec^{-1}) for January (negative values upward, positive values downward).

type circulation, although the Kelvin waves were filtered from the model's equations.

The zonal average variances resulting from stationary eddies (Fig. 3.9) show that the maximum variability of both the observed and simulated patterns is between 20°N and 40°N. The simulated pattern does not show the secondary maxima near the equator and 70°N. In the Southern Hemisphere the simulated values give a small maximum between 30°S and 50°S.

3.1.4 Free Air Temperature

The zonal average of temperatures at 500 mb is shown in Fig. 3.10. The January simulated field is colder than the observed. In addition the temperature difference between the equator and 75°N exceeds the observed difference by about 10°C. Both patterns are relatively flat between 10°S and 40°N. However, north of 40°N the simulated temperature gradient is steeper than revealed by the observations. In the Southern Hemisphere we cannot rely on the observed (December - February) averages since January may differ from the three-month average. In general, the simulated temperature is warmer than the observed between 35°S and 75°S.

The geographic maps of the simulated January temperatures for the 750 mb and 500 mb levels (Fig. 3.11a,b) reveal a reasonable simulation of these fields. In particular, note the configuration of the thermal ridge to the west of the North America Continent and Eurasia, and also the thermal troughs along the east coasts of these continents. In the Southern Hemisphere the warm centers over South America and Australia are correctly simulated.

Statistically speaking, the variance of temperature is a measure of the deviation of the individual temperature distributions from the zonal

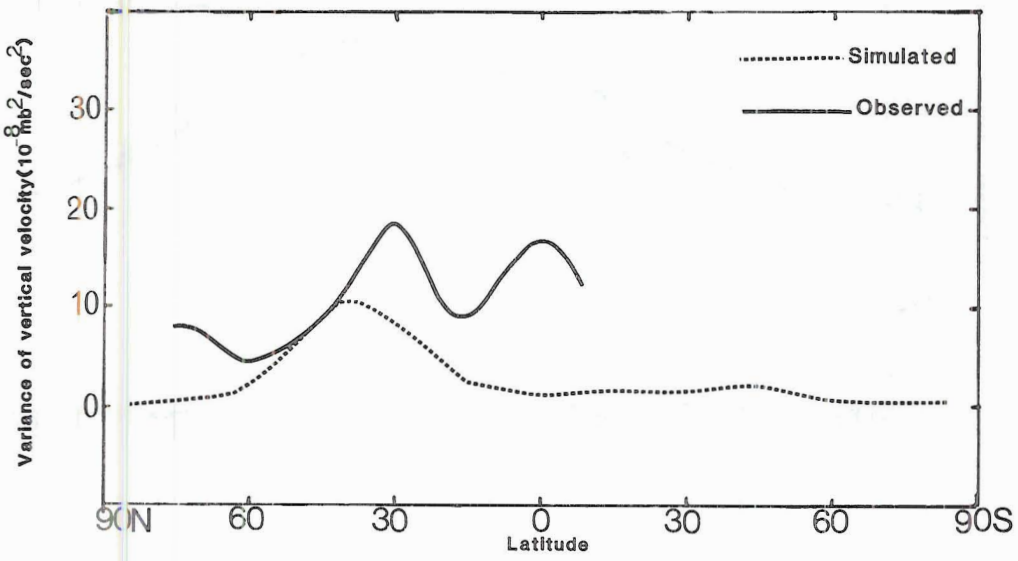

3.9 The tropospheric average of the observed (full line) and simulated (dotted line) zonally averaged variances of vertical pressure velocity (10^{-8} mb^{2}sec^{-2}) resulting from stationary eddies for January.

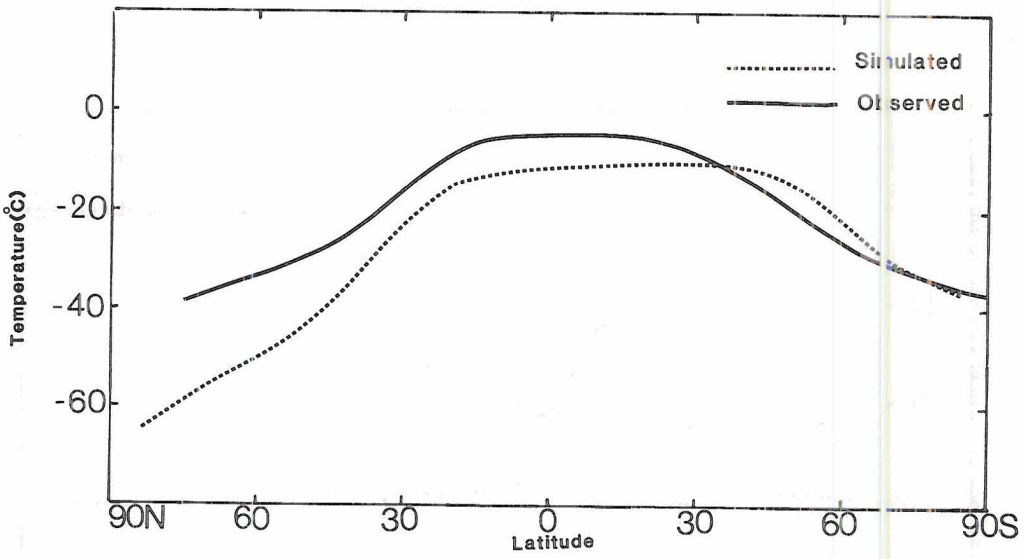

3.10 The zonal average of the observed (full line) and simulated (dotted line) temperature (°C) at 500 mb for January.

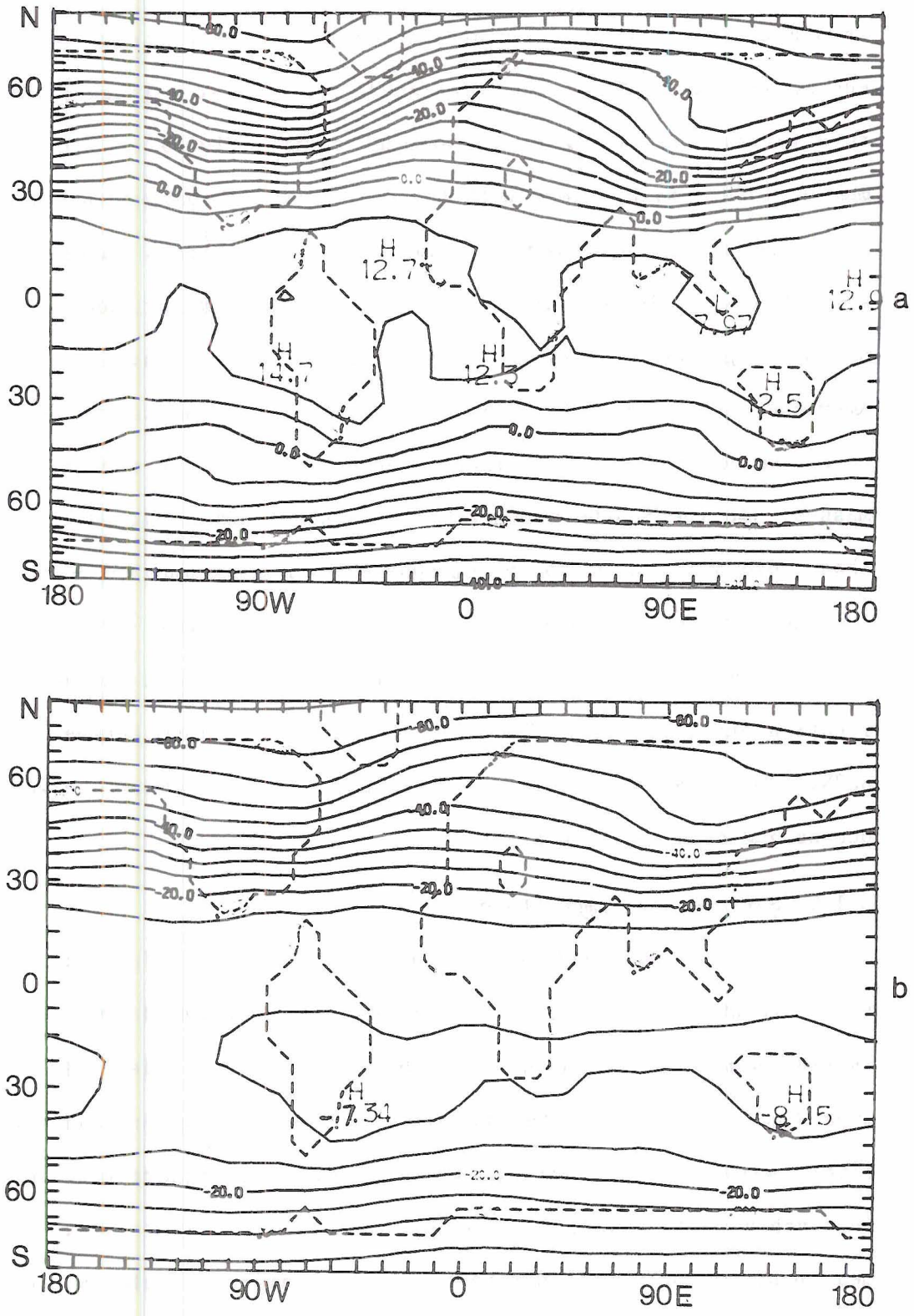

3.11 The simulated temperature (°C) for January.
a) At 750 mb; b) At 500 mb.

mean value. From a physical point of view, the variance of temperature is a measure of the local contribution to the eddy available potential energy (Lorenz, 1955). The simulated tropospheric average of temperature variance resulting from transient eddies (Fig. 3.12) shows a maximum at 65°N, which agrees with the corresponding observed pattern. The amplitude of the observed maximum is about two times larger than the simulated one. The maximum variance occurs at this latitude as a result of the high variability of temperature over the Eurasian and North American continents. Over these continents large variation in temperature can occur due to alternative advection of polar and tropical air masses. In the Southern Hemisphere the simulated variances are smaller than those over the Northern Hemisphere, with a maximum value near 50°S. The variance of the simulated temperatures resulting from stationary eddies (Fig. 3.13) shows a good agreement with observations for both the location and amplitude. Both reveal a winter maximum between 50°N and 60°N. This maximum occurs as a result of the contrast between warm oceans and cold continents.

3.1.5 Surface Air Temperature

The simulated (1000 mb) and observed January surface air temperatures are shown in Fig. 14a,b. The large scale temperature distribution is well simulated by the model. The reservoirs of relatively cold air over the continents in the Northern (winter) Hemisphere and the relatively warmer air over the Southern (summer) Hemisphere continents are reasonably well projected. The 0°C isotherm is nearly in its observed mean position over the continents in the simulated field, whereas over the oceans it is shifted southward from its observed position. This indicates that the simulated amplitude is less than the observed, as a

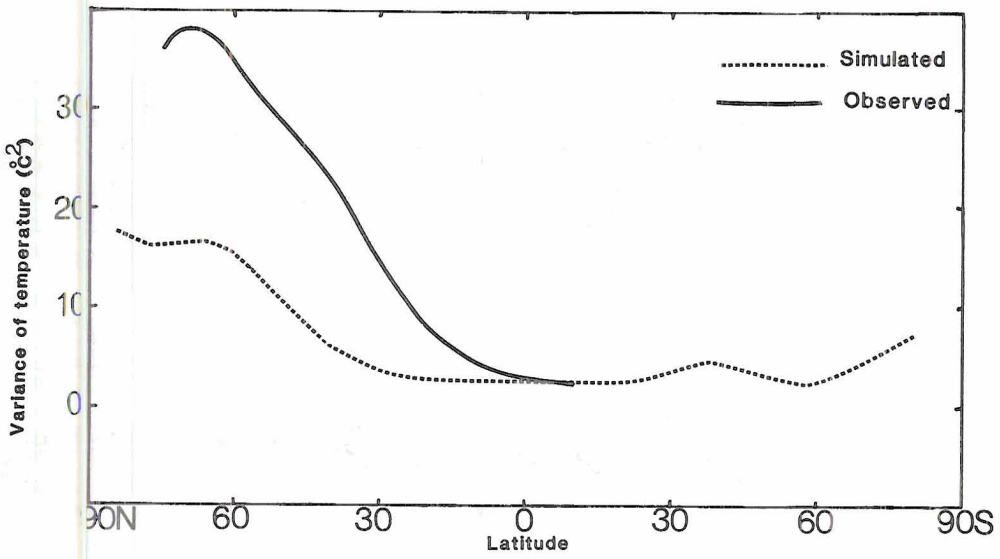

3.12 The tropospheric average of the observed (full line) and simulated (dotted line) zonally averaged variance of temperature ($°C^2$) resulting from transient eddies for January.

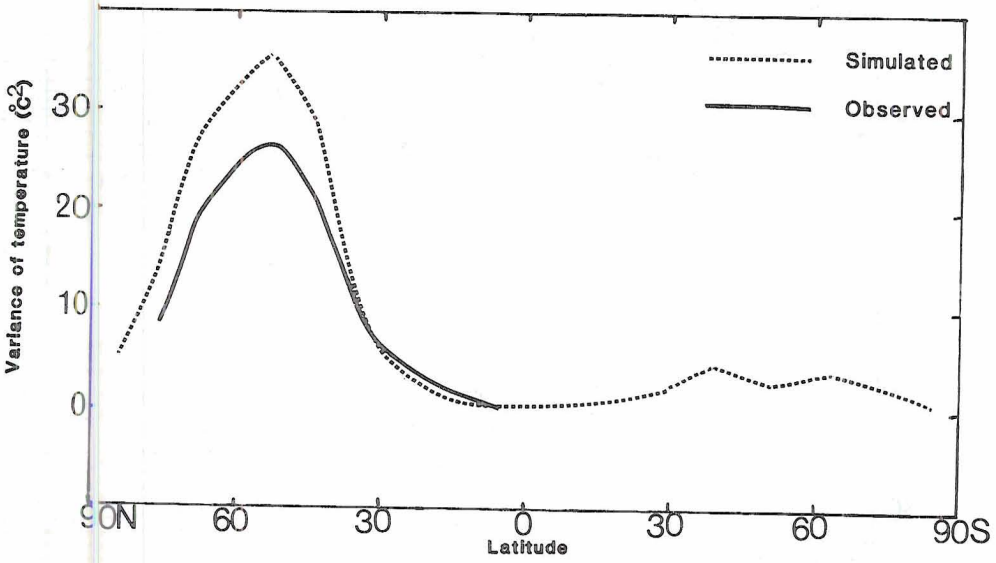

3.13 The tropospheric average of the observed (full line) and simulated (dotted line) zonally averaged variance of temperature ($°C^2$) resulting from stationary eddies for January.

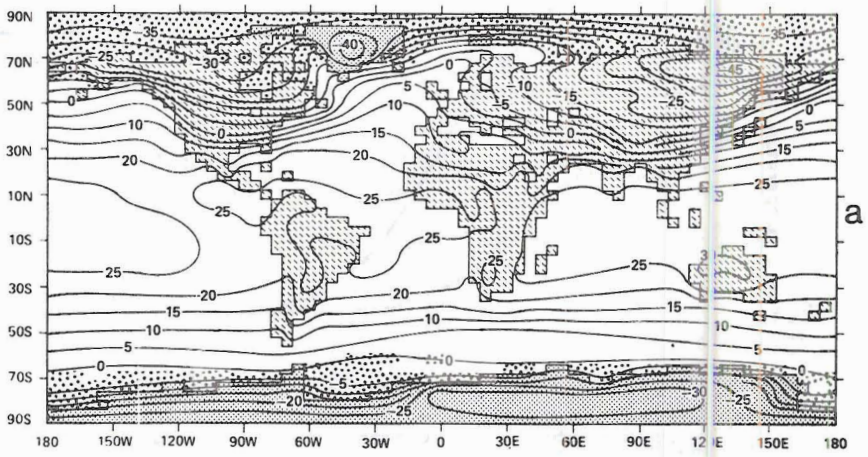

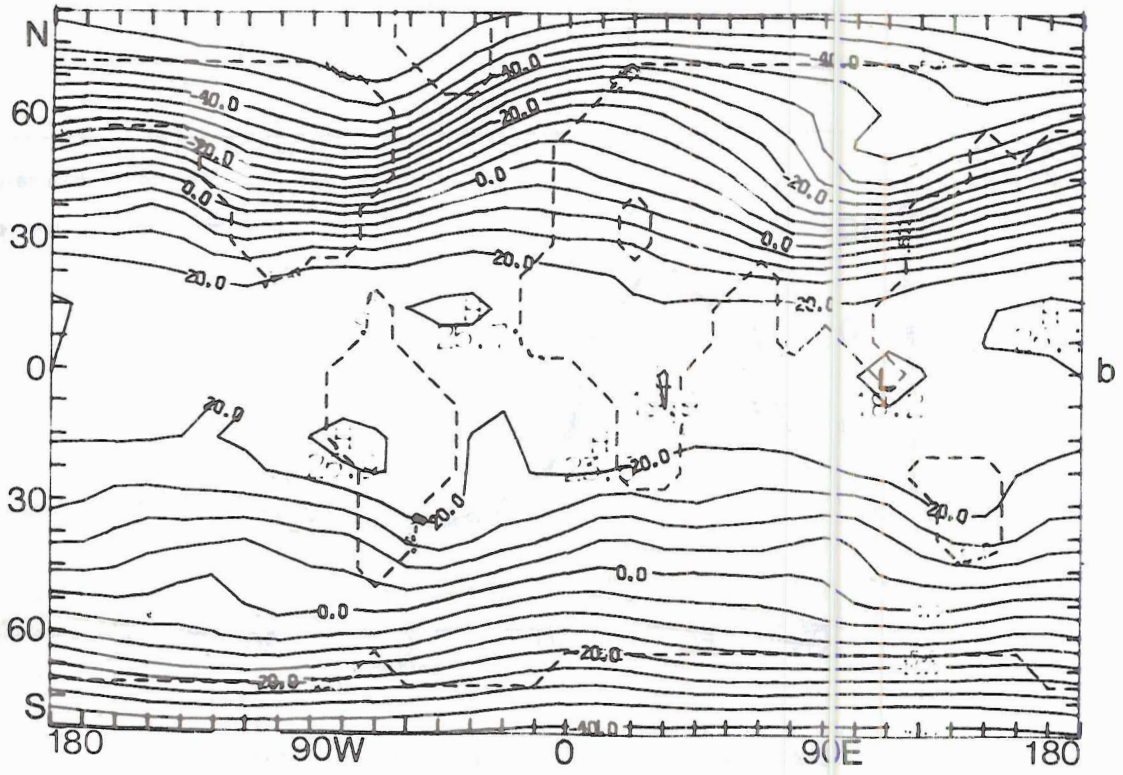

3.14 The surface air temperatures (°C) for January.
a) observed; b) simulated (1000 mb).

result of the zonal average radiative forcing used in the model. The cold pools over the eastern United States and Eurasia and the cold air mass associated with the Siberian high also are reasonably well simulated. In the Southern Hemisphere, the temperatures are somewhat colder than those revealed by observations.

3.1.6 Geopotential Height

The zonal average 500 mb geopotential height departures from the global average (Fig. 3.15) show the model's tendency to predict lower pressure in the Northern Hemisphere and higher pressure in the Southern Hemisphere. The larger simulated pressure gradient in the Northern Hemisphere also is shown. The simulated January 750 mb and 500 mb geopotentials are compared with the observed 800 mb and 400 mb geopotential (Fig. 3.16a,b; Fig. 3.17a,b). We can summarize the comparison as follows:

1) The ridges on the western sides of North America and Eurasia are correctly simulated for both the 750 mb and 500 mb fields.

2) The ridge north of the Himalayas is simulated in the 750 mb map, as is the trough to the south, but the model calculates a higher geopotential gradient in the southern part, which leads to an over-estimate of the strength of the southwesterly flow there.

3) The Aleutian low covers the central and eastern Pacific in the 750 mb simulation. On the 500 mb map, the trough over the Pacific has a reasonable phase, but a smaller amplitude than that observed at 400 mb.

4) In the Southern Hemisphere the simulated 750 mb geopotential height shows the subtropical high pressure region over the eastern Pacific and western Atlantic. The observed low pressure area

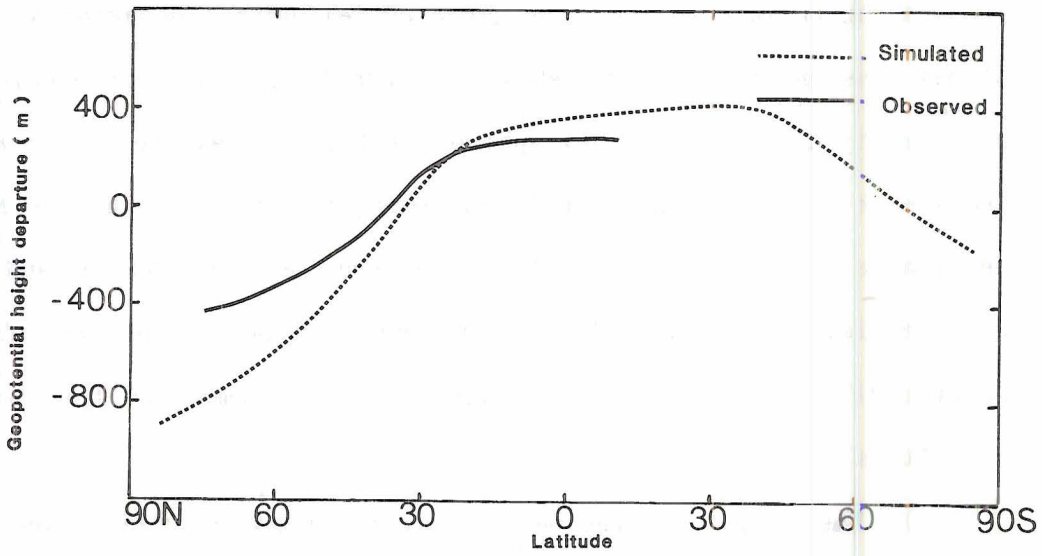

3.15 The zonal average of the observed (full line) and simulated (dotted line) geopotential height departures (m) at 500 mb for January.

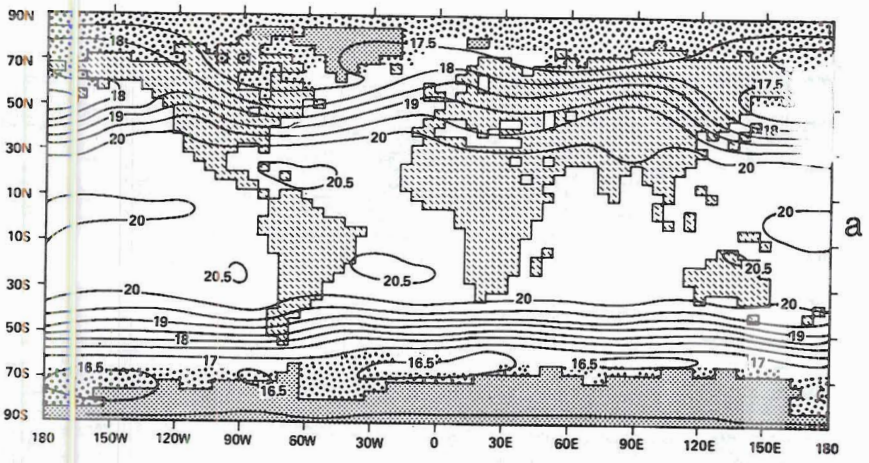

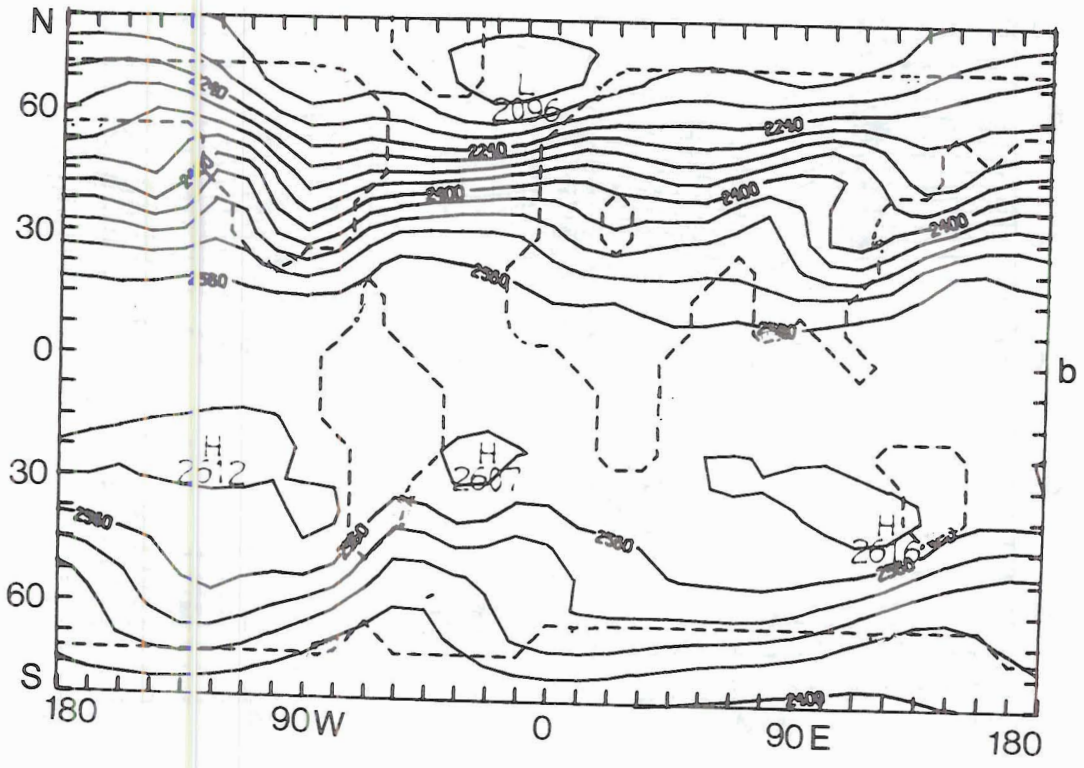

3.16 The geopotential height for January. a) observed (10^2m) at 800 mb; b) simulated (m) at 750 mb.

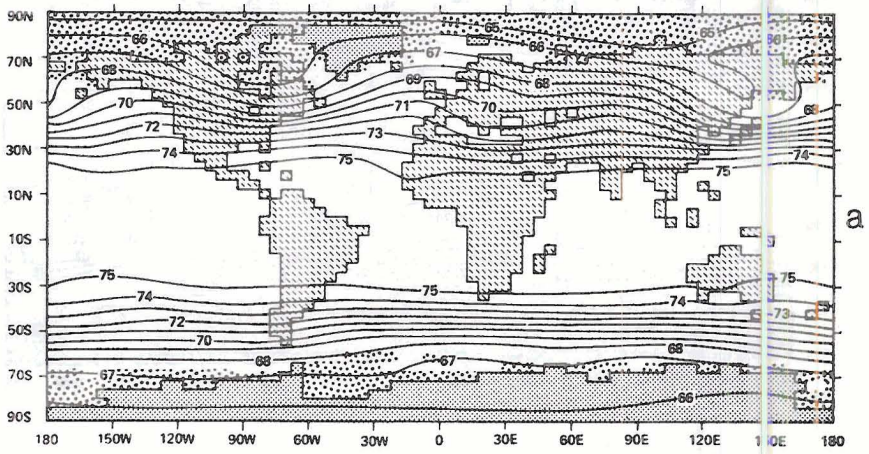

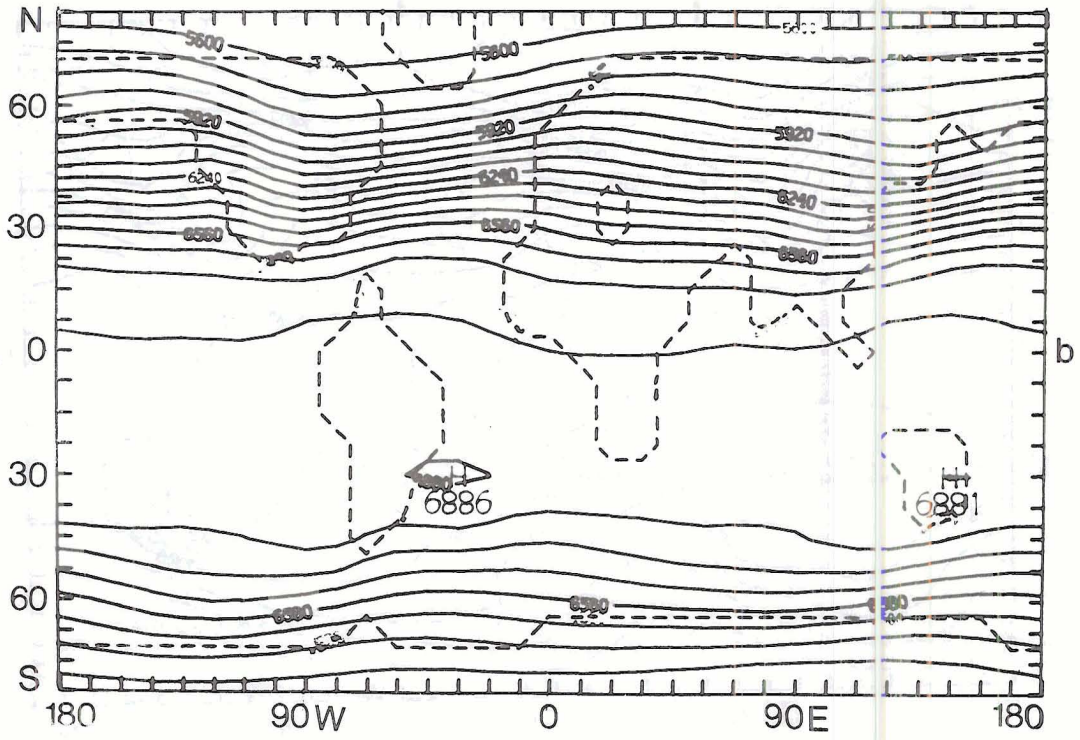

3.1/ The geopotential height for January. a) observed (10^2m) at 400 mb; b) simulated (m) at 500 mb.

between 10°N and 10°S in the Pacific is reasonably simulated. The simulated 500 mb geopotential shows a reasonable agreement with the observed 400 mb field. The latitude of the simulated maximum geopotential gradient is at about 50°S, in agreement with the observations.

In the Northern Hemisphere the location of the variance of the simulated geopotential heights resulting from transient eddies agrees with the observations, but with a smaller magnitude (Fig. 3.18). The observed maximum, between latitudes 50°N and 75°N, is about three times larger than the simulated maximum. The same conclusion is true for the variance resulting from stationary eddies (Fig. 3.19), but the simulated amplitudes are about half the observed values.

3.1.7 Sea level pressure

Although the sea level pressure may be not the most important factor from the point of view of climate studies, its representation completes a summary of the general circulation. The model does not predict the surface pressure. A constant lower boundary of 1000 mb is assumed. However, we can still have an estimation of the sea surface pressure of the model using a diagnostic relation that takes into consideration the average geopotential, temperature and the static stability of the model's atmosphere. This relation is derived, using the hydrostatic relation, and assuming an atmosphere with constant lapse rate,

$$p_s = \Delta p \left(1 + \Gamma \frac{Z_2}{T_2}\right)^{g/R\Gamma} , \qquad (3.7)$$

where Γ is the temperature lapse rate, p_s is an analogue to the surface pressure (mb), Δp = 500 mb, Z_2 is the 500 mb geopotential height, and T_2 the 500 mb temperature (°K).

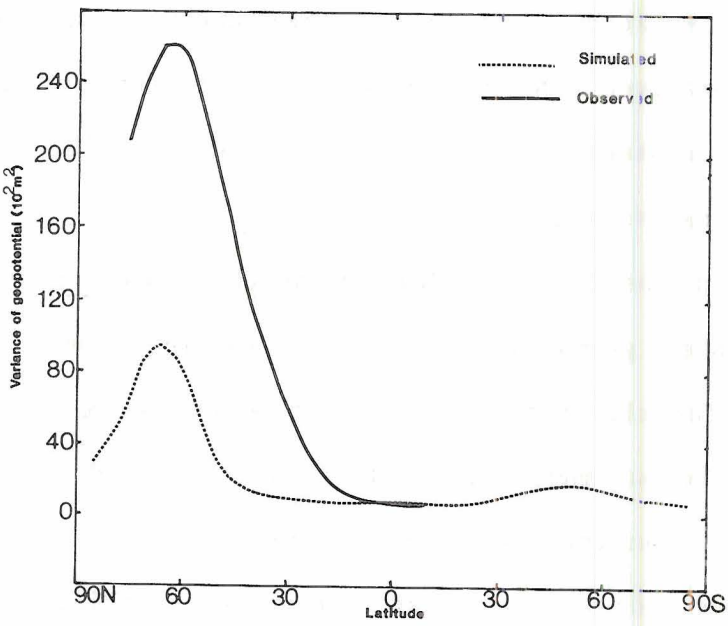

3.18 The tropospheric average of the observed (full line) and simulated (dotted line) zonally averaged variance of geopotential height (m^2) resulting from transient eddies for January.

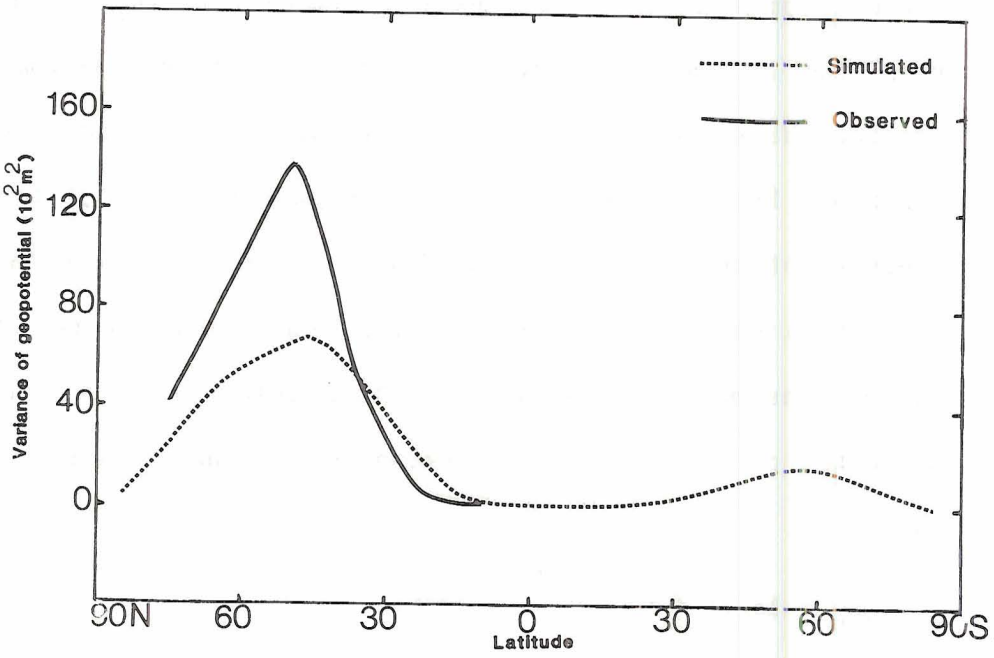

3.19 The tropospheric average of the observed (full line) and simulated (dotted line) zonally averaged variance of geopotential height (m^2) resulting from stationary eddies for January.

Fig. 3.20 represents the January simulated sea level pressure deviations from a global average. In general we can see the tendency for the model to simulate a mean sea level pressure which is low in the winter and high in summer. This tendency was mentioned by Gates and Schlesinger (1977), who used a two-level primitive equation model with a sigma coordinate system. In the Northern Hemisphere the model correctly locates the Siberian high, the ridge over the western United States, and the Aleutian and Atlantic lows. Neither the Aleutian nor Atlantic lows spread over the entire ocean areas, but they do cover the central and eastern parts. In the Southern Hemisphere high pressure ridges appear over the subtropical South Pacific, the South Atlantic and the Indian Oceans. The relatively low pressure over the continents of South America and Australia also are simulated, while over South Africa the observed trough is shifted to the west.

3.1.8 Mixing Ratio

The moisture budget is calculated in the lower layer of the model only (750 mb level). Since the mixing ratio and the specific humidity are nearly the same and have the same properties, the simulated 750 mb mixing ratio for January is compared with observed specific humidities at 700 mb and 850 mb. The zonally averaged simulated mixing ratio (Fig. 3.21) shows the same tendency as the observed field at all latitudes, but is underestimated in the extratropical latitudes, where colder temperatures are simulated.

The average tropospheric variance of the simulated and observed mixing ratio resulting from both the transient and stationary eddies are shown in Figs. 3.22 and 3.23, respectively. The simulated transient

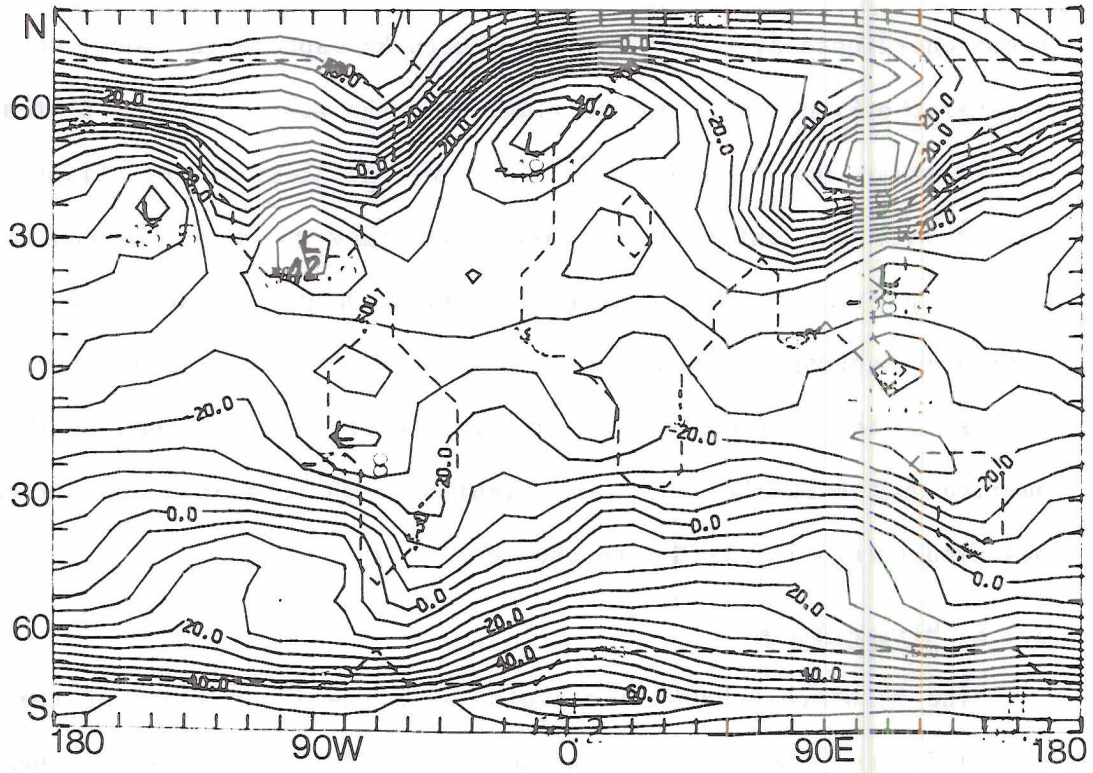

3.20 The simulated departures in the mean sea level pressure (mb) for January.

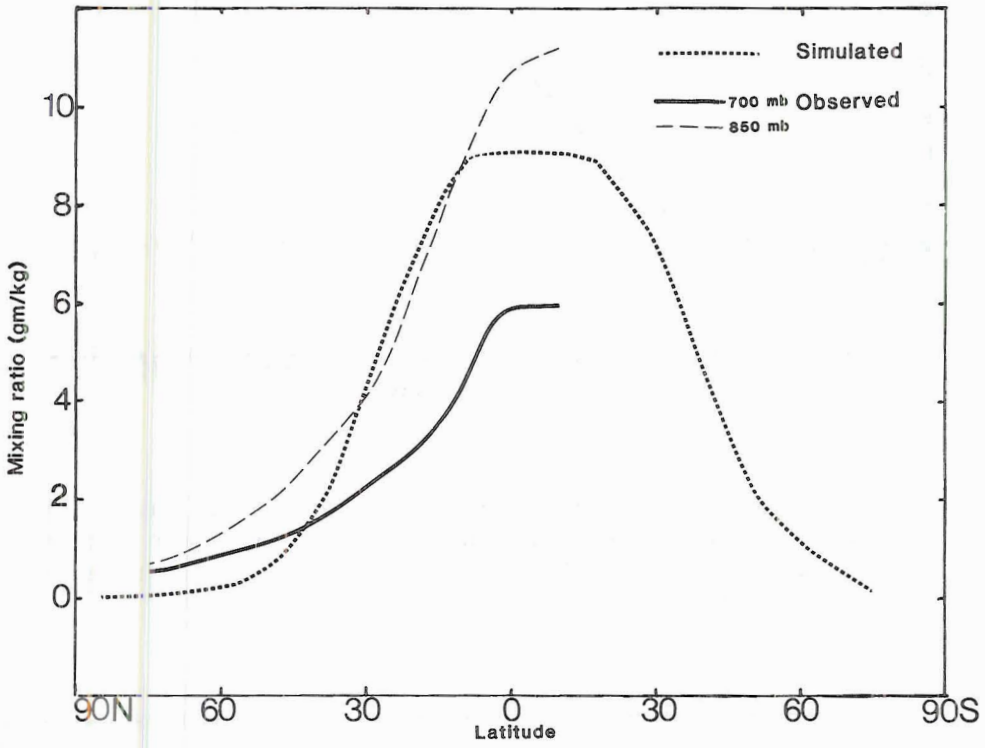

3.21 The zonal average of the observed (700 mb, full line; 850 mb, dashed line) and simulated (dotted line)mixing ratio (gm/kg) for January.

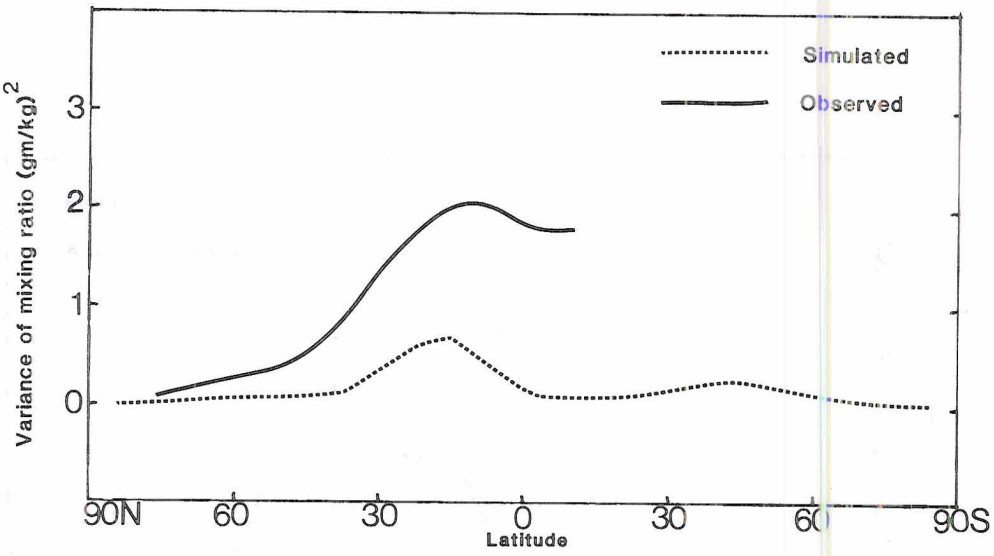

3.22 The tropospheric average of the observed (full line) and simulated (dotted line) zonally averaged variance of mixing ratio $(gm/kg)^2$ resulting from transient eddies for January.

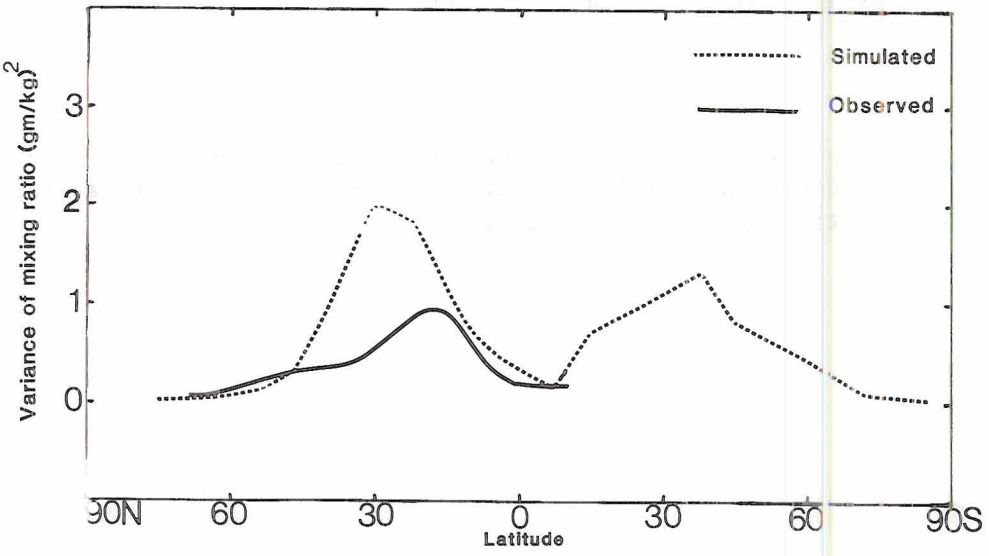

3.23 The tropospheric average of the observed (full line) and simulated (dotted line) zonally averaged variance of mixing ratio $(gm/kg)^2$ resulting from stationary eddies for January.

component has its maximum at 15°N, about 5° north of the observed maximum. Also, in the Southern Hemisphere, a secondary maximum is simulated at 40°S. The simulated stationary component has its maximum at 30°N, whereas the observed maximum is at 20°N. Both the simulated and observed fields reveal an area of maximum variability between 10°N and 40°N. There is a secondary maximum in the Southern Hemisphere near 40°S.

3.1.9 Precipitation and Evaporation

Precipitation occurs in the model as a result of condensation due to large scale supersaturation. All condensed water is assumed to fall instantaneously to the surface as rain, without being re-evaporated or stored in the lower layer. Convection develops if the resulting lapse rate is larger than the moist adiabatic lapse rate, after the release of latent heat in the lower layer.

The model's simulation of precipitation seems to be more successful in the Northern Hemisphere than in the Southern Hemisphere (Fig. 3.24). In both hemispheres, more precipitation is simulated over the oceans than over the continents. According to observations, this is only true in the winter hemisphere (see for example Gates and Schlesinger, 1977). The zonal average of the simulated precipitation (Fig. 3.26) shows maxima on the equator, and at 30°N, 30°S, 70°N and 80°S. The excessive rain in the Southern Hemispheric polar latitudes is considered to be in error.

The evaporation from the surface to the model's lower layer is better simulated than the precipitation field (Fig. 3.25). In both hemispheres the maximum evaporation is over the oceans, in agreement with observations (Gates and Schlesinger, 1977). The areas of maximum

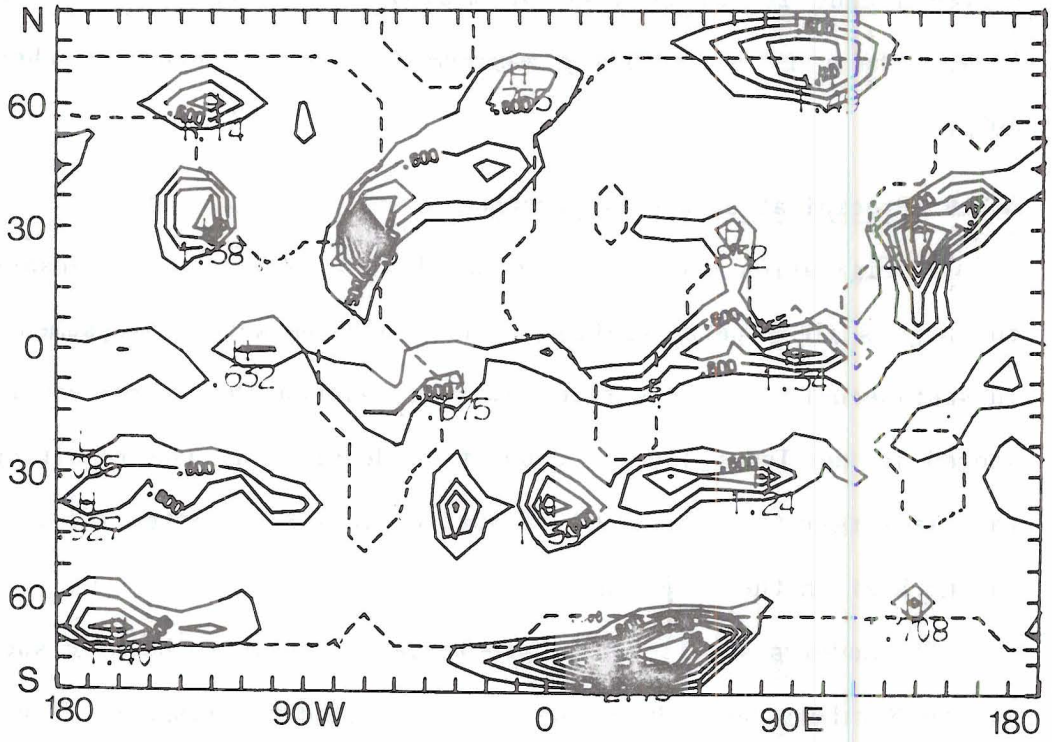

3.24 The simulated precipitation rate (cm/day) for January.

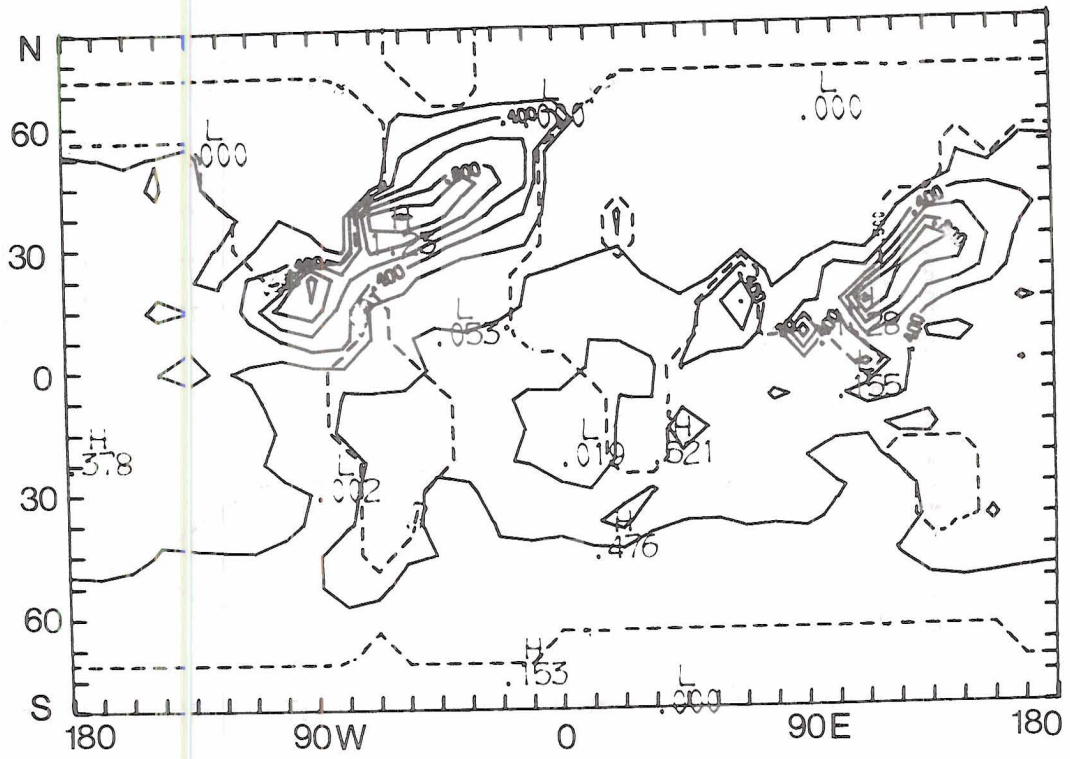

3.25 The simulated evaporation rate (cm/day) for January.

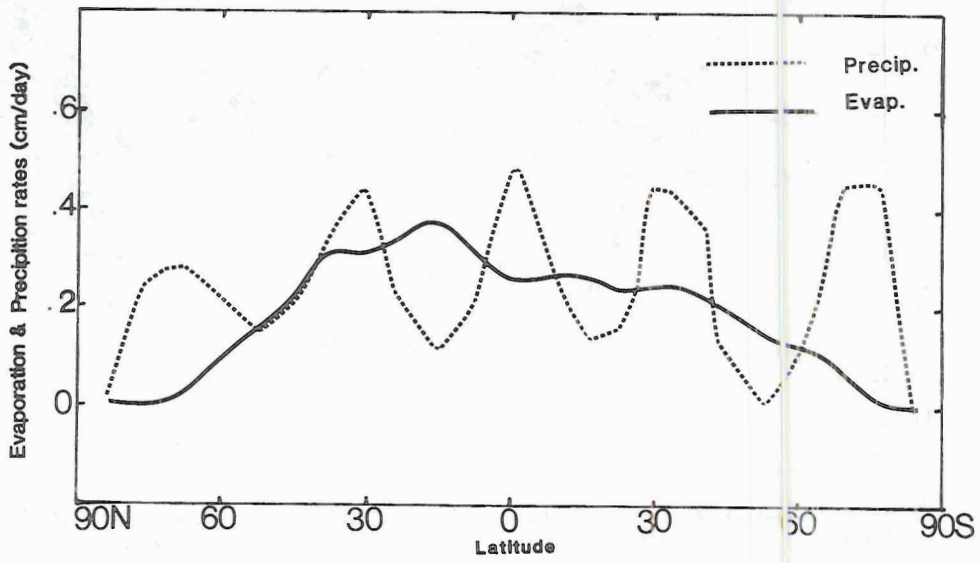

3.26 The zonal average of the simulated evaporation rate (full line) and precipitation rate (dotted line) for January.

evaporation over the western Pacific, western Atlantic, Indian Ocean and South Pacific are reasonably well simulated. One of the reasons that the simulated evaporation has a better match with observations than precipitation is that the model uses a similar bulk formula as in calculating the evaporation from observed data. In parameterizing precipitation, many important mechanisms were excluded, in addition to assuming that the moisture was in one layer only.

The difference between evaporation and precipitation represents the net moisture source or sink to the model's atmosphere. The zonally averaged simulated sources (evaporation larger than precipitation) of moisture are in the subtropical latitudes of both hemispheres between 5°N and 28°N, and between 10°S and 25°S. Another source appears in the Southern Hemisphere between 45°S and 60°S. This source represents the effect of large amounts of evaporation from the ocean during summer. The sinks appear mainly in the equatorial belt between 10°S and 5°N, 55°N and the North Pole, and 25°S and 45°S. The large negative values near the South Pole, which result from the spurious amount of rain simulated by the model at this latitude, do not affect the results significantly due the small area of the polar cap as compared to other latitude belts.

3.2 Meridional Transports

For the atmosphere-ocean system, the zonally averaged radiation pattern shows an excess of incoming over outgoing radiation in low latitudes and a deficit in high latitudes. The radiational imbalance is maintained by strong poleward transports of energy in the atmosphere and oceans. The major components of energy transported are sensible heat,

potential energy, latent heat and kinetic energy. In a certain latitudinal band, the time averages of these energy components usually balance. The convergence and divergence of the north-south flow component play an important role in creating such a balance. We can define two mechanisms of transfer; namely, the transfer by the eddies (transient or stationary) and the transfer by the mean meridional circulation.

Using the same definitions as in section 3.1, we define the following transport processes for a certain parameter X:

northward transport by transient eddies = $[\overline{v'X'}]$

northward transport by stationary eddies = $[\bar{v}^*\bar{X}^*]$

northward transport by mean meridional circulation = $[\bar{v}]''[\bar{X}]$,

where v is the meridional wind component and the superscript " denotes the deviation from the vertical average.

The simulated transports for January of westerly momentum, sensible heat, potential energy and latent heat are discussed and compared with the observed values. Kinetic energy transports will not be presented here. In general their influence is much less than that due to sensible heat, latent heat and potential energy (Starr, 1951).

3.2.1 Transport of Westerly Momentum

Both the observed and simulated meridional transports of westerly momentum by the transient eddies (Fig. 3.27) show a maximum near 35°N to 45°N. This maximum is a result of the strong westerly subtropical jet stream. As in the case of the variances, the simulated amplitude is considerably smaller than the observed one. The transport of westerly momentum by stationary eddies (Fig. 3.28) shows a better agreement with

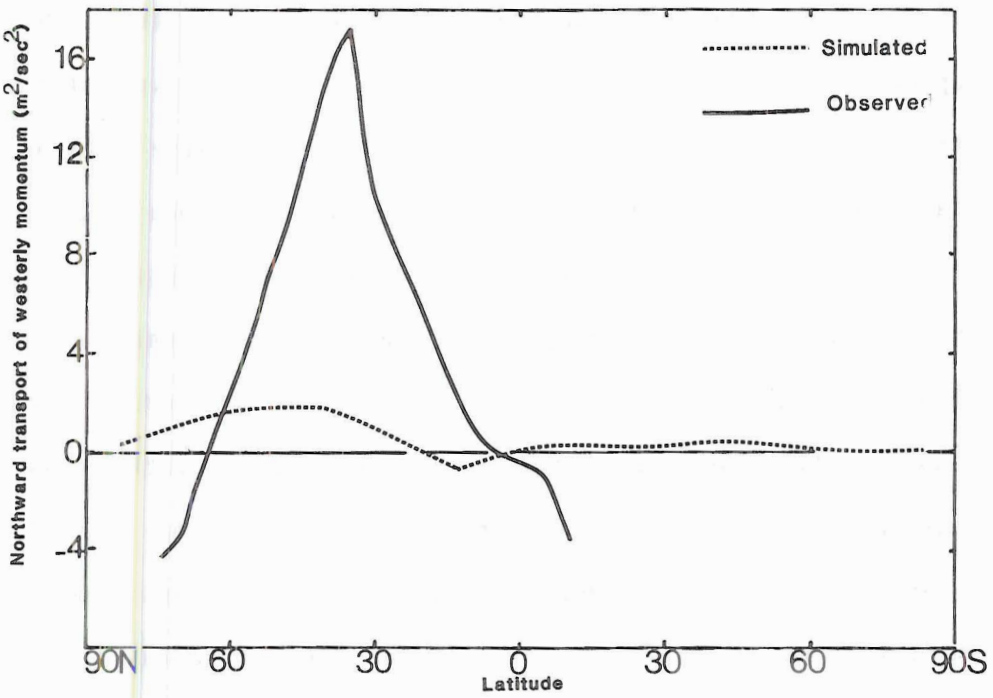

3.27 The tropospheric average of the observed (full line) and simulated (dotted line) zonally averaged northward transport of westerly momentum ($m^2 sec^{-2}$) by the transient eddies for January.

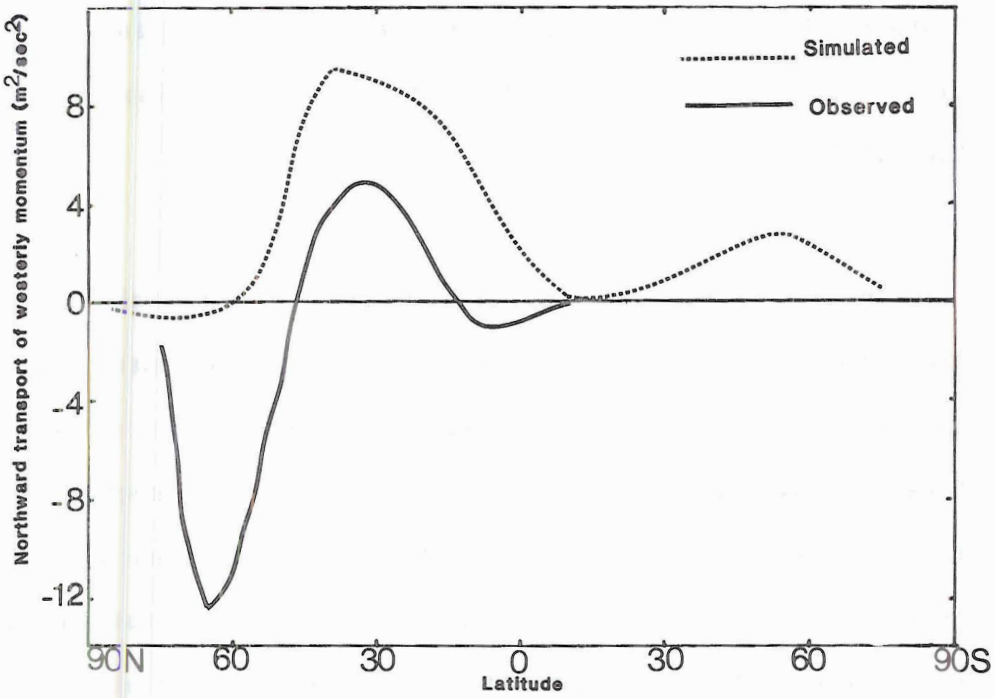

3.28 The tropospheric average of the observed (full line) and simulated (dotted line) zonally averaged northward transport of westerly momentum ($m^2 sec^{-2}$) by the stationary eddies for January.

the observed pattern than the transient case. The maximum transport appears to be between 30°N and 40°N. The observed strong southward transport in the extratropical Northern Hemisphere latitudes is simulated as a small southward transport near the polar region. The model fails to simulate the small southward momentum transport in the Northern Hemisphere tropical region. In the Southern Hemisphere there is a simulated maximum near 50°S. The observed transport of westerly momentum by the mean meridional circulation (Fig. 3.29) shows four main latitudinal zones with alternating signs. These are the southward transports in the Southern Hemisphere tropical region and in the subtropical to midlatitude region, and the northward transport in low latitudes and the polar region. These four cells of transport are simulated by the model, but in the area north of 30°N the model did not correctly simulate the location of the observed pattern. In the Southern Hemisphere the small observed southward transport in the tropical region is extended to reach the Southern Hemisphere subtropics in the simulated case.

3.2.2 Transport of Sensible Heat

In discussing this type of transport we must take into consideration that the sensible heat by itself is not a conservative quantity. Latent heat, potential energy and kinetic energy are needed to attain a total energy conservation. The latitudinal cross section of the simulated transports at 750 mb and 250 mb are compared with the observed cross sections at 700 mb, 500 mb and 300 mb. Observations show a maximum transport by transient eddies (Fig. 3.30a) between 40°N to 60°N at all levels. The simulated pattern shows the maximum in the same latitudinal belt Fig. (3.31a), but with a slightly smaller magnitude. At

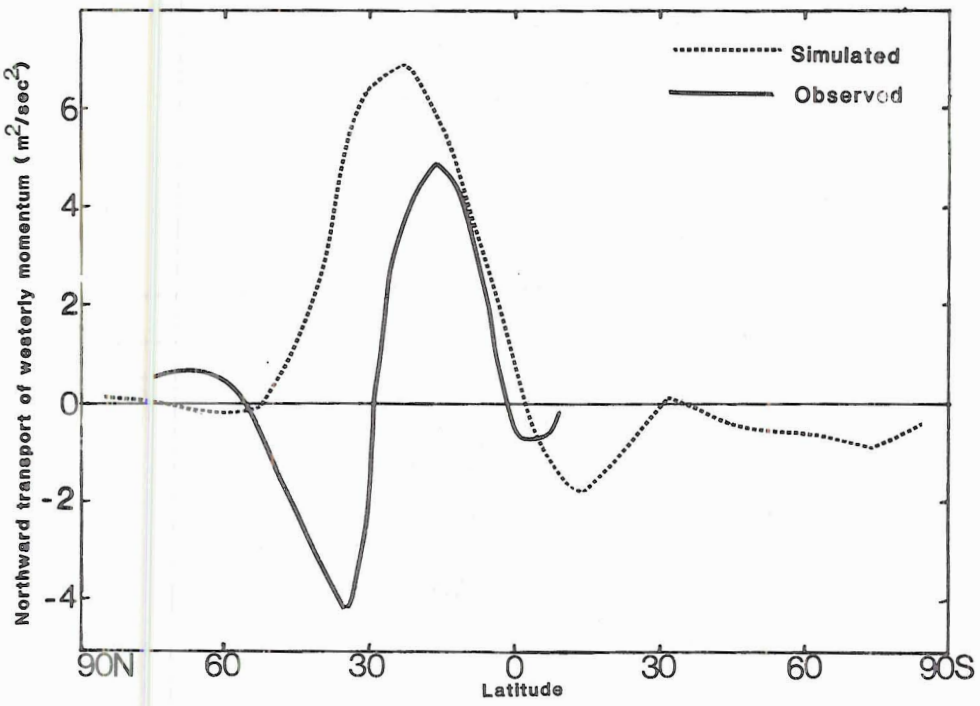

3.29 The tropospheric average of the observed (full line) and simulated (dotted line) zonally averaged northward transport of westerly momentum ($m^2 sec^{-2}$) by the mean meridional circulation for January.

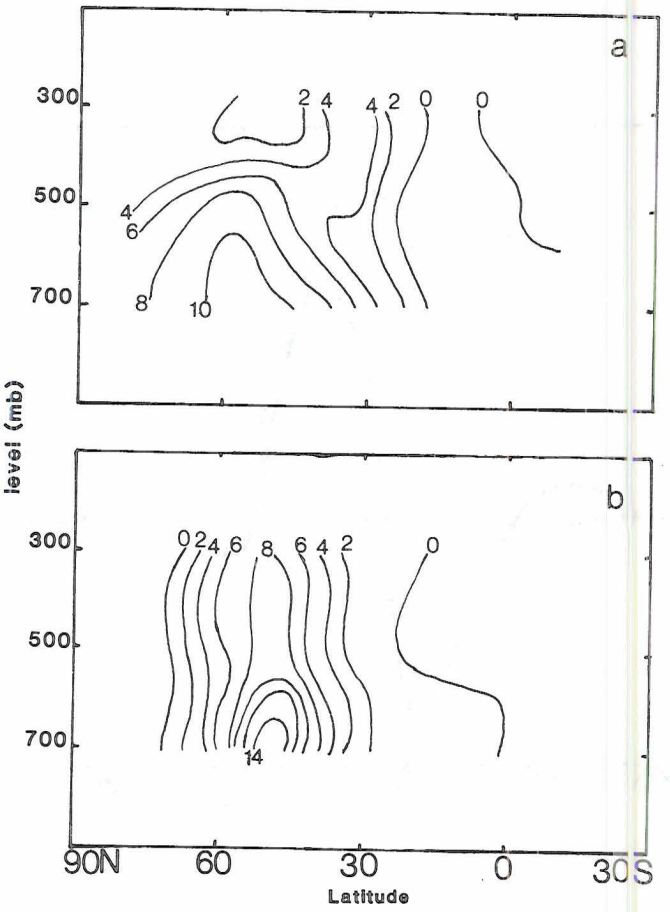

3.30 Vertical cross section of the observed zonally averaged northward transport of temperature (m sec $^{-1}$ °C) for January. a) by the transient eddies; b) by the stationary eddies.

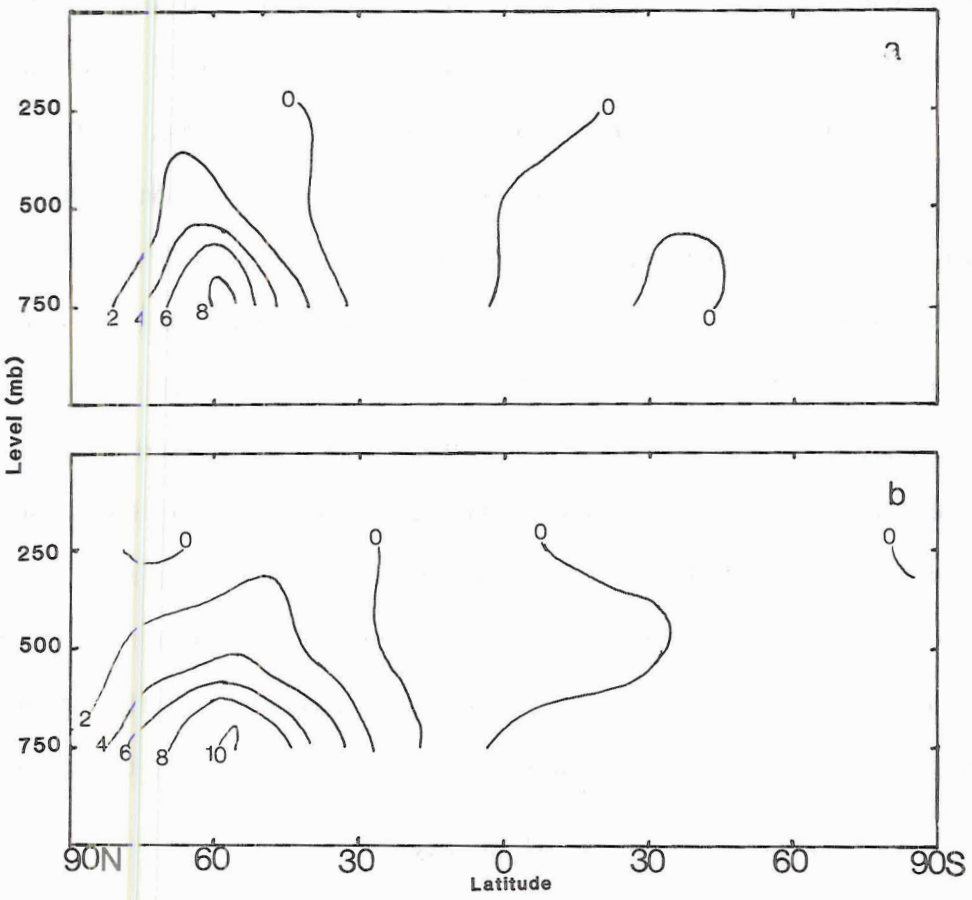

3.31 Vertical cross section of the simulated zonally averaged northward transport of temperature (m sec^{-1} °C) for January. a) by the transient eddies; b) by the stationary eddies.

250 mb the simulated values show a small southward transport at most of the subtropical latitudes of the Northern Hemisphere. The simulated transport of sensible heat by standing eddies (Fig. 3.31b) has a reasonable agreement with the observed cross section (Fig. 3.30b), especially in the middle and extratropical latitudes of the Northern Hemisphere. In the Southern Hemispheric midlatitudes a simulated northward sensible heat transport appears at all levels. The transport by the mean meridional circulation (Fig. 3.32) shows nearly the same differences as the transport of the westerly momentum. The simulated transport in the tropical region is extended to the subtropics in the Southern Hemisphere and to the midlatitudes in the Northern Hemisphere. In the extratropical latitudes of the Northern Hemisphere, the two patterns are not similar. One should emphasize the small values of this type of transport as compared to the correctly simulated transport by the eddies.

3.2.3 Transport of Potential Energy

The observed transport by transient eddies (Fig. 3.33a) shows a maximum southward transport in the middle and upper troposphere of the Northern Hemisphere between 30°N and 50°N. Also there is a secondary maximum of northward transport between 60°N and 80°N. These features are well duplicated by the model (Fig. 3.34a). At the lower level (750 mb), the observed northward transport is stronger than the simulated transport. In the Southern Hemisphere the model simulates a southward transport in the lower layer and northward transport in the upper layer. The transports by stationary eddies show a similar agreement between observed and simulated cross sections (Figs. 3.33b, 3.34b), particularly in the Northern Hemisphere subtropical and middle latitudes. In high

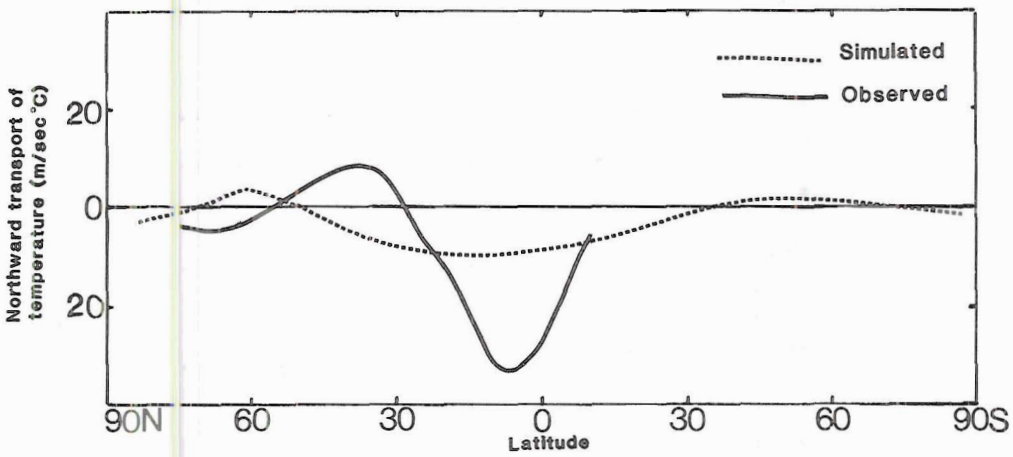

3.32 The tropospheric average of the observed (full line) and simulated (dotted line) zonally averaged northward transport of temperature (m sec^{-1} °C) by the mean meridional circulation for January.

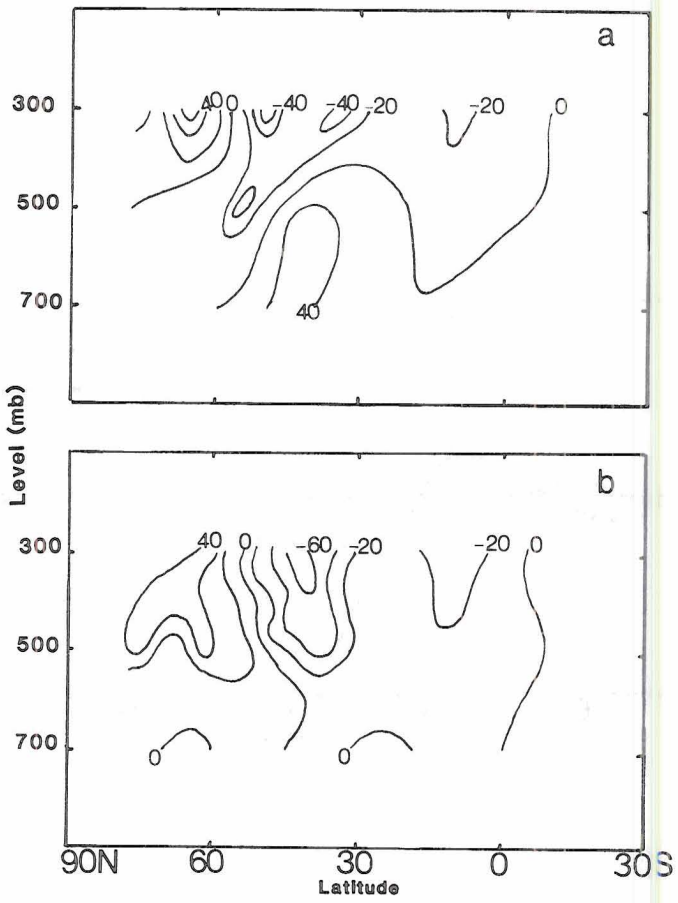

3.33 Vertical cross section of the observed zonally averaged northward transport of geopotential height ($m^2 sec^{-1}$) for January. a) by the transient eddies; b) by the stationary eddies.

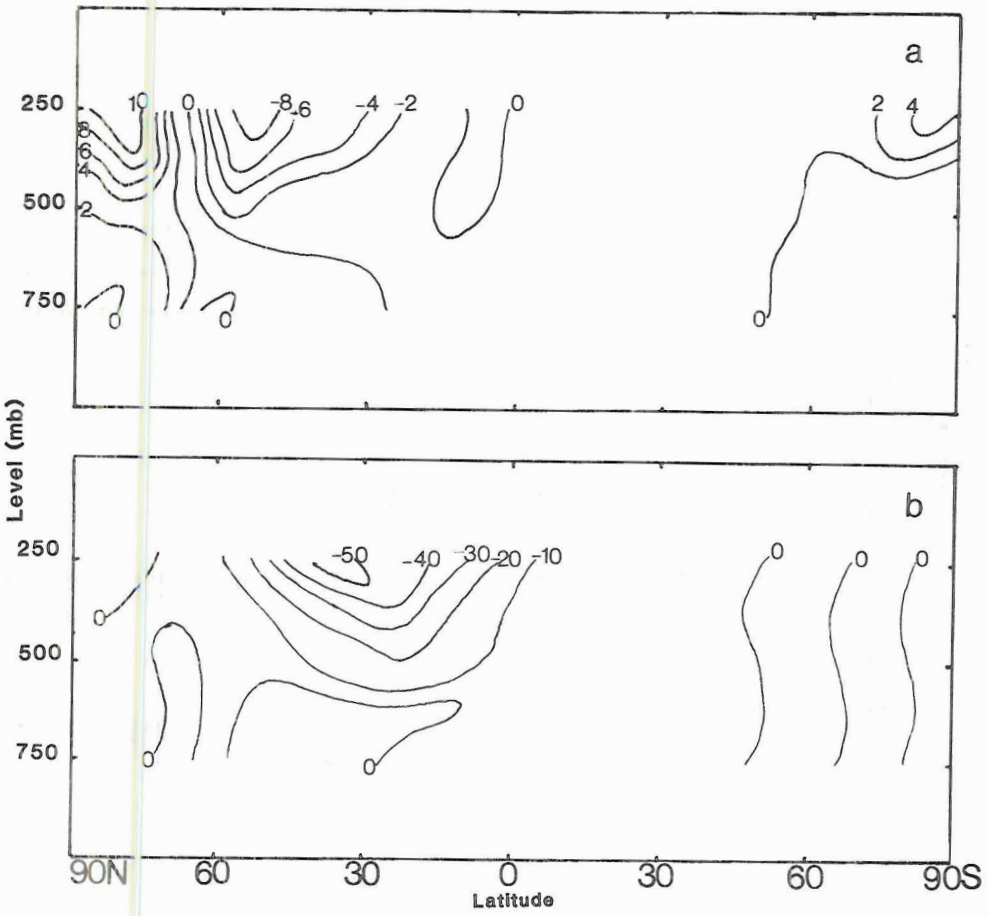

3.34 Vertical cross section of the simulated zonally averaged northward transport of geopotential height ($m^2 sec^{-1}$) for January. a) by the transient eddies; b) by the stationary eddies.

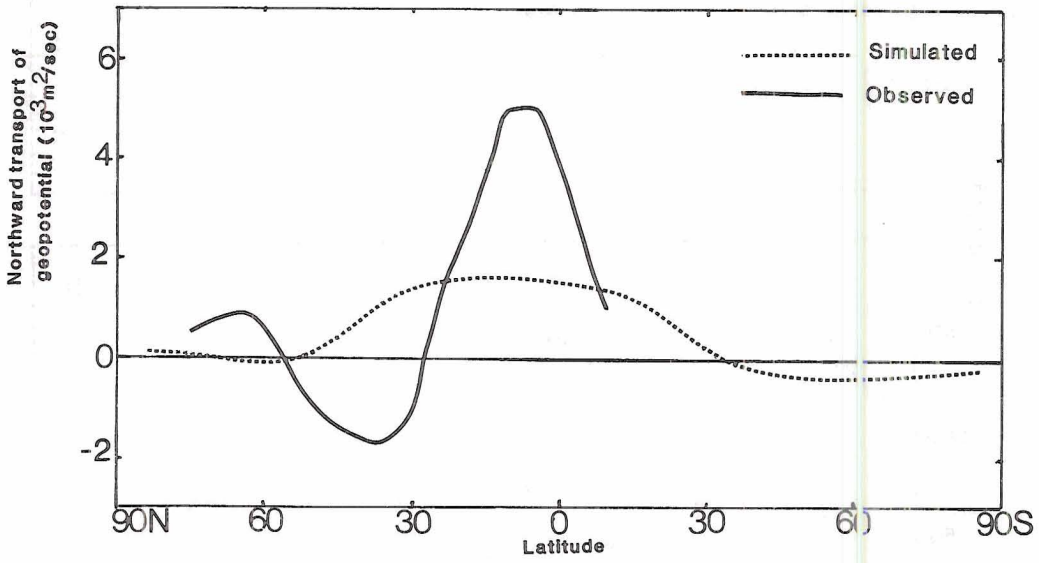

3.35 The tropospheric average of the observed (full line) and simulted (dotted line) zonally averaged northward transport of geopotential height ($m^2 sec^{-1}$) by the mean meridional circulation for January.

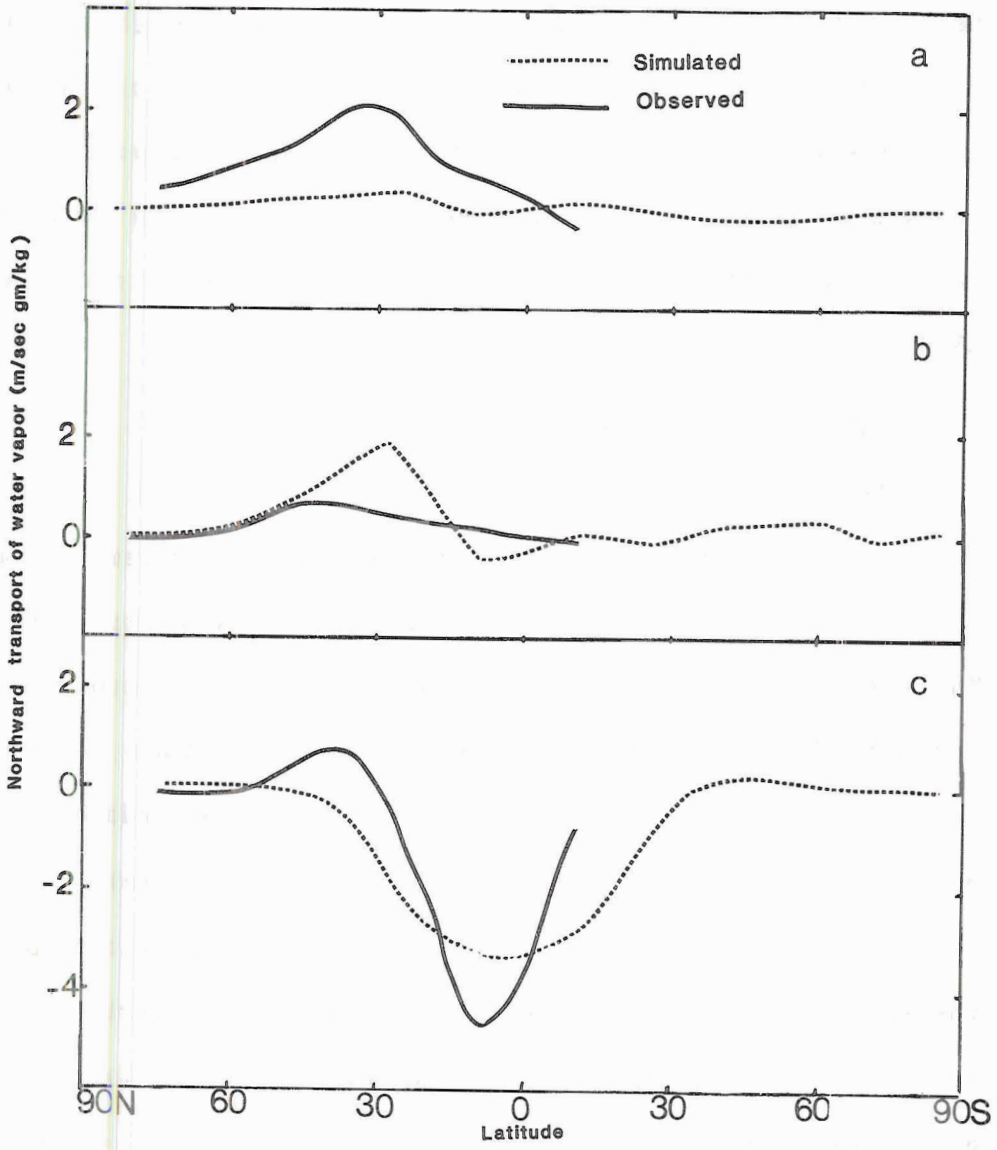

3.36 The tropospheric average of the observed (full line) and simulated (dotted line) zonally averaged northward transport of water vapor (m sec^{-1} gm/kg) for January. a) by the transient eddies; b) by the stationary eddies; c) by the mean meridional circulation

latitudes the observed upper-tropospheric northward transport is simulated, but with lesser magnitude. The transport by the mean meridional circulation (Fig. 3.35) is similar to the transport of the sensible heat. The northward transport of potential energy in the tropical region is extended to the middle latitudes. A small southward transport in the extratropical latitudes and northward transport in polar latitudes are simulated. In the Southern Hemisphere, the model simulates a continuous southward transport by the meridional circulation south of 35°S.

3.2.4 Transport of Latent Heat

The transport of water vapor resembles that of latent heat. Although the hydrologic cycle used in the model is extremely simple, it is able to simulate the major observed features of latent heat transport. The simulated transport by transient eddies has a maximum between 20°N and 35°N (Fig. 3.36a), but with less amplitude than the observed pattern. The observed maximum transport by stationary eddies at 50°N (Fig. 3.36b) is simulated at 30°. For both types of eddies, the model simulates a southward transport in the Northern Hemispheric tropical region, whereas the observations show this transport to be farther to the south. The simulated transport by the mean meridional circulation (Fig. 3.36c) also shows a reasonable agreement with observations, especially in the tropical and subtropical latitudes.

3.3 Summary

In spite of its simple structure, the model could simulate many of the major large scale features of the observed January circulation. We must take into consideration that the observed statistics used for verification include all the observed wave lengths. A fairer comparison

between the statistics of both sets would be made if we were to truncate the observations at the same wave number used in the model (wave no. 9).

From the above discussion it can be seen that the model has two main deficiencies - the first in the precipitation field (near the poles and in the Southern Hemisphere), and the second in the transient eddy motions. The simple hydrological cycle, with a crude precipitation scheme, is one factor in causing such deficiencies. The spectral transform method has its difficulty in simulating small quantities like the mixing ratio, particularly in the case of low order truncation. Harmonic coefficients may yield negative values in the mixing ratio near the poles. This difficulty is treated by assuming a spurious source of evaporation to increase the mixing ratio to a zero value. This false source of evaporation is balanced by an equal amount of precipitation. The small negative mixing ratios are set to zero. In general the effect of moisture on the general circulation is very small near the poles where such a procedure is necessary.

The simulated values of the variability and transport caused by the transient eddies generally were underestimated by the model. This is expected from this type of simulation because of the limited number of layers representing the atmosphere, and, also, because of the low order of truncation assumed. Other points to be considered are the effect of diffusion of various scalar parameters and the time filtering scheme used, which were necessary for computational stability. At the same time the locations of such variances or meridional transports by the transient eddies usually were in reasonable agreement with observations, especially in extratropical latitudes, where such mechanisms are important.

Similar problems were encountered using a more complicated model (Manabe et al., 1965). The poleward transport of angular momentum by the large scale eddies in Manabe's model was nearly half the amount revealed by observations. The horizontal resolution was found to be a major factor in improving these two deficiences. When the pole to equator grid intervals were increased from 20 to 40, the results were greatly improved, especially with regard to the vertical motion and precipitation. It is of interest that the dry version of Manabe's model revealed greater transient transports than the moist version of the same model. The release of latent heat of condensation decreases the temperature gradient and the vertical wind shear in middle latitudes, decreasing the eddy kinetic energy in middle latitudes, and accordingly decreasing the northward fluxes of heat and momentum due to large scale eddies.

The simulated variances especially in the temperature and geopotential fields resulting from the stationary eddies show a reasonable agreement with observations in both, phase and amplitude. This is to be expected, since the ocean-land differences and the topographic forcing were included in the model.

The transports by the mean meridional circulation were correctly simulated in the tropical and subtropical regions, whereas in the middle and extratropical latitudes, where the influence of such transports is generally small relative to that by the eddies, the simulated patterns do not reveal the same phase as the observations.

In all cases the difference between the simulated amplitudes of different fields between the Northern and Southern Hemispheres were correct.

The previous discussion shows that the model could be used for climate sensitivity studies. The main issue of the present study is to find the variability in the quasi-stationary ultra-long waves and long waves as a result of thermal anomalies. These types of waves are well represented by both the dynamic structure and the horizontal resolution of the model. However, the model is not appropriate for the study of smaller-scale phenomena.

4. EXPERIMENT DESIGN AND STATISTICAL METHODS

4.1 Introduction

The experiments were designed to investigate the possible teleconnections between local anomalies and the atmospheric circulation in subsequent months or seasons. As was discussed in Chapter 1, observational studies, supported by many numerical modelling results, suggested that tropical SSTAs in the Pacific ocean have significant effects on the atmospheric circulation in middle and extratropical latitudes, especially in the Northern Hemisphere. Although many observational studies also suggested that middle latitude SSTAs could have a significant effect on the atmosphere there, most of the numerical experiments failed to support such a hypothesis. The negative phase of the Southern Oscillation is defined as low surface pressure anomalies in the tropical east Pacific and high surface pressure anomalies in the Indonesian region. A certain SSTA pattern was found to be associated with the negative phase of the Southern Oscillation. This pattern may be identified by the presence of warm water in the equatorial east Pacific (El Nino) and cold water in the central and western parts of the North Pacific. Horel and Wallace (1981) suggested that this phase of the Southern Oscillation is associated with an anomalous mid-tropospheric pressure pattern in the middle and extratropical latitudes. The major features of this mid-tropospheric pressure anomaly are high pressure in western Canada and low pressure over the southeastern United States and in the North

Pacific. This distribution was supported by the results of experiments using a linear model (Hoskins and Karoly, 1981).

One phase of the experiments performed in this study is the investigation of the effect of the SSTA in the Pacific Ocean using a more realistic nonlinear model with topographic forcing. The time changes of nonlinear interactions are important in middle and extratropical latitudes, where the advection of atmospheric variables is of a significant magnitude.

Another phase of the experiments is to examine the response of the atmosphere to mid-tropospheric thermal anomalies. It is known that surface temperature has an effect on the atmosphere through the flux of moisture and sensible heat into the boundary layer. Most numerical models do not have a detailed structure of the boundary layer, and even those which have a boundary layer fail to represent many processes that take place there. The details of the complex mechanisms by which such fluxes affect the static stability of the lower troposphere are not fully understood. Because of crude parameterizations, the thermal effects caused by lower boundary anomalies may not resemble the actual tropospheric response. El Nino events, with warm water in the tropical eastern Pacific, are associated with cloud clusters across the width of the equatorial troposphere in the central Pacific region. If the SSTAs were inserted in a complex atmospheric model, they might not actually reproduce the same cloudiness structure, and, consequently, the same tropospheric thermal influence. Here, we assume that a middle tropospheric thermal forcing exists at certain locations. The anomalies are represented by propagating waves, which simulate the easterly waves in the tropical troposphere.

4.2 Experimental Design

Starting from horizontally isothermal atmosphere initially at rest and with a constant lapse rate, the model was run for 60 days. During this period the solar declination of the sun was held constant in order to represent the first day of January. A statistically steady state is reached during these two months of integration. The simulated month of January is obtained by running the model from day 61 to day 90, the February simulation is the 30 day average from day 91 to day 120, and finally, the March simulation is the average of days 121 to 150. During the three month simulation, solar radiation is changed daily using a mean zenith angle. The simulation during these months has been done without including any anomalies. The sea surface temperatures are kept unchanged, representing the average observed values for January. The monthly simulations described above represent the control run of the model.

The results of the anomaly experiments are analyzed and compared with the appropriate month of the control run. Each experiment is started from the initial state on the first of January (day 1). The anomalies are introduced gradually with an e-folding time of 5 days in January until they reach their full amplitude through the remaining days of January, February and March. An additional run is made with the SSTA turned off at the beginning of March. In this run the anomalies are gradually removed with the same e-folding time (5 days) with which they were initiated at the beginning of January. The differences between the March run with and without anomalies will give an estimate of the "memory" of the atmosphere to different anomalies.

4.3 Statistical Significance of the Signal

The purpose of any statistical significance testing is to provide an estimate of the probability that a given experimental result can be attributed to a specific forcing or perturbation applied by the experiment. In general, any changes in the initial conditions or in the forcing of the model will cause a change in the values of a certain predicted variable. The difference between the perturbed and unperturbed fields provides a measure of the response of the model's atmosphere to such external forcing. In order to detect the response of the atmosphere caused by the different anomalies in the experiments, it is essential to estimate the inherent variability of the model itself. This is an estimate of the random variations caused by the model's internal, nonlinear dynamics (noise). If the signal from the perturbations or from the anomalies exceeds the noise level of the model, then it is considered to be a significant signal.

For estimating the noise level of the model, a set of runs is performed to simulate the same period of integration covered by the control run. Each run is done by starting with different random perturbations in the wind and temperature fields. For each case the random initial perturbations have a mean of zero, and standard deviations of 1°C in the temperature and 4 m/s in the horizontal wind components. A statistical analysis is done using the results of the random initial condition runs to calculate the variance of the temperature and geopotential fields caused by the inherent variability of the model. In this study we use the model simulation from four different, randomly perturbed initial conditions, together with the control run, to give four degrees of freedom.

We define the time average of a variable X_{ij} at a grid point ij to be $\bar{X}_{ij}$, and the ensemble average over five runs of this time average to be $\bar{\bar{X}}_{ij}$. The geographic variance, for the variable X, can be calculated from the relation

$$(S_t)^2_{ij} = \frac{1}{4} \sum_{k=1}^{5} ((\bar{X}_{ij})_k - \bar{\bar{X}}_{ij})^2. \tag{4.1}$$

The standard deviation $(S_t)_{ij}$ at each grid point is the positive square root of the above expression. The geographic distribution of the standard deviations for the temperature and geopotential fields is calculated for each of the three-month simulations.

The difference between the monthly average anomaly case (2) and the monthly average control run (1) at each grid point gives the response of the atmosphere to the specified anomaly. This difference is given by

$$\Delta X_{ij} = |(X_{ij})_2 - (X_{ij})_1| \tag{4.2}$$

The significance of the response (ξ_{ij}) is calculated using the relation

$$\xi_{ij} = \frac{\Delta X_{ij}}{(S_t)_{ij}} \quad . \tag{4.3}$$

ξ_{ij} should be larger than one for a significant response of the atmosphere. That is, the absolute value of the difference caused by the anomalies must be larger than the inherent variability of the model at a certain grid point. The larger the value of ξ_{ij}, the more confidence we can have that the change is a result of the effect of the anomalies. The value can be large due to a large difference value or a small standard deviation. According to Chervin and Schneider (1976), $\xi_{ij} \geq 4$ was found sufficient for a 5% significant level, which means that the probability of such a response arising from mere chance sampling is less

Table 4.1 Significance levels for a selection of critical values of ξ corresponding to four degrees of freedom.

ξ	1	2	3	4	5	6	7	8	9
significance level %	51.69	22.86	10.02	4.69	2.38	1.31	.77	.47	.31

than 5%. The above table from Chervin and Schneider (1976) shows the relationship between the normalized response, ξ_{ij}, and the significance level, using a two-sided statistical t test and assuming four degrees of freedom (the same number of degrees of freedom used in the present experiments).

4.4 Position and Magnitude of the Anomalies

The experiments were designed to identify the response of the atmosphere to two main types of thermal anomalies. These are the anomalies in sea surface temperatures, and the anomalies in mid-tropospheric thermal heating. The anomalies are superimposed upon the original fields on the first day of the January (day 61 of the control run) simulation. However, to introduce their effect in a gradual way, as might be the case in the actual ocean-atmophere system, we apply a certain amplifying time function with an e folding time of 5 days using the relation

$$(\text{Anom})_{ij} = (1 - e^{-\nu t})\ (\text{Amplitude})_{ij},$$

where ν is the e-folding time. In order to isolate the effects of the different anomalies, the experiments were designed to test each local anomaly separately, as well as combined with the other anomalies, when appropriate.

4.4.1 Anomalies in Sea Surface Temperature

Here, we primarily investigate the effect of El Nino in the eastern Pacific, and the cold anomalies in the Northern Pacific. However, as will be noted, we use super-anomalies in the Northern Pacific region. These are found necessary for trying to identify the atmospheric response in middle latitudes, where small values of SSTA and the short period of integration by the model (2-3 months) are not sufficient to detect the phase and amplitude of the response. Super-anomalies in those regions were used by many authors for the same reasons mentioned (e.g., Chervin et al., 1980, Shukla and Bangaru, 1981). The sea surface temperature is maintained constant through the whole period of integration, except in the periods of their initial gradual influence.

Experiment 1

This experiment describes the effect of the cold sea surface temperatures in the central and western portions of the North Pacific as they were observed during the Fall and Winter 1976-1977. However, the actual values are much exaggerated in order to identify the response, for the reasons mentioned above. Fig. (4.1a) shows the location and magnitudes of the anomalies for this experiment.

Experiment 2

The effect of El Nino is demonstrated by this experiment. This warm water phenomenon lasts for 16 months on the coast of Peru, and it has been found to have significant teleconnections with middle latitude weather. It is important to identify its effect in midlatitudes using the quasi-geostrophic model and compare the model's response with the results of other primitive equation GCMs. Fig. (4.1b) shows SSTAs for Experiment 2.

Experiment 3

This case represents the combined anomalies in experiments 1 and 2 with an additional warm anomaly along the west coast of the United States. Instead of super-anomalies in the Northern Pacific we use more realistic anomalies, with a maximum amplitude of 4°C (Fig. 4.1c).

4.4.2 Tropospheric Thermal Anomalies

Observations in the tropical atmosphere show that the low level circulation over the Atlantic and Pacific is dominated by easterly flow on the equatorward flanks of the subtropical high pressure belts near 30°N and 30°S. Superimposed upon this planetary-scale pattern are weak synoptic disturbances which move, unlike the middle latitude disturbances, from east to west. These tropical disturbances are called the easterly waves. The cloudiness in the ITCZ is modulated by the easterly waves. The cloud clusters which are observed along the ITCZ are associated with precipitation zones that accompany the regions of ascent in the easterly waves. The phase speed of such waves is 8-10 m sec^{-1} (Holton, 1979) and the longitudinal separation of the cloud bands is about 3000-4000 km, corresponding to a period of 4-5 days.

Diagnostic studies indicate that the driving mechanism of the easterly waves is the release of latent heat in the convective precipitation areas accompanying the waves. Perturbations in the amplitude of this tropospheric thermal heating source in the tropics might cause certain responses in the extratropical troposphere. The monthly average of this enhanced heating would give an extended heat source, as often assumed in numerical teleconnection experiments.

In experiments 4 and 5 we intend to investigate the effect on the atmospheric circulation of tropospheric thermal anomalies, which act as

propagating easterly waves. The anomalies will be initiated as heating waves at 500 mb in specific regions, using a trigonometric function in the form

$$(\text{Amplitude})_{ij} \cos (kx + \nu t),$$

where $(\text{Amplitude})_{ij}$ = 5°C/day, k is the wavenumber corresponding to 4000 km wavelength, and ν is the frequency corresponding to a 5-day period.

Experiment 4

The anomaly wave in this experiment is assumed to propagate along the width of the equatorial Pacific. This experiment simulates the tropospheric cloud pattern associated with the negative phase of the Southern Oscillation in which the two ITCZ's, usually located on both sides of the equator, merge to form a cloud cluster along the width of the Pacific.

Experiment 5

The response of the atmosphere to thermal anomalies south of the Himalayas are investigated. The thermal anomalies propagate at latitude 7.7°N along the Gulf of Bengal.

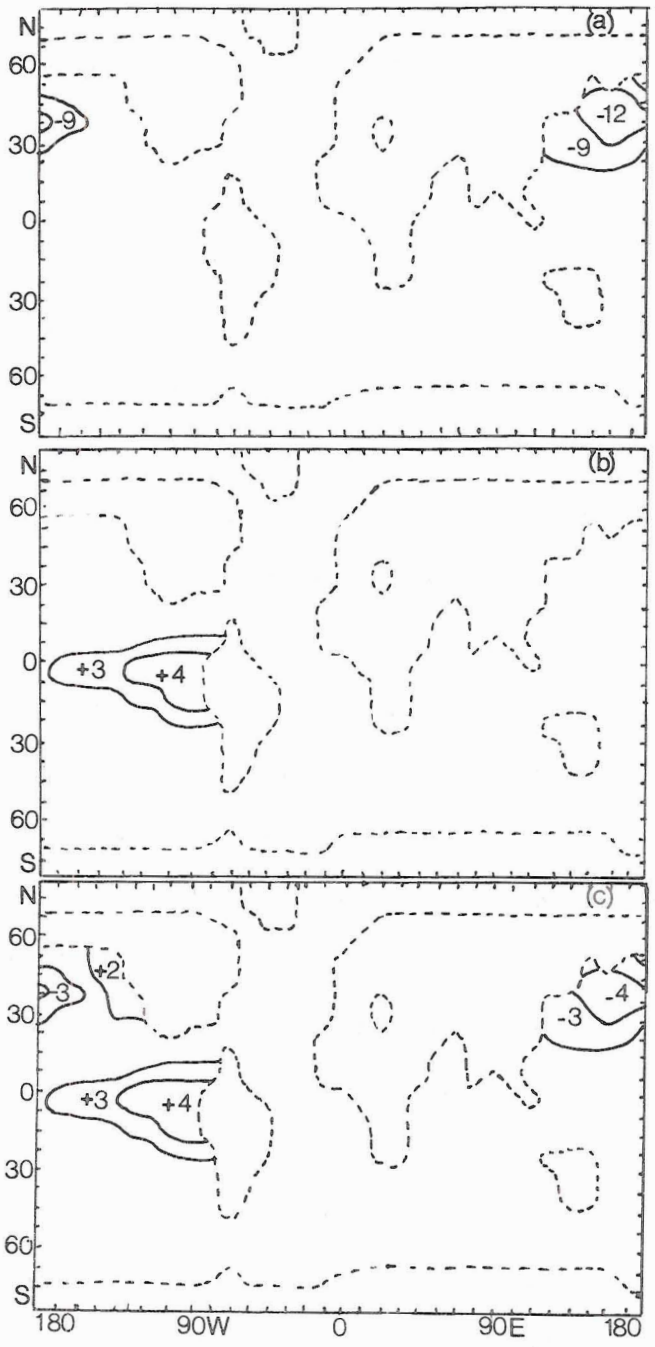

4.1 Sea surface temperature (°C) anomaly distribution. a) Experiment 1; b) Experiment 2; c) Experiment 3.

5. ANALYSIS OF THE RESULTS

Since the anomalies were introduced gradually (with 5 days e-folding time) at the beginning of January (day 61), we decided to show the difference between the anomaly runs of February (day 91-120) and the corresponding control run. This will give the model's atmosphere sufficient time to sense and distribute the effect of the different anomalies. The difference (anomaly minus control) values of the various fields representing the 30-day averages of zonal wind component, meridional wind component, 750 mb temperature, 250 mb temperature, 750 mb geopotential, 250 mb geopotential, 500 mb pressure velocity, evaporation rate, and surface pressure are discussed. The significance of such differences is investigated using the geographic distributions of the standard deviations of the temperature and geopotential height fields. The differences in the zonal averages of the different meridional transports and the differences of the variances resulting from stationary and transient eddies also are discussed. This will clarify some mechanisms that are enhanced as a result of the various anomalies. The second phase of our study is to investigate the areas that retain some memory of the anomalies after they are gone. For this purpose, the run for the month of March (day 121-150) is repeated with the anomalies turned off. A memory parameter is introduced to determine the magnitude of the remaining response to the different anomalies.

Before discussing the results of the different experiments, it will be helpful to use linear theory to predict and compare the different phases of the atmospheric response to the latitudinal positions of the low-level thermal anomalies. Following Hoskins and Karoly (1981), a steady state linearized, inviscid β plane vorticity (ζ) equation may be written in the form

$$\bar{u} \frac{\partial \zeta'}{\partial x} + \beta v' = f \frac{\partial w'}{\partial z}. \tag{5.1}$$

With the same assumptions, the thermodynamic energy equation is written in the form

$$\bar{u} \frac{\partial \theta'}{\partial x} + v' \frac{\partial \bar{\theta}}{\partial y} + w' \frac{\partial \bar{\theta}}{\partial z} = (\theta_o/g)\, Q, \tag{5.2}$$

where Q represents diabatic heating. Using the thermal wind relation, (5.2) can be modified to yield the following equation:

$$f\bar{u} \frac{\partial v'}{\partial z} - f \frac{\partial \bar{u}}{\partial z} v' + w' N^2 = Q, \tag{5.3}$$

where N is the Brunt-Väisälä frequency. Considering the thermodynamic equation (5.3), three balances may arise:

1) If the meridional advection is dominant, then

$$v \sim \frac{Q}{f\, \partial\bar{u}/\partial z} \sim \frac{Q\, H_u}{f\, \bar{u}}, \tag{5.4}$$

where H_u is the height scale of zonal velocity, $H_u = \bar{u}/(\partial\bar{u}/\partial z)$.

2) If the zonal advection is dominant

$$\frac{\partial v'}{\partial z} = \frac{Q}{f\bar{u}},$$

$$\text{or } v' = \frac{QH_Q}{f\bar{u}}, \tag{5.5}$$

where H_Q is the height scale of the heat source.

3) If the vertical advection is dominant (this can only be true away from the surface), then

$$w' \sim Q/N^2.$$

In this case the balance between the β term and the stretching term in the vorticity equation will require

$$v' \sim fQ/(\beta N^2 H_Q). \tag{5.6}$$

From (5.4) and (5.5) it is clear that the larger of the values H_u and H_Q will determine whether the heat source will be balanced by meridional or by zonal advection. To combine (5.4) and (5.5) in one relation, a parameter H is defined as the minimum of H_u and H_Q. In this case

$$Q = \frac{f\bar{u}}{H} v'. \tag{5.7}$$

(5.6) and (5.7) could be combined in a single relation by defining a new parameter γ:

$$\gamma = f^2\bar{u}/(\beta N^2 H_Q H).$$

This parameter differentiates between the two types of advection:

$\gamma >> 1$ low level heating will be balanced by horizontal advection

$\gamma << 1$ low level heating will be balanced by vertical advection

In the tropics the height scale of the heat source, H_0, is usually greater than 1 km, and γ is small. A heat source near the surface is balanced by an upward motion ($w' > 0$), which implies the creation of low level vorticity. Using the vorticity equation (5.1), this stretching is balanced by a poleward meridional motion ($v' > 0$). Thus, the surface trough must be to the west of the heat source.

In middle latitudes γ is generally large and the heating at any level is balanced by horizontal advection of temperature. A heat source is balanced by advection of cooler air from polar regions, $v' < 0$, in the Northern Hemisphere. Thus, the trough must be to the east of the source.

Similar conclusions were reached by Webster (1980) in trying to explain the significant response of the midlatitude atmosphere to tropical SSTA's, in contrast to the weak signal detected from midlatitude SSTA's. The tropical SSTA initiates a direct circulation in which warm air rises and cold air sinks, whereas in the middle latitudes the strong advection will develop an indirect circulation with rising of cold air and sinking of warm air. The two reverse mechanisms are associated with a reverse cycle for the transformation between available potential energy and kinetic energy. The above explanations, although ignoring the nonlinear interactions, still help in understanding many of the results of complex models.

The calculated average zonal wind for February is shown in Appendix 3. The Figure will help in interpreting the results of the experiments concerning the wind field.

5.1 Response of the Atmosphere to Sea Surface Temperature Anomalies

5.1.1 Negative Temperature Anomalies in the Northern Pacific

Experiment 1 was designed to examine the response of the atmosphere to a colder than normal North Pacific Ocean. This anomaly pattern may have a significant effect on the weather of the United States in the subsequent months or seasons. The experiment was initiated using super-anomalies, which do not resemble the actual observations of SSTA magnitudes. However, due to the limited time of integration of the model (3 months), we were able to identify the centers of maximum differences as a result of the anomalies. The results could lose much of their significance when using much smaller anomalies. The exaggerated anomalies were introduced, although with different amplitudes, in many numerical experiments that deal with the midlatitude SSTA's (e.g., Chervin et al., 1980; Shukla and Bangaru, 1981).

As was discussed in the previous section, a low level thermal cooling in midlatitudes is balanced primarily by an advection of temperature from lower latitudes. With the meridional wind directed northward, the surface trough should be to the west of the cold anomalies. Of course, this simple explanation will not necessarily be true in our experiments, since the model design includes more complex mechanisms (e.g., non-linearity, mountain effects) than the simple linear theory assumes.

Although the anomalies were imposed on the sea surface temperatures in the midlatitude North Pacific (Fig. 4.1a), they have a large effect on the 500 mb zonal winds in the polar and tropical regions. The response of the 500 mb zonal wind (Fig. 5.1a) shows that the major wind anomalies appear to the east of the surface thermal anomalies. The

westerlies over the west coast of the United States generally are decelerated. The westerlies are enhanced in the high latitudes over central Canada and over the tropical Pacific (Northern Hemisphere). The Southern Hemisphere has a negligible change as a result of the anomalies. The only substantial difference is the amplification of the easterlies in the tropical Pacific. The difference in the 500 mb meridional wind component (Fig. 5.1b) shows that the maximum wind anomaly appears to be a southward flow over the eastern United States. A maximum northward transport is seen to the west of Canada. Unlike the linear theory, a southward component is initiated directly above the anomaly, whereas the northward flow takes place to the east and the west of the anomaly.

The difference in the 750 mb temperature fields (Fig. 5.2a) shows that the coldest temperatures exist directly above the anomalies, illustrating the importance of the change of static stability as a result of cooler temperatures. The cold air mass extends over the central and eastern parts of the United States. A center of warm air appears over Greenland as a result of the northward transport over the North Atlantic. Although this feature of the response seems to be mainly a result of advection of different air masses east of the anomalies, a relatively strong cold air mass exists near the polar region northeast of Eurasia. The response in the 250 mb temperatures (Fig. 5.2b) shows that the difference at upper levels above the anomaly is much smaller than in the lower level. The positive difference over the North Atlantic has the same sign, but with higher magnitude, than in the lower level. The 750 mb temperature pattern shows that, in general, the anomalies tend to stabilize the atmosphere.

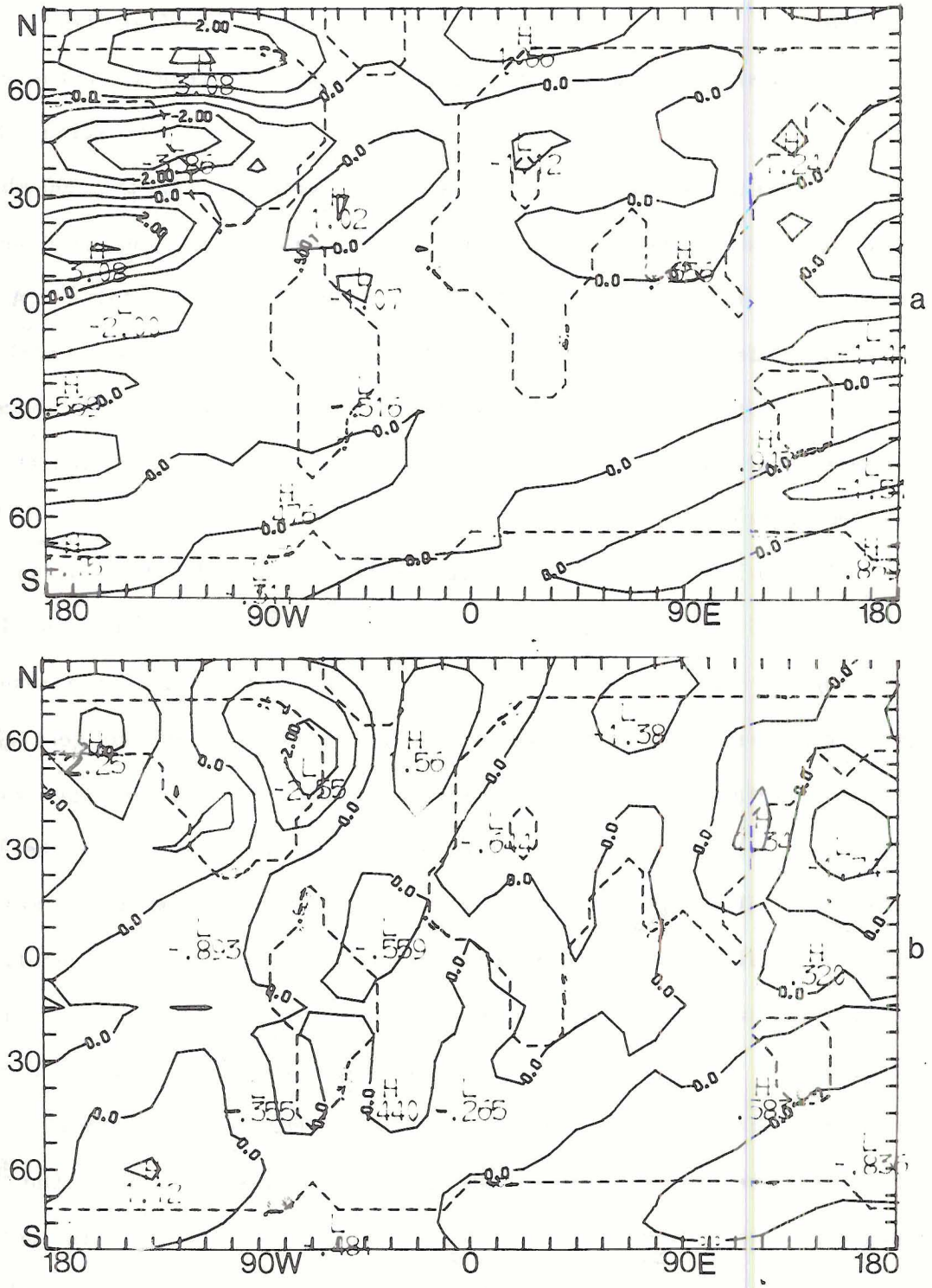

5.1 The horizontal wind difference (m sec^{-1}) at 500 mb between the anomaly (Experiment 1) and control run for February. a) zonal wind; b) meridional wind.

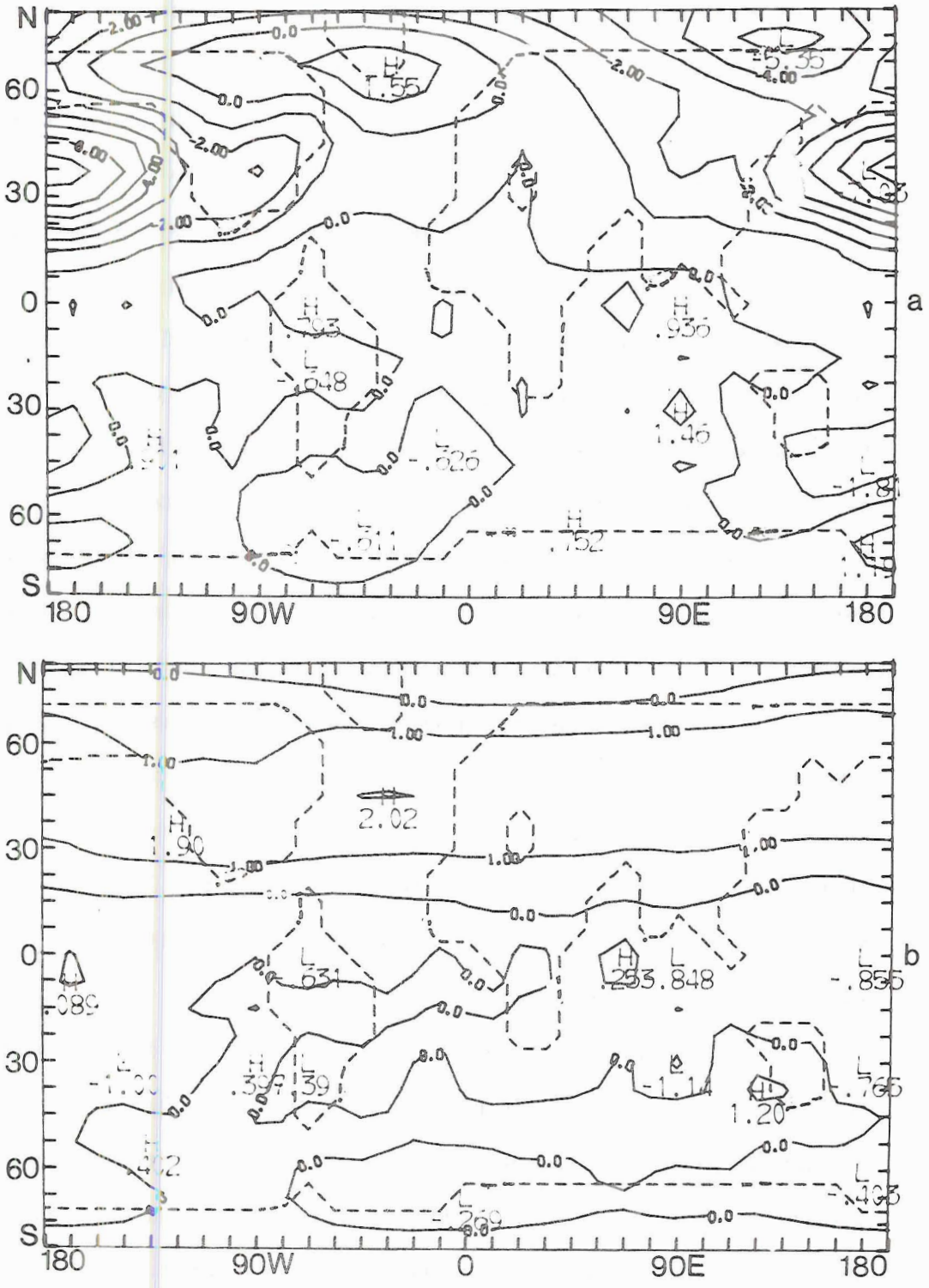

5.2 The temperature difference (°C) between the anomaly (Experiment 1) and control run for February. a) at 750 mb; b) at 250 mb.

The 750 mb geopotential height difference (Fig. 5.3a) reveals high pressure over western Canada and the United States and above the area of the anomalies. A trough of low pressure south of Greenland dominates the North Atlantic. North of Eurasia a secondary high pressure region is found. The relatively small low pressure area over eastern Eurasia, west of the anomalies (in agreement with the linear theory), gives an indication that the Siberian high becomes weaker. This low forms mainly as a result of the northward transport of relatively warm air west of the cold anomalies. The regions of cyclonic and anticyclonic vorticities induced to the east of the Rockies as a result of the anomalies have an important influence in developing the geopotential pattern over the United States. The sinking motion associated with anticyclonic vorticity, together with the southward cold air flux, act to build and extend the ridge over the southern parts of the eastern United States. The train of waves resulting from the anomalies seems to be propagating towards the northeast. The quasi-barotropic character of the response is reflected by the 250 mb geopotential height differences (Fig. 5.3b). There the differences have the same sign as in the lower level, except over the area of the anomalies, where the 750 mb positive height anomaly was replaced by a low anomaly at 250 mb.

The 500 mb pressure velocity differences (Fig. 5.4) show maxima in the regions of the Rocky Mountain and Himalayas. The differences show an inverted omega-shaped pattern over the United States, with subsiding motion over the west coast and east of the continent. Over eastern Eurasia an anomalous rising motion is initiated. Over the North Atlantic the anomalous descending and ascending motions force low-level divergence, with convergence to the west and east, which enhance the

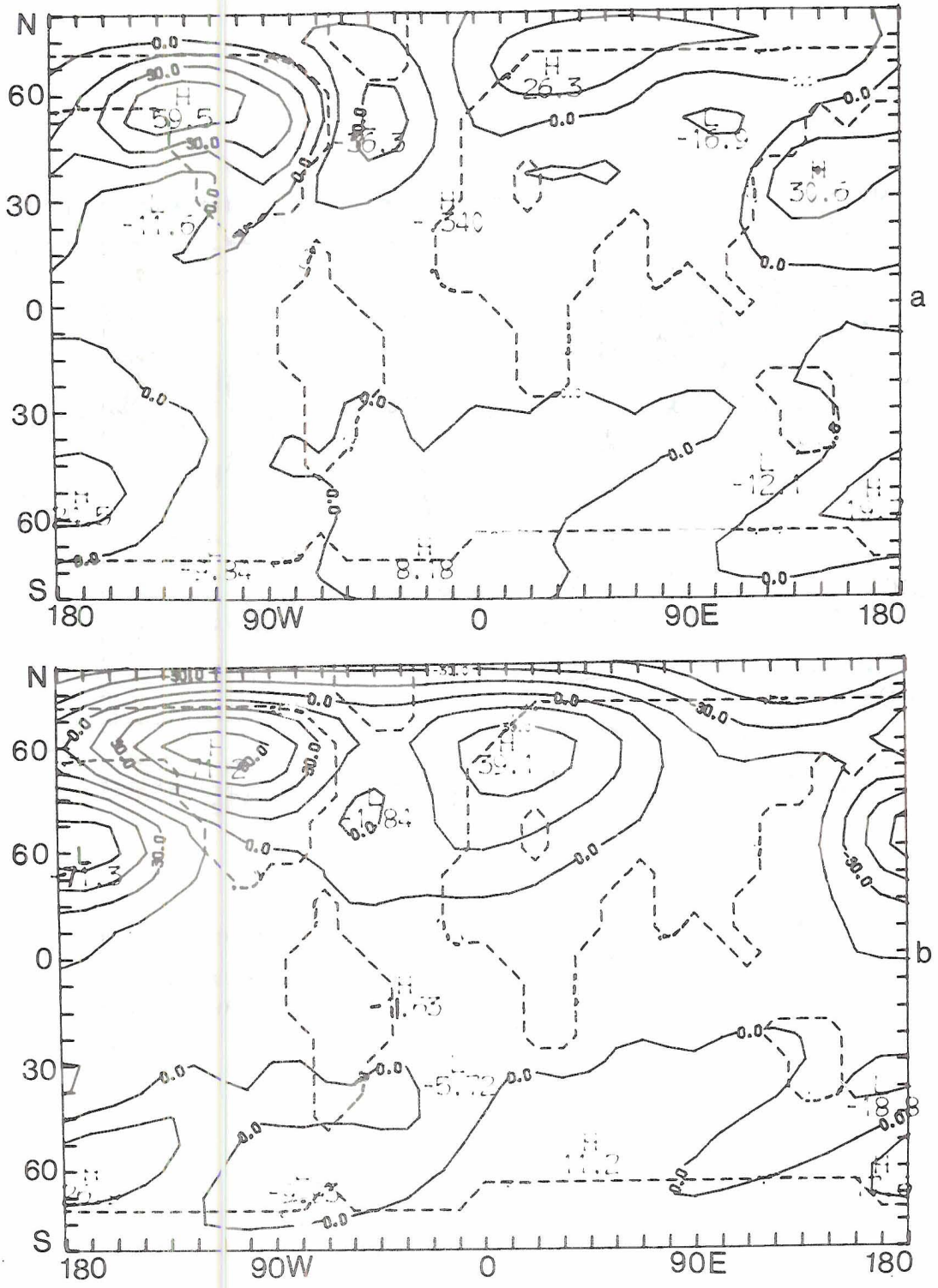

5.3 The geopotential height difference (m) between the anomaly (Experiment 1) and control run for February. a) at 750 mb; b) at 250 mb.

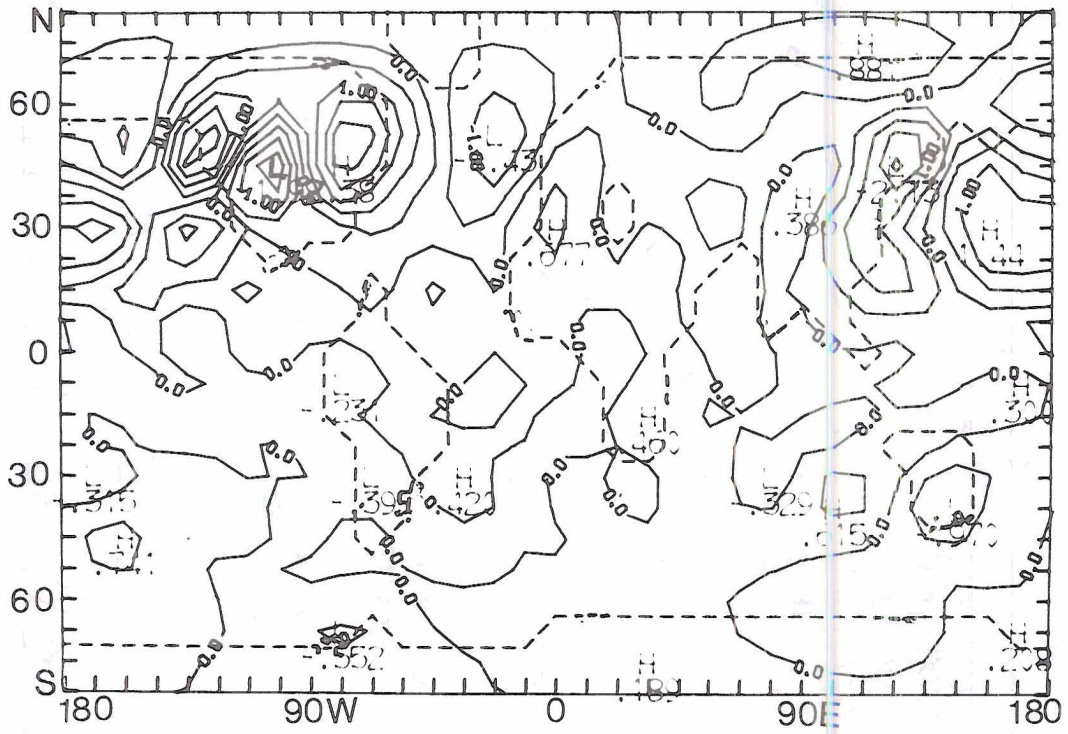

5.4 The vertical pressure velocity difference (10^{-4}mb sec^{-1}) at 500 mb between the anomaly (Experiment 1) and control run for February (negative values upward, positive values downward).

trough there over the North Atlantic. Over the western North Pacific a descending motion is initiated above the area of the anomalies.

The moisture supply to the atmosphere (evaporation rate) is largely decreased in the area of the cold temperatures (Fig. 5.5). It is increased elsewhere in the same latitude belt over the oceans. On a global basis, there is a tendency for the evaporation rate to decrease as a result of the cold SSTA. The changes are of much lower order of magnitude over the continental regions .

The surface pressure differences (Fig. 5.6) show a positive area directly above the anomalies, which extends into the eastern parts of the United States. Low pressure anomalies are seen over Greenland. Also, noteworthy is the high pressure located in the extratropical latitudes of Eurasia.

The above analysis gives a description of the main differences, which lasted for a sufficiently long period to appear in the monthly means. It is desirable to get some insight into the changes in zonal averages of the different transport mechanisms and in the variability of the energetics resulting from both the stationary and transient eddy components. Table (5.1a,b) shows the difference in the zonally averaged transports and in the variances of the temperature and geopotential fields at 500 mb.

The northward transport of sensible heat by the mean meridional circulation reaches its maximum in the subtropics and middle latitudes, compensating for the cooling effect of the anomalies. The northward transport of sensible heat by the stationary eddies is dominant in the middle and extratropical latitudes. The transient eddies seem to be the major mechanism for southward sensible heat transport in the extra-

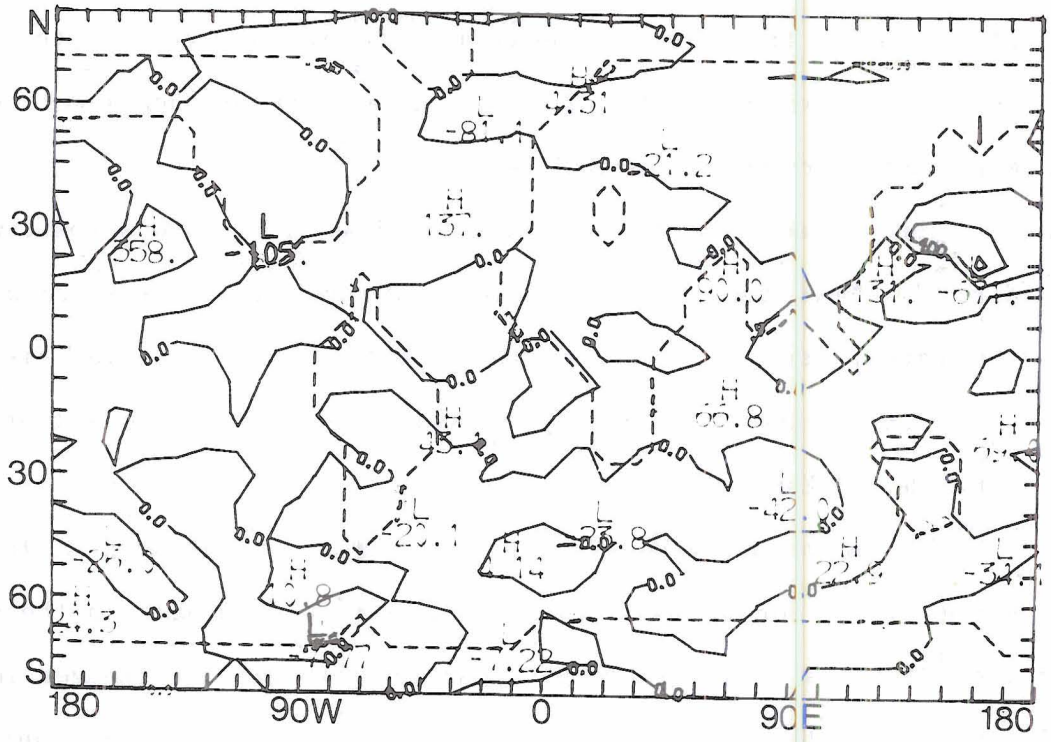

5.5 The surface evaporation rate difference (10^{-3} cm/day) between the anomaly (Experiment 1) and control run for February.

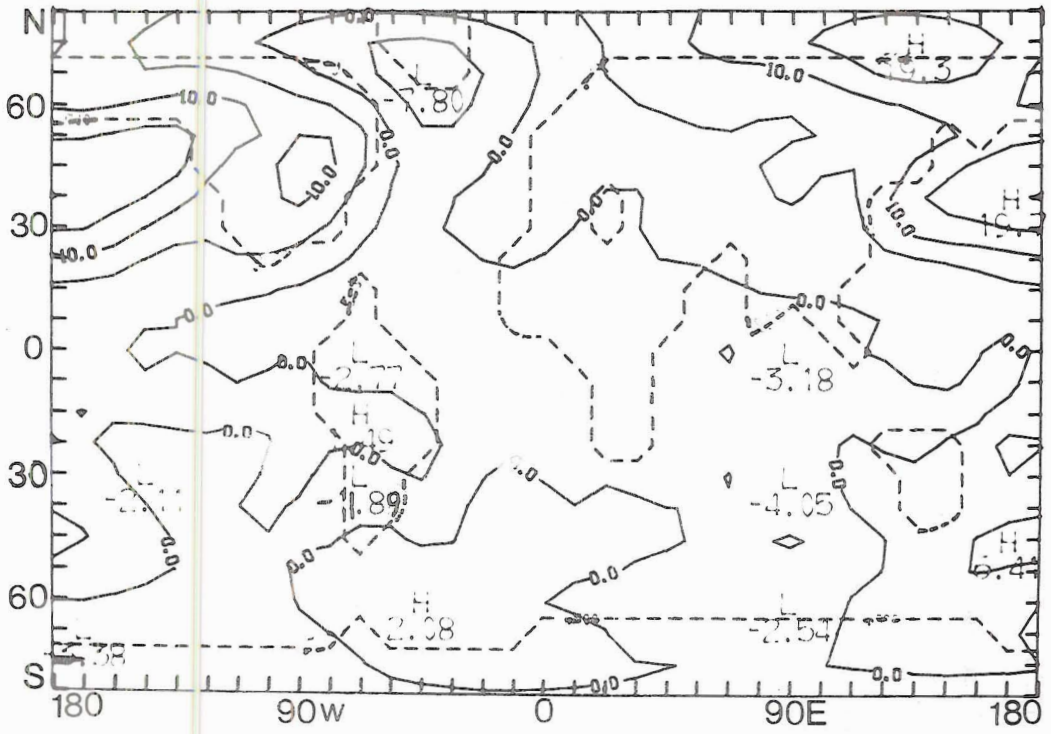

5.6 The mean sea level pressure difference (mb) between the anomaly (Experiment 1) and control run for February.

TABLE (5.1)

Experiment 1
Difference (Anomaly minus Control) in the
Zonal Average Variances and Transports

Table (5.1a)

Temperature

Latitude (North)	Eq.	7.7	15.3	23.0	30.6	38.3	45.9	53.6	61.3	68.9	76.5	84.1
Parameter												
Transport by Mean Meridional Circulation ($m\ sec^{-1}\ °C$)	-.035	-.25	-.28	.16	.8	1.05	.642	.095	-.076	.04	.182	.158
Transport by Stationary Eddies ($m\ sec^{-1}\ °C$)	.052	.005	.096	.11	-.15	-.5	-.44	.365	.742	.048	.074	.43
Transport by Transient Eddies ($m\ sec^{-1}\ °C$)	0	0	0	.01	-.01	-.01	-.04	-.25	-.48	-.52	-.52	-.37
Variances of Stationary Eddies $(°C)^2$	.025	.034	.121	.527	1.5	2.4	2.8	2.9	1.99	.518	.093	.071
Variances of Transient Eddies $(°C)^2$	-.02	-.04	-.03	.02	.07	.07	.03	-.13	-.4	-.5	-.2	.8

Table (5.1b)

Geopotential

Latitude (North)	Eq.	7.7	15.3	23.0	30.6	38.3	45.9	53.6	61.3	68.9	76.5	84.1
Parameter												
Transport by Mean Meridional Circulation ($m^2 sec^{-1}$)	.516	42.6	64.1	31.3	-30.7	-59.5	-29.6	19.8	34.2	3.3	-31.47	-27.6
Transport by Stationary Eddies ($m^2 sec^{-1}$)	.5	.4	.6	.9	.5	.8	.82	-.96	-1.1	1.35	2.97	2.2
Transport by Transient Eddies ($m^2 sec^{-1}$)	.06	.07	.14	.1	.09	.04	.23	.3	.07	-.06	-.03	.24
Variances of Stationary Eddies (10^2 m^2)	-.15	-.013	.031	.126	.21	.5	5.98	15.5	13.4	2.9	.315	.545
Variances of Transient Eddies (10^2 m^2)	.31	.3	.478	.65	.253	-.5	-1.7	-3.6	-4.7	-2.6	4.7	15.3

tropical and polar latitudes. The variance of the temperature resulting from stationary eddies tends to increase in all latitude belts, an indication of the increased land-sea temperature gradient, especially in the middle latitudes. This also indicates that most of the variability took place in the middle latitudes, as a result of the anomalies themselves and of the induced circulation over land. Meanwhile, the transient eddies seem to be damped in the latitudes north of the anomalies, implying less air exchange between the polar and extratropical latitude regions.

The differences in the geopotential height fields show two main regions of mean meridional transport of potential energy: a northward transport in the tropical region and a southward transport in midlatitudes. The transports by the stationary and transient eddies are of a lesser order of magnitude. Stationary eddies have a southward transport component north of the anomalies, where the transports by the transient eddies are insignificant. The differences in the variances of both the stationary and transient eddies are similar to those in the variances of the temperature fields. This result is expected since the height of a constant pressure level is computed using the vertical-mean temperature of the layer representing it.

5.1.2 Warm Anomalies in the Equatorial Pacific

In experiment 2, the warm SSTA's were located in the tropical Pacific of both hemispheres to simulate the effect of El Nino. It is important that we carefully analyze the results of this experiment, comparing it with the conclusions of primitive equation general circulation models which responded to anomalies in the same location. The importance of such analyses stems from the use of a linear balance

model, as used in the present study, which has its limitations in representing the tropical atmosphere. The SSTA's used here have a maximum of 4°C and minimum of 3°C (Fig. 4.1b), closely representing anomalies observed in these regions.

The 500 mb zonal wind differences (Fig. 5.7a) are relatively small. A positive anomaly component is seen in the tropical region of the Northern Hemisphere. The subtropical zonal winds are generally decelerated, especially over the continents. The midlatitude westerlies over Eurasia are enhanced. Since a considerable part of the surface anomalies lie in the Southern Hemisphere, there are some changes in zonal wind structure in this region, but with less magnitude than calculated in the Northern Hemisphere. The tropical easterlies and subtropical westerlies are enhanced. It can be noted that the anomalous westerlies are stronger than the easterlies in both hemispheres, which means that the effect of the SSTA's is to increase the zonal momentum. This result agrees with many primitive equation general circulation models concerning the effects of the similar anomalies (e.g., Rowntree, 1976a). The meridional mass transports initiated by the anomalies (Fig. 5.7b) show a northward component in the equatorial Pacific, over the North American continent and over the subtropical Atlantic. The major southward mass transport takes place over the North Pacific and over the eastern side of Eurasia. The intersection between the northerlies and southerlies in the tropical Pacific lies very close to the equator, suggesting a tendency of the low-level convergence between the northerlies and southerlies to shift equatorward. The order of magnitude of the differences in the Northern Hemisphere generally is larger than that in the Southern Hemisphere.

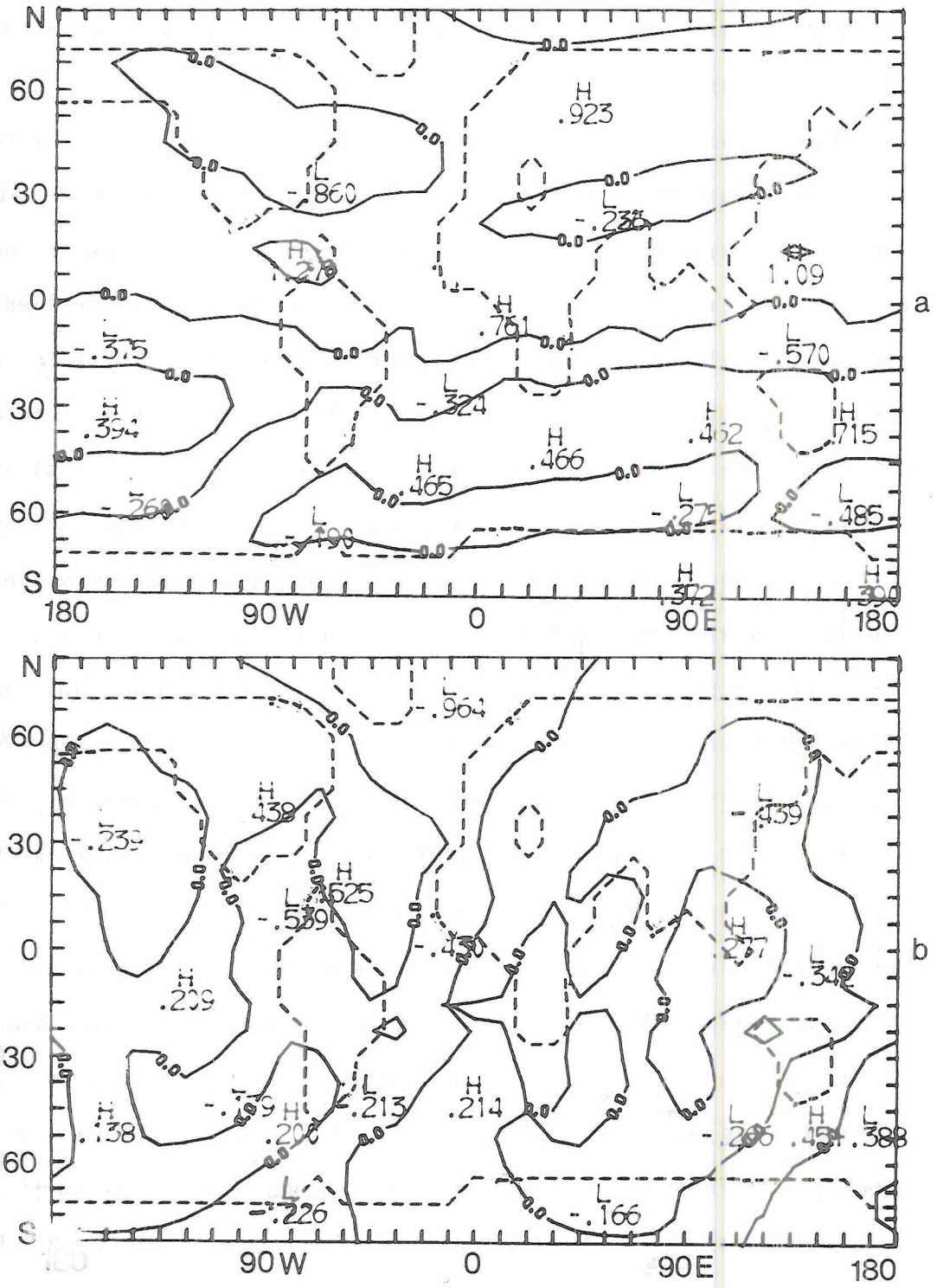

5.7 The horizontal wind difference (m sec^{-1}) at 500 mb between the anomaly (Experiment 2) and control run for February. a) zonal wind; b) meridional wind.

The differences in the temperature fields (Fig. 5.8a,b) reveal the in-situ response of the lower layer to the warm anomalies. The other temperature changes at remote locations are small in comparison (although they may be still statistically significant), being only a fraction of a degree. The larger differences appear to be at 750 mb above the oceans. There are temperature differences of opposite sign in the Pacific to the north and south of the anomaly region. The tropical regions over the Atlantic are warmed, while the subtropical regions have a continuous area of cooler air extending from the eastern United States to North Africa. The relatively large differences over the oceans are a result of the influence of the tropical warm SSTA's on the hydrologic cycle, and, therefore, on the thermal equilibrium of the atmosphere. At the 250 mb level the temperature differences in the South Pacific are almost opposite to those in the lower layer.

The geopotential height differences at 750 mb (Fig. 5.9a) show a maximum in the polar region in the form of a trough of low pressure north of Eurasia. This feature, together with anomalously high pressure east of the Mediteranean Sea, develops a westerly wind component which intensifies the middle latitude westerlies over the Eurasian continent. The second feature of importance is a high pressure anomaly over the North Atlantic and Greenland. Most of the Pacific Ocean comes under the influence of a trough with two centers, the first west of Canada and the second in the Southern Hemispheric tropical region adjacent to the location of the SSTAs. The North Pacific negative height differences agree with results from a similar numerical experiment done by Rowntree (1976a). The Aleutian low is deepened and shifted to the east, while a low pressure area develops near the surface anomaly location.

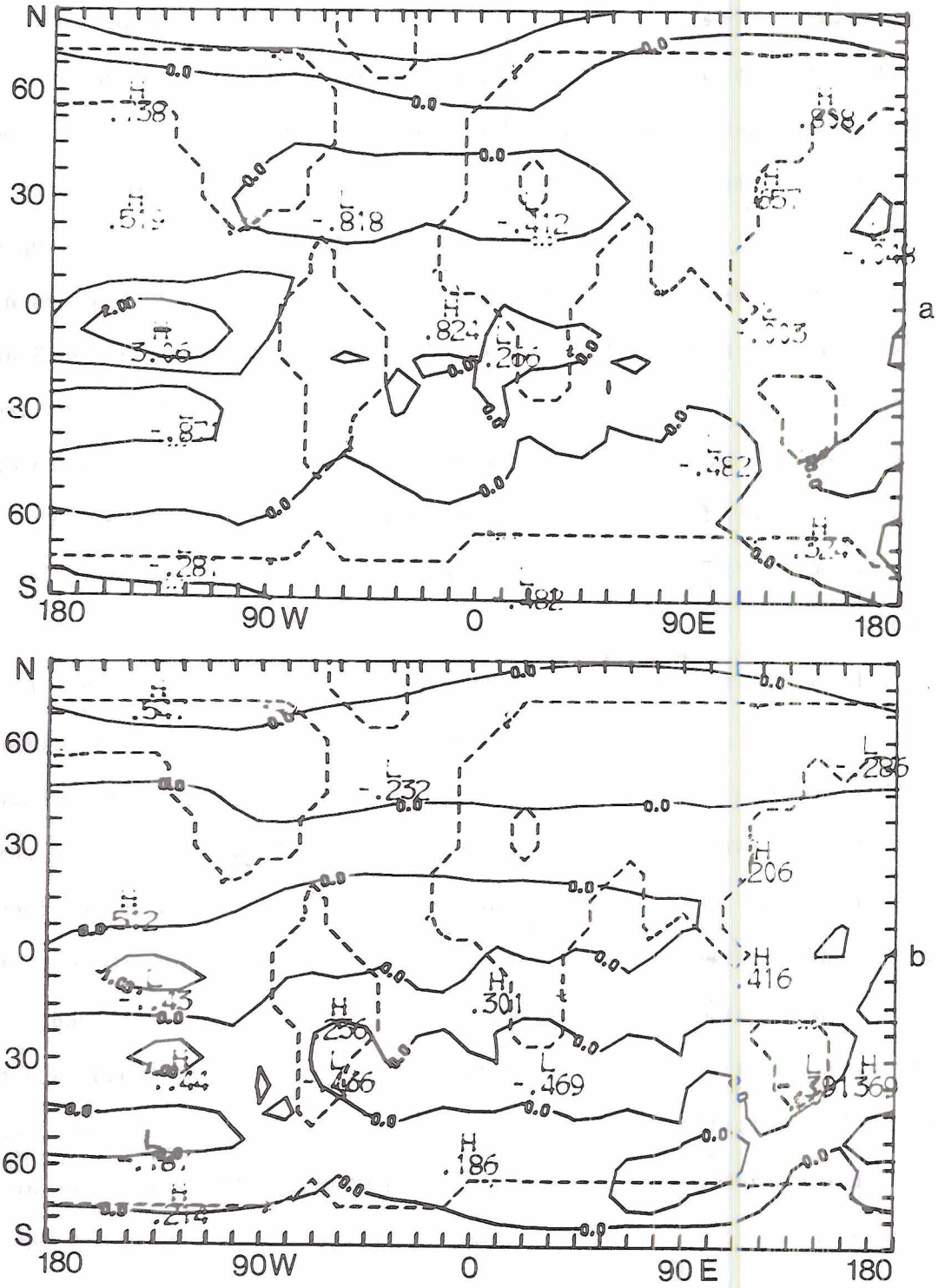

5.8 The temperature difference (°C) between the anomaly (Experiment 2) and control run for February. a) at 750 mb; b) at 250 mb.

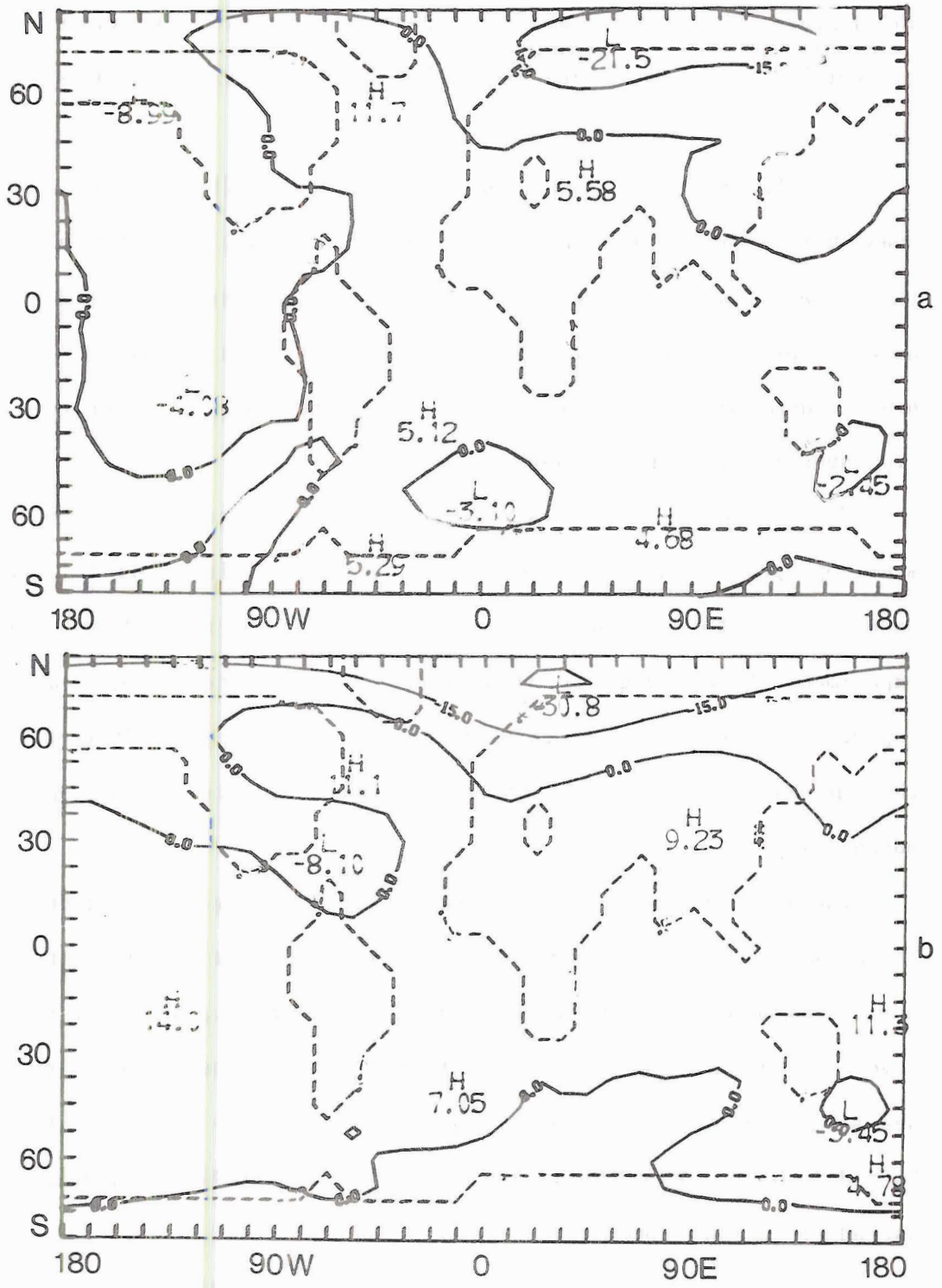

5.9 The geopotential height difference (m) between the anomaly (Experiment 2) and control run for February. a) at 750 mb; b) at 250 mb.

Our own and Rowntree's results confirm Bjerknes' (1969) hypothesis, which states that the anomalies of opposite sign over the eastern tropical Pacific and the western Pacific appear with a negative phase of the Southern Oscillation.

The 250 mb geopotential height differences (Fig. 5.9b) show the quasi-barotropic character of the atmosphere away from the anomalies (teleconnections). At the same time, directly above the anomalies, the negative pressure differences in the lower layer are changed to positive height anomalies in the upper layer, corresponding to a positive mid-tropospheric temperature anomaly.

Hoskins and Karoly (1981), using a linear model, concluded that mid-tropospheric thermal anomalies in the subtropics tend to induce a wave pattern to the northeast. However, the results of the present experiment do not support this argument. In a nonlinear model with topographic forcing and differential diabatic heating, positive SSTAs in the equatorial Pacific are not sufficient to produce the proposed geopotential pattern.

The differences in the pressure velocity (Fig. 5.10) show strong rising motion in the region of the anomalies, with the maximum to the north. This also agrees with Rowntree's experiment, where in the low-level convergence and ascending motion took place near the area of the sea surface temperature maximum. Descending motion appears east of the United States. Over the western Pacific, in the Northern Hemisphere, ascending motion takes place.

As expected, the evaporation rate (Fig. 5.11) increases in the area of the positive SSTA. A secondary evaporation maximum appears in the subtropical Atlantic in the Northern Hemisphere and in the subtropical

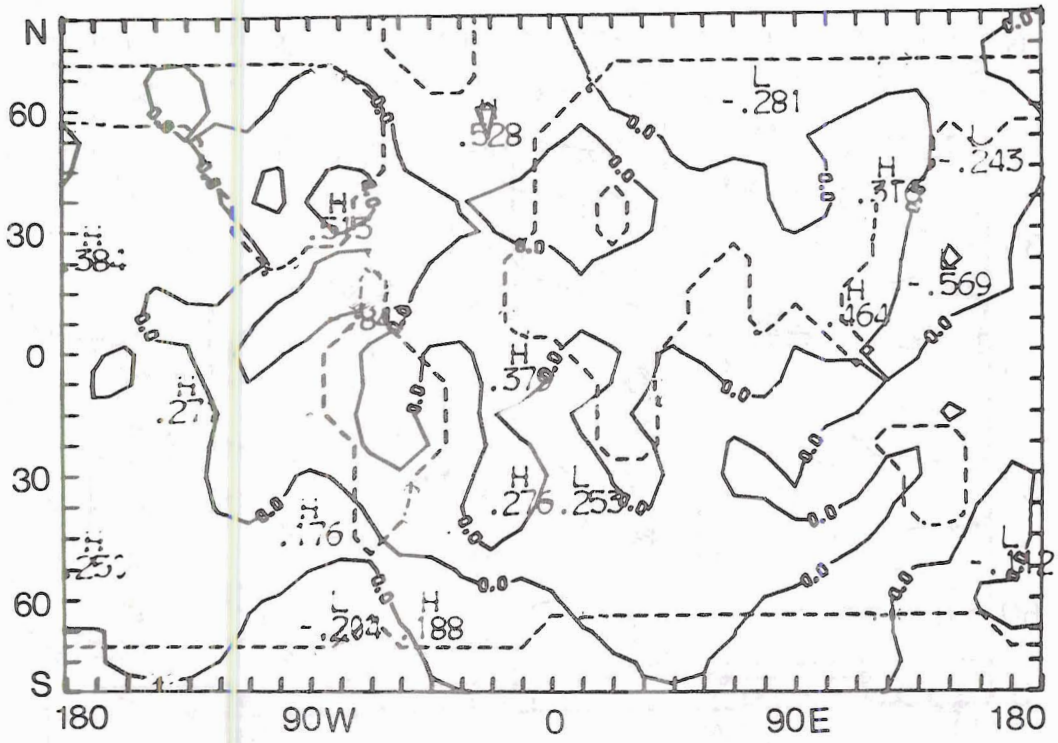

5.10 The vertical pressure velocity difference (10^{-4} mb sec^{-1}) at 500 mb between the anomaly (Experiment 2) and control run for February (negative values upward, positive values downward).

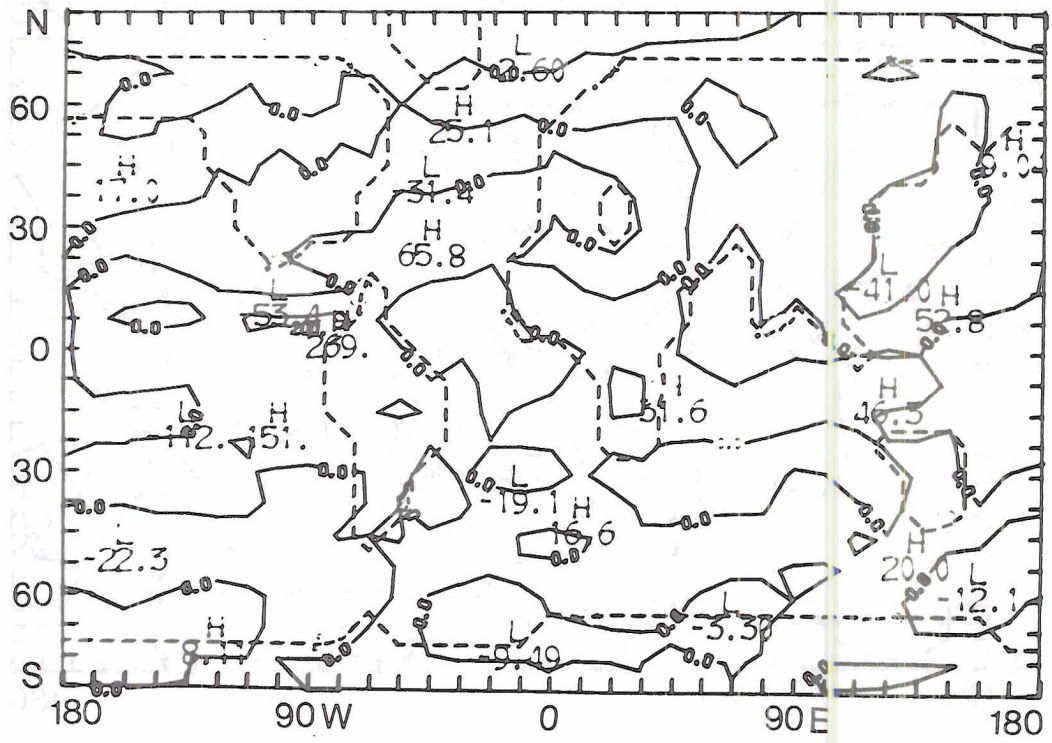

5.11 The surface evaporation rate difference (10^{-3} cm/day) between the anomaly (Experiment 2) and control run for February.

Pacific in the Southern Hemisphere. The tropical region is not a source of atmospheric moisture, due to the excess of precipitation over evaporation. The subtropical regions, which act as moisture sources, are very sensitive to any changes in the lower layer water content and temperature. The absolute value of the Southern Hemisphere differences generally are greater than those in the Northern Hemisphere due to the increased surface temperature (summer hemisphere). Again, most of the differences take place over the oceans.

The differences in the sea level pressure (Fig. 5.12) summarize the major features of the atmospheric response to the warm SSTA's in the equatorial Pacific. A surface low is induced directly above the warm surface anomalies. The center of the low pressure appears to the west of the maximum SSTA in agreement with linear theory. The Aleutian surface low is shifted to the east and deepened. The negative phase of the Southern Oscillation also is simulated as a negative surface pressure anomaly in the eastern Pacific and a positive anomaly in the Indian Ocean. The anomalies generally weaken the Siberian high, with the maximum negative values to the northeast of Eurasia.

The differences in the zonally averaged transports and variances of sensible heat (table 5.2a) indicate that the stationary eddies are the major components in the middle and extratropical latitudes which transport sensible heat to the south. Transient eddies in the high latitudes have a northward transport of sensible heat, but with a smaller order of magnitude. In the tropical region, transports by the mean meridional circulation have a higher order of magnitude than the eddy components. They are still smaller than the transports by the eddies in middle and higher latitudes. Although the surface anomalies are located in the

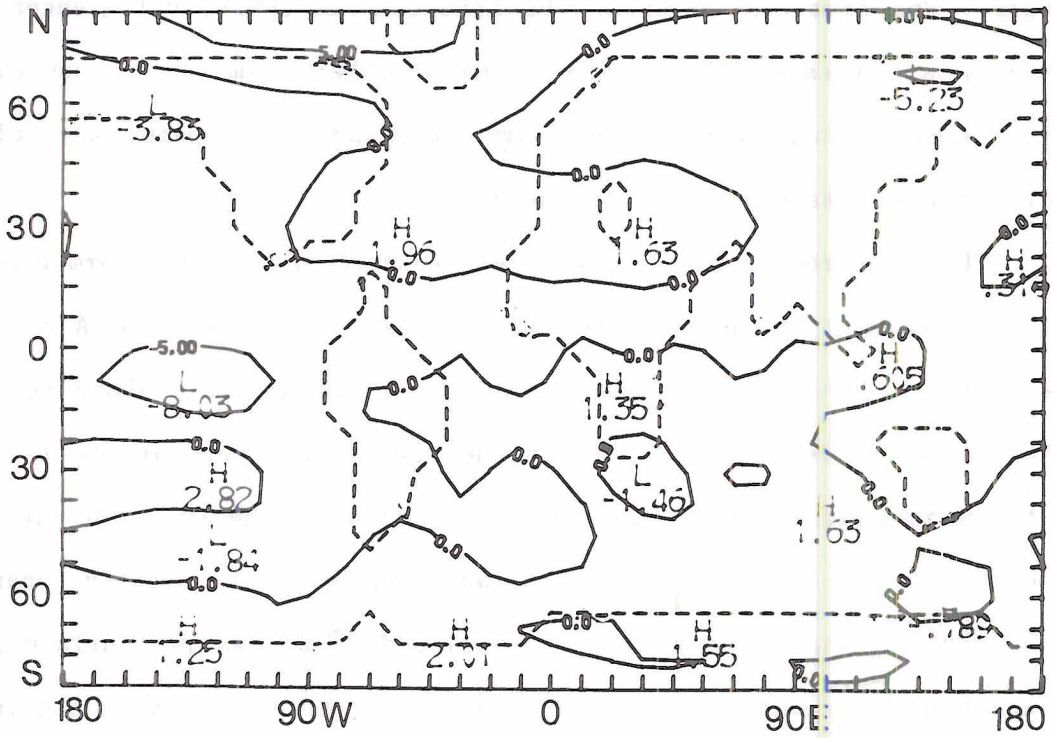

5.12 The mean sea level pressure difference (mb) between the anomaly (Experiment 2) and control run for February.

TABLE (5.2)

Experiment 2
Difference (Anomaly minus Control) in the
Zonal Average Variances and Transports

Table (5.2a)

Temperature

Latitude (North)	Eq.	7.7	15.3	23.0	30.6	38.3	45.9	53.6	61.3	68.9	76.5	84.1
Parameter												
Transport by Mean Meridional Circulation ($m\ sec^{-1}\ °C$)	-.119	-.072	.004	.052	.036	-.016	-.026	.001	-.013	-.049	-.05	-.025
Transport by Stationary Eddies ($m\ sec^{-1}\ °C$)	.024	.015	-.007	-.033	-.059	-.026	-.03	-.26	-.65	-.802	-.725	-.439
Transport by Transient Eddies ($m\ sec^{-1}\ °C$)	0	.001	-.001	-.004	-.009	-.013	-.005	.042	.11	.164	.168	.092
Variances of Stationary Eddies $(°C)^2$	-.008	-.008	.006	.028	-.05	-.23	-.29	-.367	-.66	-.56	-.161	-.007
Variances of Transient Eddies $(°C)^2$	.016	.006	.001	.001	.011	.043	.064	.05	.045	.121	.242	.285

Table (5.2b)

Geopotential

Latitude (North)	Eq.	7.7	15.3	23.0	30.6	38.3	45.9	53.6	61.3	68.9	76.5	84.1
Parameter												
Transport by Mean Meridional Circulation ($m^2 sec^{-1}$)	3.78	-2.9	-8.8	-6.0	2.15	4.9	-.8	-6.2	-1.4	11.7	19.7	13
Transport by Stationary Eddies ($m^2 sec^{-1}$)	-.066	.192	.211	.297	.589	.624	.856	.56	.012	.29	-.37	-1.0
Transport by Transient Eddies ($m^2 sec^{-1}$)	-.01	-.002	-.016	-.023	-.04	-.007	-.001	-.086	-.076	-.05	.02	.084
Variances of Stationary Eddies (10^2 m^2)	+.015	0	-.08	-.112	.185	.536	.08	-1.5	-3.6	-4.9	-4.07	-1.2
Variances of Transient Eddies (10^2 m^2)	.004	-.021	-.042	-.057	-.012	.133	.117	-.092	.034	.027	-1.08	-2.77

equatorial regions, the maximum southward sensible heat transports by the stationary eddies are found in the extratropical latitudes. The same conclusion can be drawn from the differences in the variances of temperature resulting from stationary eddies. The extratropical latitudes reveal a maximum negative change as a result of the prevailing warming trend above the continental regions. The temperature gradient between land and sea is reduced. At the same time the variances of temperature resulting from transient eddies are increased in the middle and extratropical latitudes, indicating an increase in the mixing of different air masses.

The differences in the potential energy transport (Table 5.2b) show that the transport by the mean meridional circulation is dominant in all latitudes. The sign of transport changes between different latitude belts. The transports by the stationary and transient eddies appear to be in opposite directions. The differences of variance resulting from the eddies maximize in the middle and higher latitudes and resemble the differences in the variance of temperature.

5.1.3 Cold and Warm Surface Temperatures in the Pacific

Experiment 3 represents a simulation of the effects of both SSTA areas assumed in experiments 1 and 2 without resorting to super-cold anomalies in the North Pacific. However, the cold SSTA's are still exaggerated to a certain extent (maximum negative anomaly 4°C)(Fig. 4.1c). In addition, a small area of warm anomalies is located west of the United States. The anomalies proposed in this experiment match the pattern of the SSTA's presented by Horel and Wallace (1981). According to their analysis, this pattern represents the first eigenvector (containing the major variance contribution, i.e. 23 percent) of Pacific sea

surface temperatures. It is of interest to examine the response of the atmosphere to these SSTA's and to see if it matches the hypothesis given by Horel and Wallace. The following discussion will give a good explanation of the dominant mechanisms enhancing the teleconnection between tropical and middle latitude regions.

The differences in the 500 mb zonal wind (Fig. 5.13a) show that the major increase in the westerlies is in the Pacific sector, indicating that the Pacific jet is stronger and located farther to the south. Since the westerlies over the United States generally are decreased due to the superimposed negative (easterly) component. Another area of positive wind anomalies is found north of Canada, which again enhances an anticyclonic wind shear to the south. Both these mechanisms are likely to enhance high pressure conditions northwest of the United States and a low pressure trough to its southwest. Note that the major differences are in the western hemisphere. In the Southern Hemisphere the differences are of a lesser order of magnitude. The main differences in the 500 mb meridional wind component (Fig. 5.13b) are located over the North American continent with southward component over eastern United States and northward component over the west. This feature is a result of the amplification of the Rocky Mountains of the anomalous easterly flow. The anomalous easterly flow turns to the south before it reaches the mountains. The resulting positive relative vorticity is balanced by a decrease in f (the Coriolis force) so that potential vorticity is conserved. As the air moves to the top of the mountain, the vertical column of air shrinks, and it continues to move equatorward so that the decreased depth is balanced by a decrease in f. On the other side of the mountains the process is reversed: The air

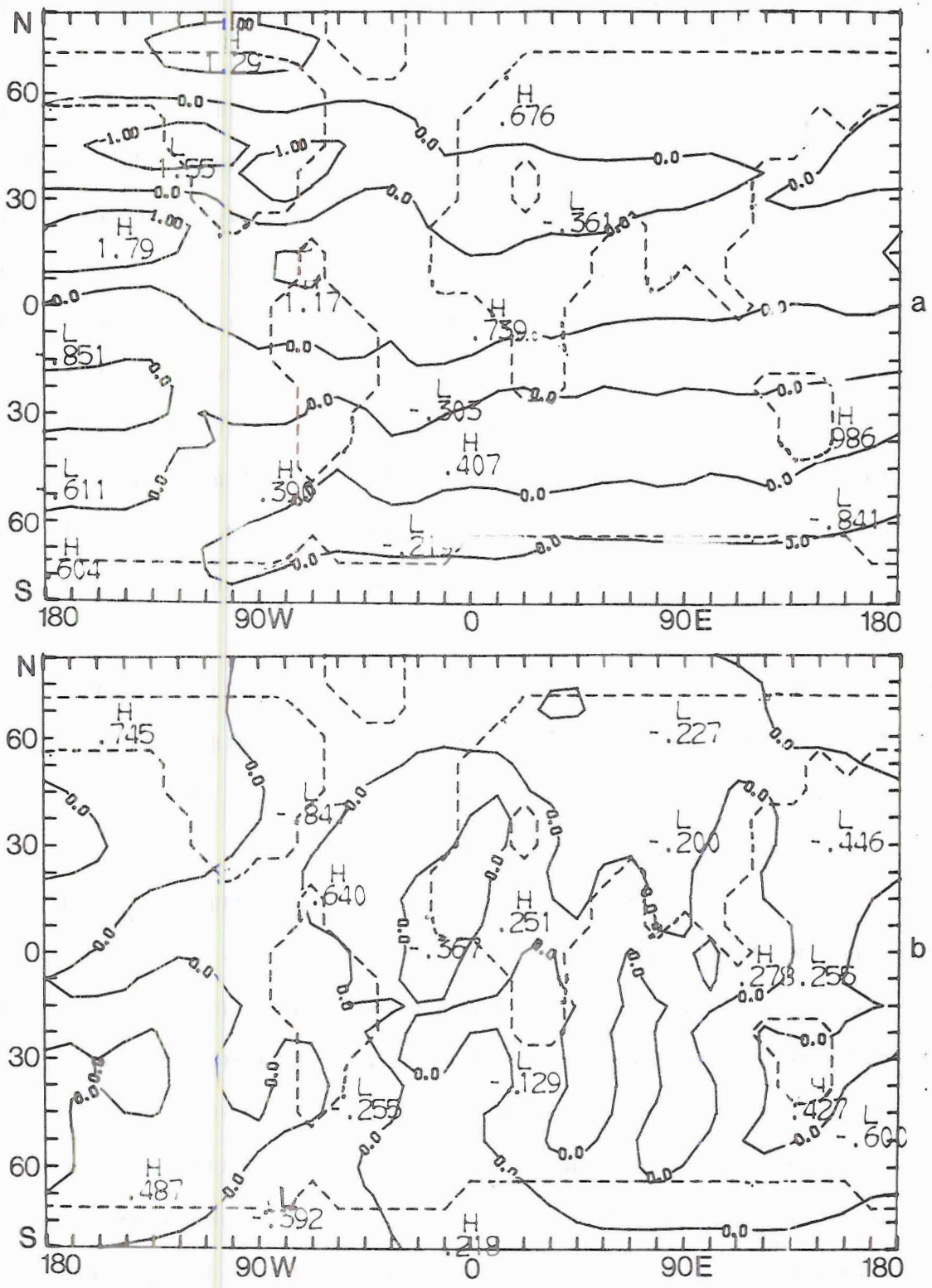

5.13 The horizontal wind difference (m sec^{-1}) at 500 mb between the anomaly (Experiment 3) and control run for February. a) zonal wind; b) meridional wind.

moves northward until it reaches the original latitude, where it goes westward.

The differences in the 750 mb temperature pattern (Fig. 5.14a) show the warm and cold pools directly above the anomalies. The south-north temperature gradient is associated with a westerly thermal wind component, which enhances the jet stream in the Pacific region. Relatively warm air in midlatitudes extends over North America and Eurasia, whereas the subtropical regions there show negative temperature anomalies. The Southern Hemisphere reveals smaller temperature differences, except for the warm center in the Southern Pacific. At 250 mb (Fig. 5.14b), the differences are smaller than those in the lower layer, with a warm center above the cold anomalies and a cold center above the warm anomalies.

The 750 mb geopotential height differences (Fig. 5.15a) reveal features of a blocking ridge over the United States, and low pressure centers on its southwestern and southeastern sides. A low pressure area also is found in northeastern Eurasia.

The 250 mb differences (Fig. 5.15b) clearly support the hypothesis given by Horel and Wallace (1981). We represent in Fig. 5.16 their Figure 11, which illustrates the hypothesized global pattern of middle- and upper-tropospheric geopotential height anomalies that occurs during an episode of warm sea surface temperatues in the equatorial Pacific during a Northern Hemisphere winter. The major features of our experiment and their hypothesis are a high pressure region over Canada, low pressure over the central Pacific, low pressure to the southeast of the United States and high pressure over the tropical Pacific. A comparison with the model results when each anomaly was investigated by itself

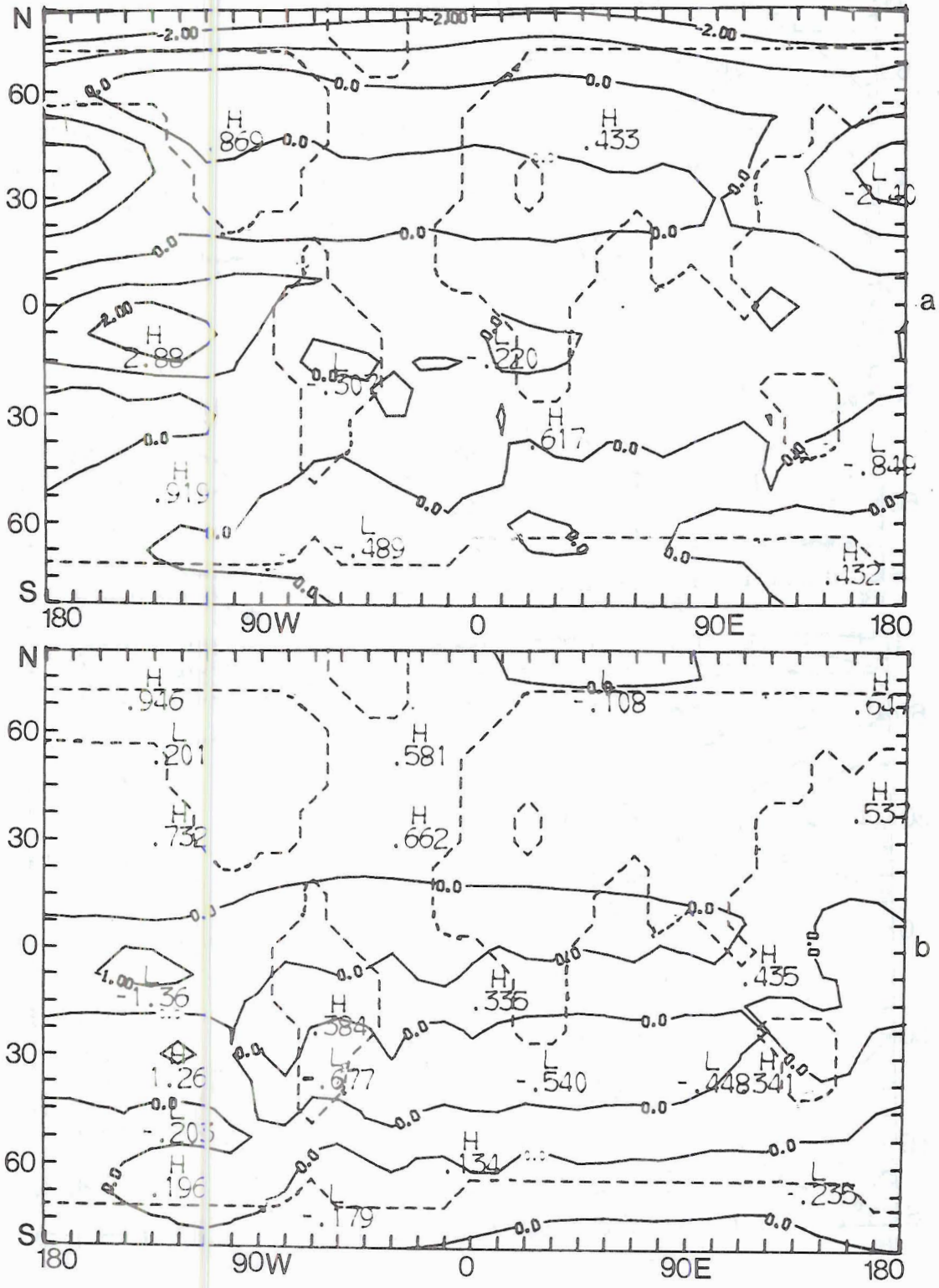

5.14 The temperature difference (°C) between the anomaly (Experiment 3) and control run for February. a) at 750 mb; b) at 250 mb.

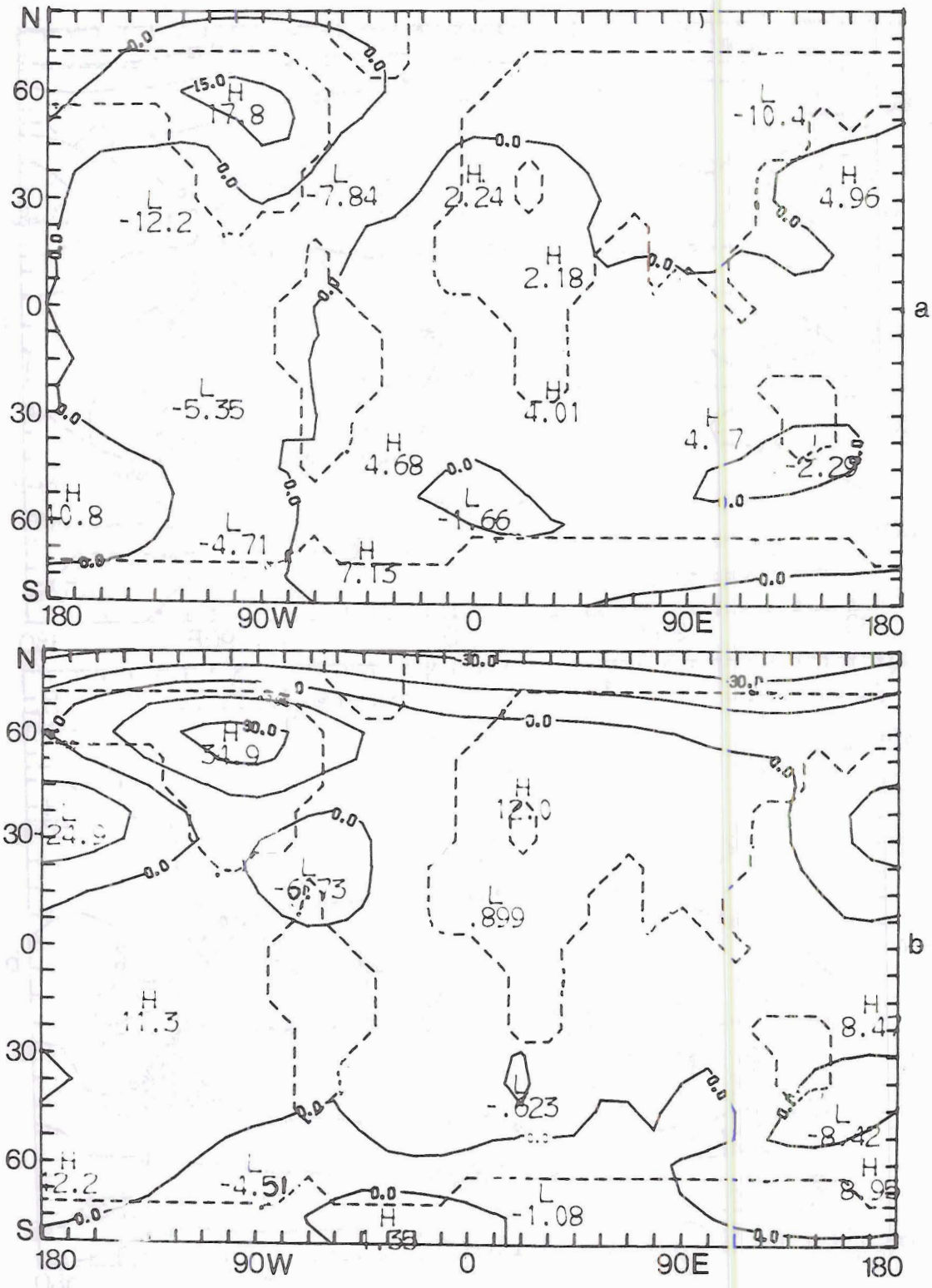

5.15 The geopotential height difference (m) between the anomaly (Experiment 3) and control run for February. a) at 750 mb; b) at 250 mb.

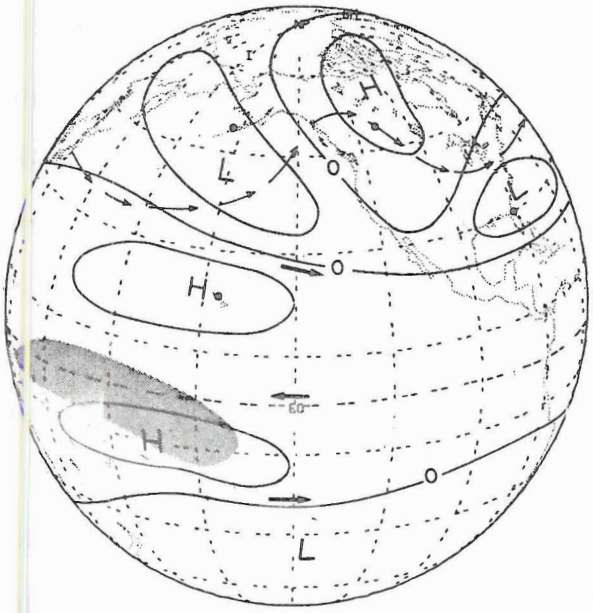

5.16 Schematic illustration of the hypothesized global pattern of middle and upper tropospheric geopotential height anomalies (solid lines) during a Northern Hemisphere winter which occurs during an episode of warm SSTA in the equatorial Pacific (after Horel and Wallace, 1981).

(experiments 1 and 2) proves that neither is capable of producing such a pattern alone. Although the mid-tropospheric thermal heating in experiment 2 is larger than in the present experiment (Fig. 5.8a,b and 5.14a,b), the response of the atmosphere in the former experiment did not support the results of the linear model by Hoskins and Koroly (1981). The negative and positive thermal anomalies to the north and south, are both necessary for producing a northeastly propagating geopotential height anomaly pattern, which closely resembles the observational study by Horel and Wallace (1981). One of the effects of both the cold and warm anomalies acting together is the horizontal and vertical wind shear created by the atmosphere in response to the surface thermal anomalies.

The differences in the 500 mb pressure velocities (Fig. 5.17) are large over the United States. However, a comparison with the relevant pattern in experiments 1 and 2 suggests that this response is a result of the temperature anomalies in the North Pacific, where the anomalous easterly component across the Rocky Mountains creates regions of cyclonic and anticyclonic circulations to satisfy the potential vorticity conservation.

The evaporation rate differences (Fig. 5.18) show that the warm anomalies cause an increase in the evaporation while the cold anomalies are associated with a decrease. As was the case in the previous two experiments, most of the variability takes place over the oceans.

The surface pressure difference (Fig. 5.19) associated with the anomalies show a low pressure area in the equatorial east Pacific, which results from the positive SSTA underneath, and a high pressure area over the cold North Pacific SSTA. The subtropical high in the Northern Hemispheric Atlantic Ocean is intensified.

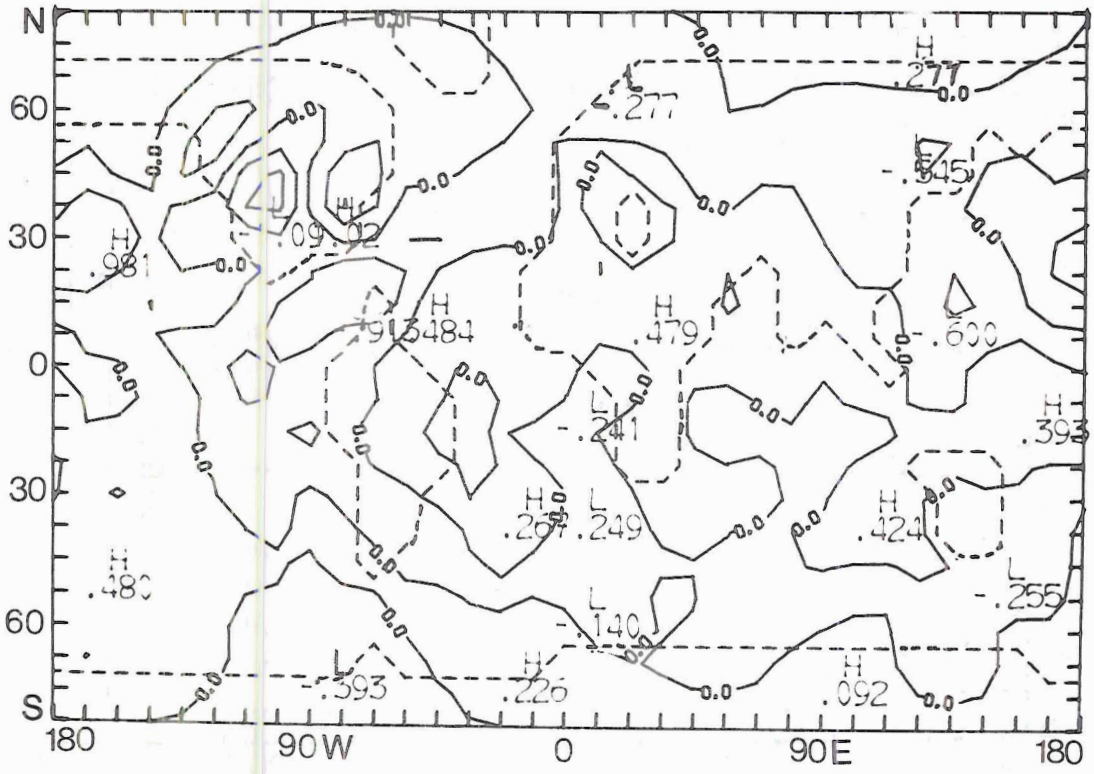

5.17 The vertical pressure velocity difference (10^{-4}mb sec^{-1}) at 500 mb between the anomaly (Experiment 3) and control run for February (negative values upward, positive values downward).

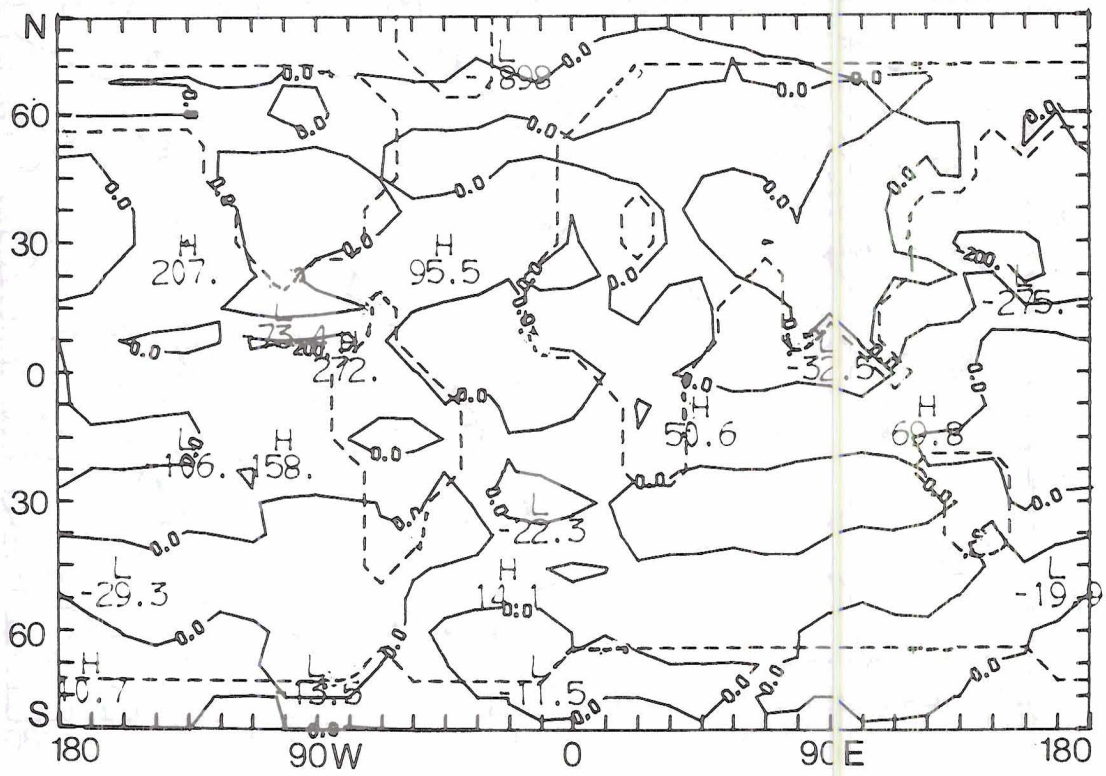

5.18 The surface evaporation rate difference (10^{-3} cm/day) between the anomaly (Experiment 3) and control run for February.

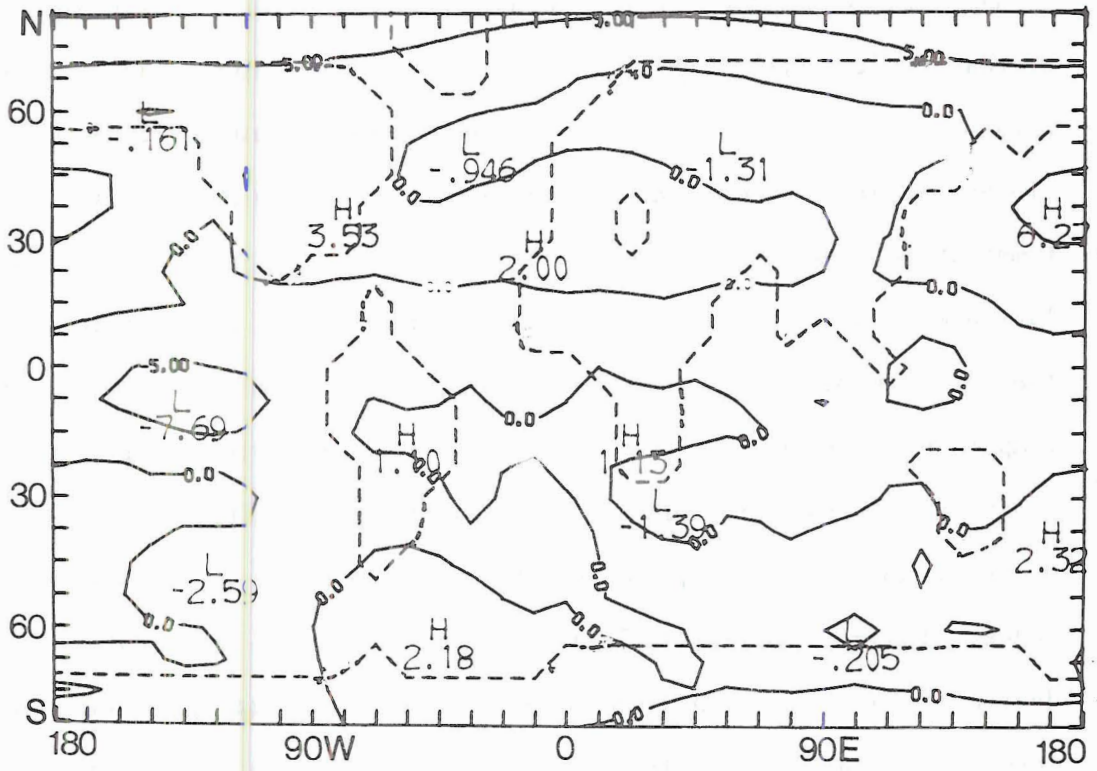

5.19 The mean sea level pressure difference (mb) between the anomaly (Experiment 3) and control run for February.

The differences in the temperature transports and variances resulting from this type of SSTA distribution (table 5.3a) show that the sensible heat transport by the mean meridional circulation is northward in the middle latitudes and southward in the low and high latitudes, whereas the transports by the stationary and transient eddies are southward in most latitudinal zones. The southward transport by the stationary eddies is the dominant mechanism north of 45°. The variance of temperature resulting from the stationary eddies is large in middle latitudes, unlike the results of experiment 2 where it was rather small. The cold anomalies in the Northern Pacific cause a larger land-sea temperature gradient. The variances of temperature resulting from transient eddies are similar to the stationary eddies; the two experiments (2 and 3) have opposite signs in middle and extratropical latitudes. Unlike experiment 2, the activity of the transient eddies is decreased in the present experiment. This result may give some insight into the variability of the atmosphere associated with the two anomaly patterns. With only a warm anomaly in the equatorial Pacific, the response of the atmosphere is transient. If the cold anomaly in the North Pacific is included, the response of the atmosphere is more of a blocking or semi-permanent type. In other words, the latter anomaly causes a change in the amplitude of the quasi-stationary waves and reduces the activity of the travelling disturbances.

The differences in the transport of potential energy (Table 5.3b) by the mean meridional circulation show a maximum southward transport in the midlatitudes. The differences in the eddy components have a lesser order of magnitude, and they are northward in nearly all the latitude

TABLE (5.3)

Experiment 3
Difference (Anomaly minus Control) in the
Zonal Average Variances and Transports

Table (5.3a)

Temperature

Latitude (North)	Eq.	7.7	15.3	23.0	30.6	38.3	45.9	53.6	61.3	68.9	76.5	84.1
Parameter												
Transport by Mean Meridional Circulation ($m\ sec^{-1}\ °C$)	-.105	-.119	-.047	.142	.327	.345	.204	.043	-.05	-.061	-.017	.01
Transport by Stationary Eddies ($m\ sec^{-1}\ °C$)	.038	.037	.044	-.008	-.141	-.21	-.241	-.209	-.321	-.576	-.484	-.157
Transport by Transient Eddies ($m\ sec^{-1}\ °C$)	.002	.002	.002	-.001	-.015	-.012	-.015	-.059	-.127	-.202	-.284	-.224
Variances of Stationary Eddies $(°C)^2$	-.019	-.017	-.006	.029	.134	.19	.231	.276	.073	-.126	-.03	.023
Variances of Transient Eddies $(°C)^2$	.02	.001	-.003	.012	.016	-.007	-.032	-.102	-.127	-.119	-.082	.063

Table (5.3b)

Geopotential

Latitude (North)	Eq.	7.7	15.3	23.0	30.6	38.3	45.9	53.6	61.3	68.9	76.5	84.1
Parameter												
Transport by Mean Meridional Circulation ($m^2 sec^{-1}$)	-.53	4.2	4.3	-3.1	-14.9	-22.1	-17.7	-3.4	13.18	23.28	21.87	11.1
Transport by Stationary Eddies ($m^2 sec^{-1}$)	.192	.442	.576	.802	.826	1.17	1.38	.214	-.453	.751	.846	.067
Transport by Transient Eddies ($m^2 sec^{-1}$)	.024	.027	.065	.045	.011	.011	.053	.068	.035	-.049	.063	.332
Variances of Stationary Eddies (10^2 m^2)	-.003	-.021	-.137	-.392	-.254	.468	1.674	2.462	.11	-3.42	-3.22	-.796
Variances of Transient Eddies (10^2 m^2)	.093	.063	.074	.062	-.133	-.418	-.991	-2.016	-2.48	-2.066	-.79	1.245

belts. The differences in the variances of potential energy resulting from the stationary and transient eddies are similar to those found in the temperature field.

5.2 Middle-Tropospheric Thermal Anomalies

In this section we consider anomalies in the atmosphere above a certain location. Tropospheric temperature anomalies may occur as a result of lower boundary temperature anomalies, as in the case of SSTA's, or as a result of changes in the troposphere itself. Examples of the latter are an anomalous release of latent heat of condensation, or changes in the major atmospheric radiation absorbers like carbon dioxide or water vapor. The case of tropospheric thermal anomaly resulting from the release of latent heat due to excessive condensation or precipitation is best described as a certain kind of propagating wave. It is unreasonable to assume that a stationary anomaly can exist in the troposphere for a long time. The release of latent heat will be maximised in areas of ascending motion, with areas of minimum release of latent heat in regions of descent. Such thermal anomalies are expected to prevail in low latitudes (i.e., near the ITCZ) because of the large moisture content and convective activity in that region.

In experiments 4 and 5 the thermal anomalies are represented by an easterly wave travelling along a certain latitude belt. The maximum amplitude of the wave is 5°C/day and the minimum is 0°C/day, resulting in an average of 2.5°C/day, which represents an excess precipitation rate of nearly 10 mm/day.

5.2.1 Thermal Tropospheric Anomalies Along the Equatorial Pacific

Experiment 4 represents the case of an equatorward displacement of the ITCZ over the Pacific in the form of a travelling easterly wave, with the associated anomalous release of latent heat of condensation.

The differences in the 500 mb zonal wind field (Fig. 5.20a) reveal clearly that such anomalies have larger responses than the SSTA's. These responses may be a result of the high amplitude used and of the direct and undiffused effect in the thermal energy equation. The lower boundary SSTA's must be linked to the conditions of the atmosphere above it in order to get a large tropospheric anomaly. It also is noticed that the differences in the Northern Hemisphere are larger than those in the Southern Hemisphere. The intensification and southward shift of the subtropical jet stream are shown. The maximum positive anomalies take place over west Eurasia, increasing the westerlies there. The easterlies are enhanced along the equatorial belt. Also the westerlies decelerate over most of the United States. The differences in the 500 mb meridional wind velocity (Fig. 5.20b) show large values near the Northern Hemispheric polar region, east of Greenland. A strong southward flow drifts towards the middle latitudes. Secondary differences exist in the form of a southward flux over eastern Eurasia and a northward flux over the North Pacific. The differences in the equatorial region are generally less than those at high latitudes.

The differences in the 750 mb temperatures (Fig. 5.21a) show a strong pool of cold air east of Greenland and a weaker warm pool northeast of Eurasia. The major differences in the middle latitudes appear as warm air over most of the United States and east of Eurasia. In the Southern Hemisphere the response is more pronounced in the subtropics,

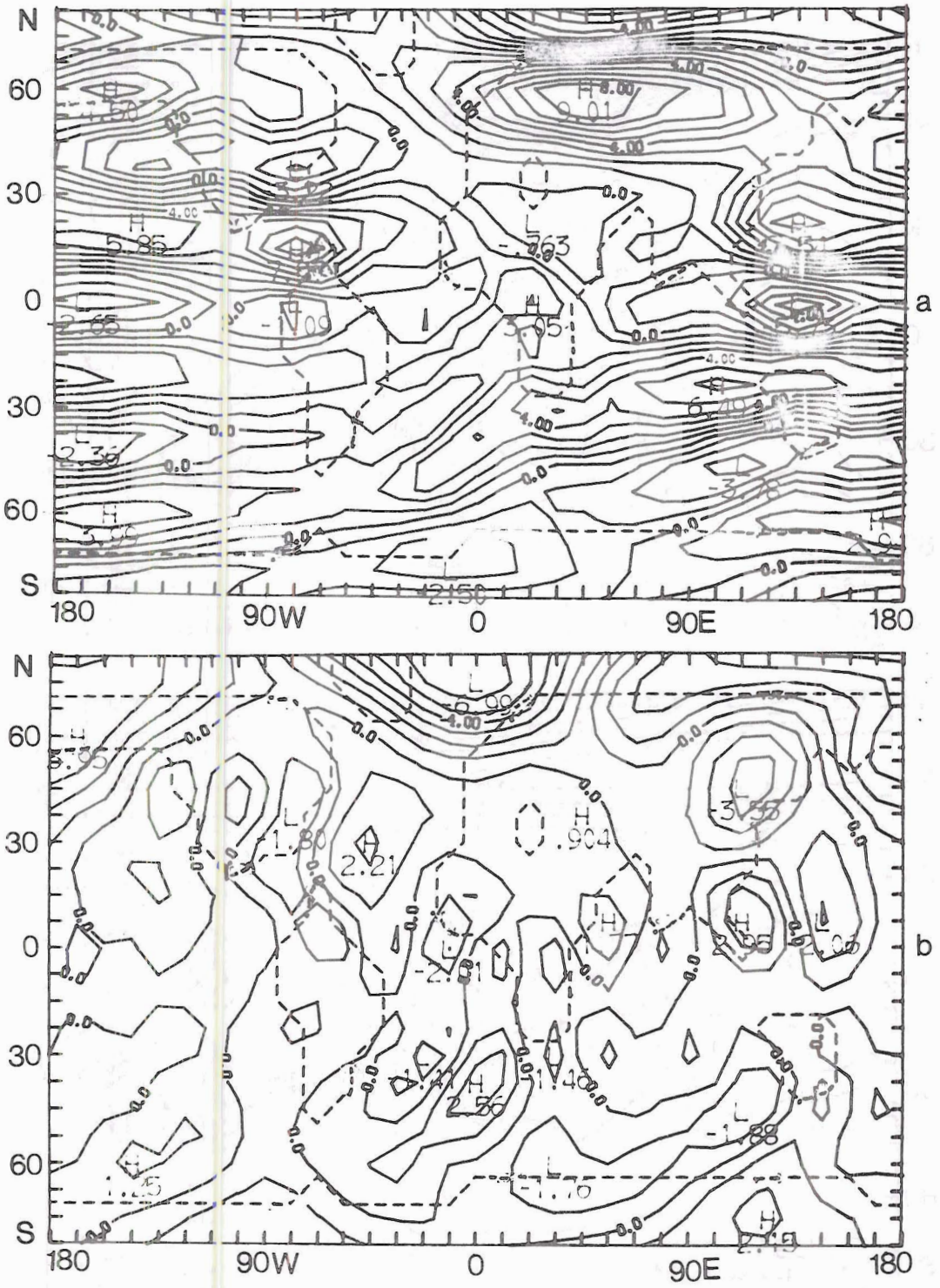

5.20 The horizontal wind difference (m sec^{-1}) at 500 mb between the anomaly (Experiment 4) and control run for February. a) zonal wind; b) meridional wind.

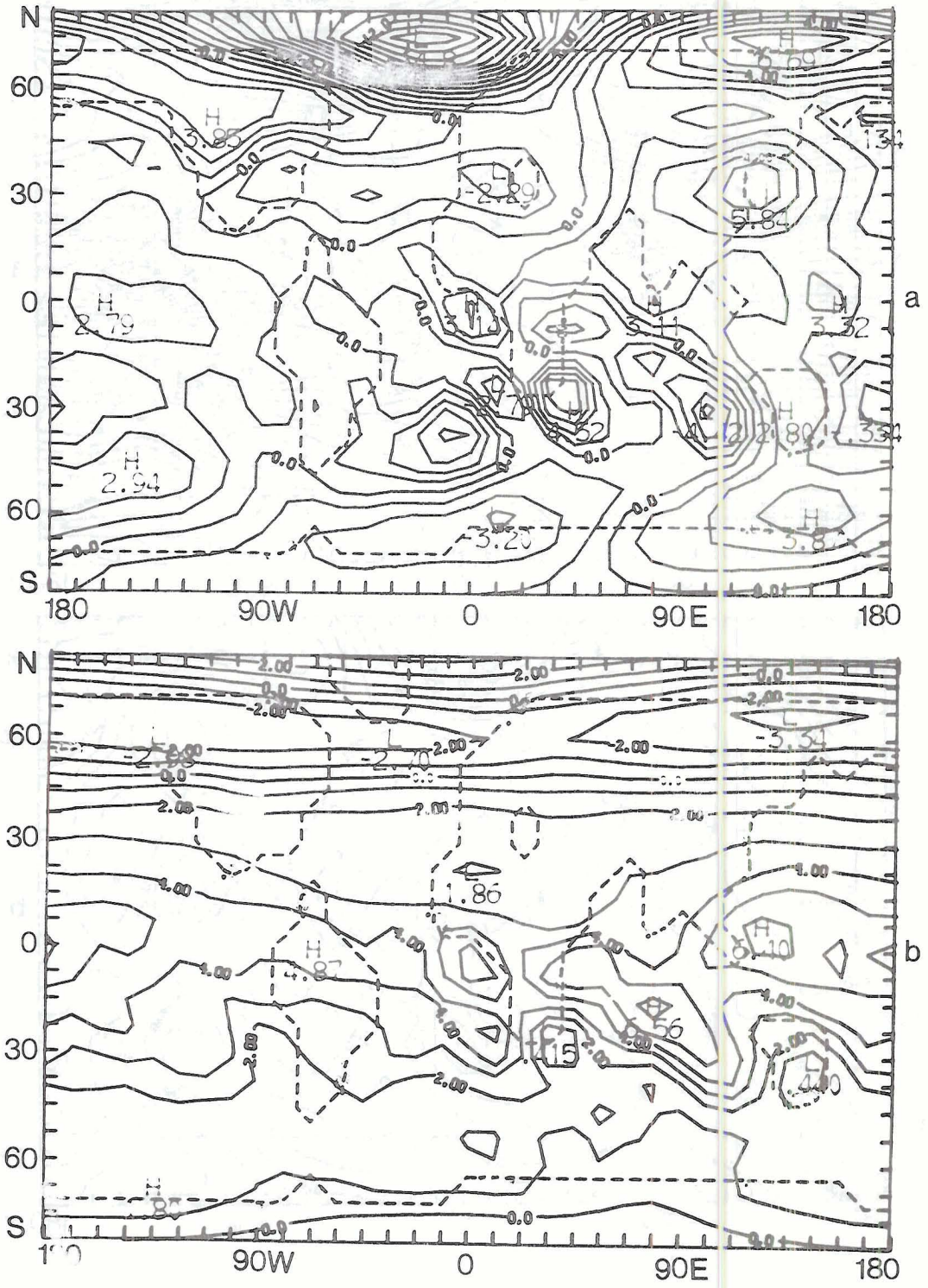

5.21 The temperature difference (°C) between the anomaly (Experiment 4) and control run for February. a) at 750 mb; b) at 250 mb.

with shorter wavelengths than already noted in the Northern Hemisphere. The 250 mb temperature differences (Fig. 5.21b) show a nearly zonal pattern in the Northern Hemisphere with a cold pool in the midlatitudes. In the Southern Hemisphere the major positive differences are in the Indian Ocean with cold regions over the South African and Australian regions.

The differences in the 750 mb geopotential heights (Fig. 5.22a) reveal that most of the response takes place in the high latitudes of the Northern Hemisphere, mainly in the form of a deep trough north of Eurasia and a ridge over Greenland. The trough associated with the depression over northern Eurasia is deep and reaches the western Pacific subtropics. The Aleutian low is enhanced over the west Pacific, while the Siberian high is weaker and the subtropical high is built up. Noteworthy are the anomalies of opposite sign over the United States. In the Southern Hemisphere, a low pressure area is dominant in the middle latitudes of the Atlantic with a high on the Antaractic region. The 250 mb pattern (Fig. 5.22b) shows that the major differences are nearly the same as in the lower layer.

The differences in the 500 mb pressure velocities (Fig. 5.23) show rising motion over the equatorial Pacific region associated with the thermal anomalies there. In the polar region a major sinking area appears east of Greenland and a region of ascending motion of comparable magnitude over northern Eurasia. The mountains generate anomalous circulations in between these two regions. The tropical warm anomaly initiates a local low-level convergence accompanied by an ascending motion. The continuity of mass requires that air must descend in other regions. The descending air carries the properties of its original

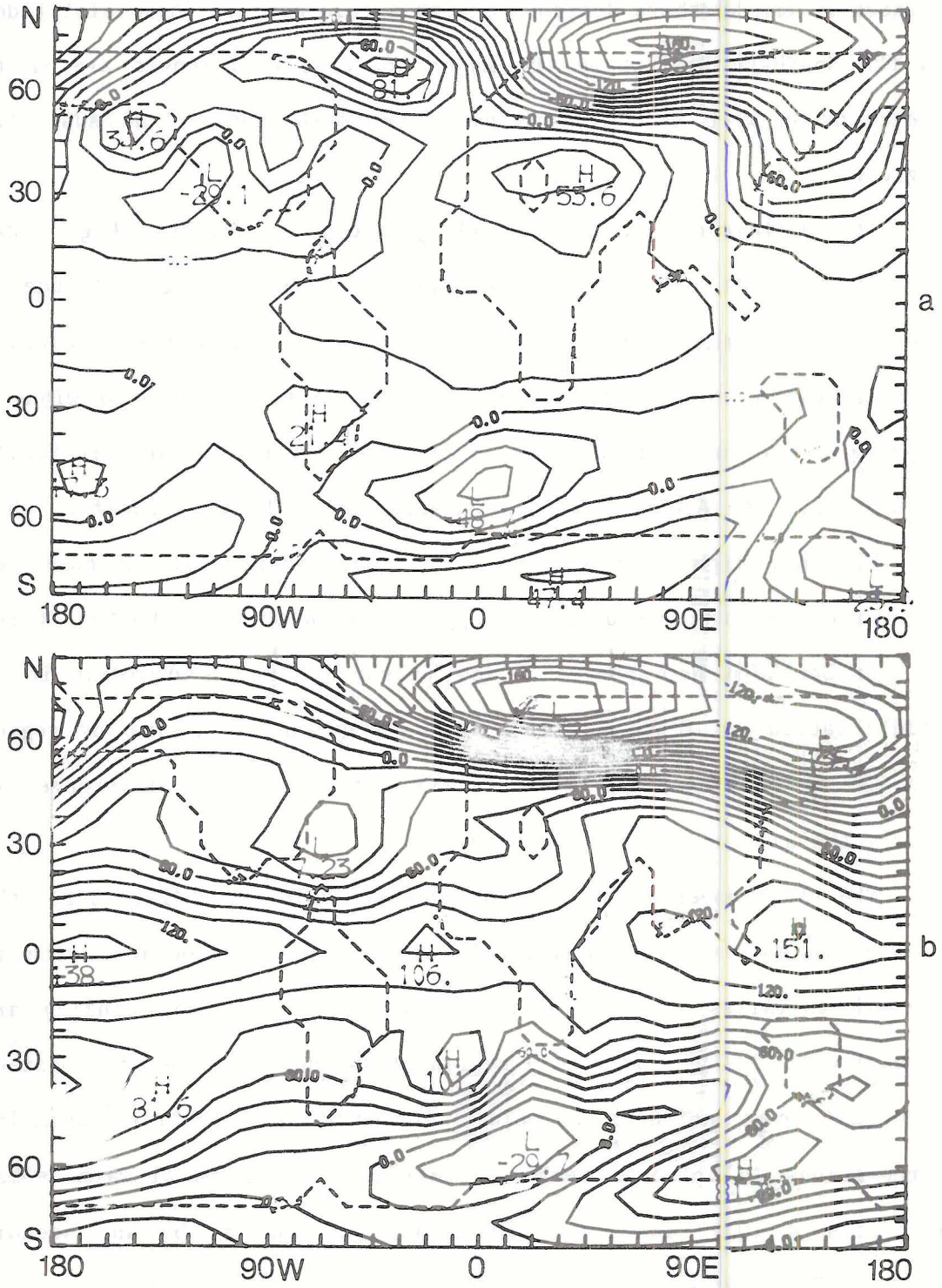

5.2: The geopotential height difference (m) between the anomaly (Experiment 4) and control run for February. a) at 750 mb; b) at 250 mb.

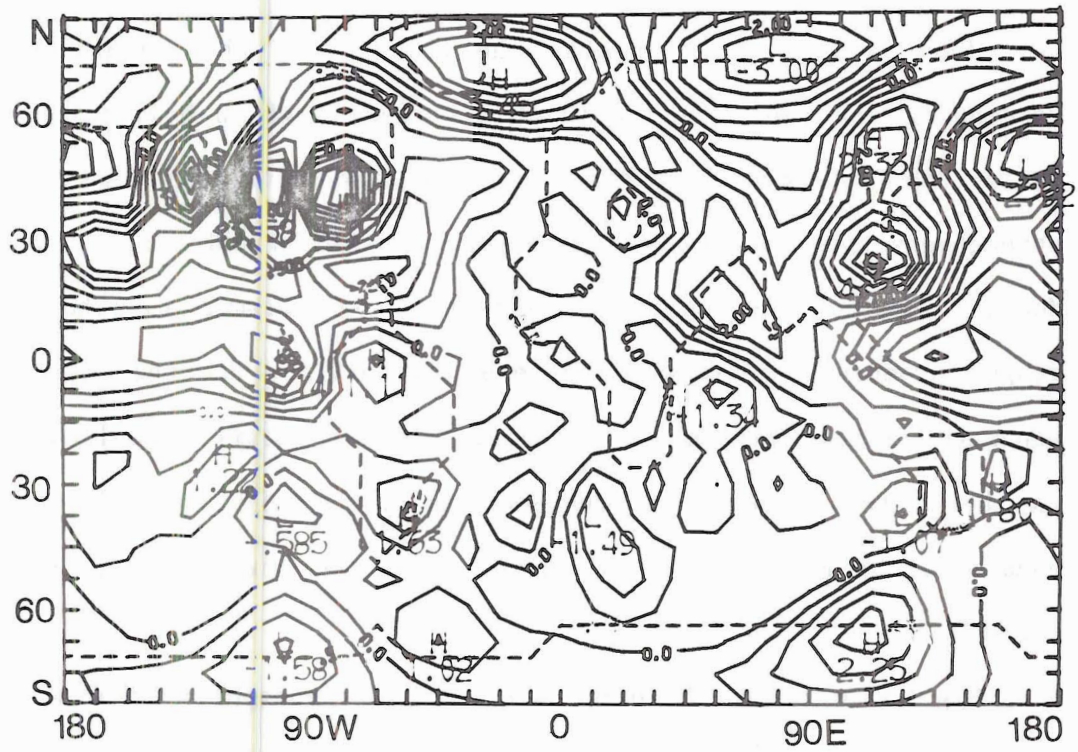

5.23 The vertical pressure velocity difference (10^{-4} mb sec^{-1}) at 500 mb between the anomaly (Experiment 4) and control run for February (negative values upward, positive values downward).

layer. The strong subsidence in the area of the Himalayas is very significant, since the subsiding air is of high momentum due to the existence of the subtropical jet stream there. The colder air coming from above is the major cause for building the ridge in the subtropics over Eurasia and for deepening the trough over the western Pacific. Descending air causes a low-level divergence, which builds the ridge, while the low-level convergence associated with the ascending air strengthens the trough to the east. In the United States the Rocky Mountains modify and amplify the effects of the anomalies. The mountain ranges produce a short-wave pattern that divides the country into two separate climate regions, as usually observed during anomalous winters in the United States. In the Southern Hemisphere the effects of the equatorial anomalies also are shown through the subsidence in the polar region.

Fig. 5.24 shows the effects of middle-tropospheric thermal anomalies on the surface evaporation rate. The main differences are found in the subtropical oceans in both hemispheres. The circulation induced by the anomalies, specifically by the 750 mb temperature and horizontal wind anomalies, is the major reason for the evaporation anomalies, since the sea surface temperatures are fixed.

The surface pressure difference (Fig. 5.25) are similar to those of the geopotential heights at 750 mb. The major response occurs in the extratropical latitudes of the Northern Hemisphere, with high pressure east of Greenland, low pressure north of Eurasia and an extended trough over the subtropical west Pacific. The subtropical high is intensified. In the tropical Pacific area of the anomalous heating, a small surface low pressure anomaly appears. The differences usually increase with latitude in both hemispheres.

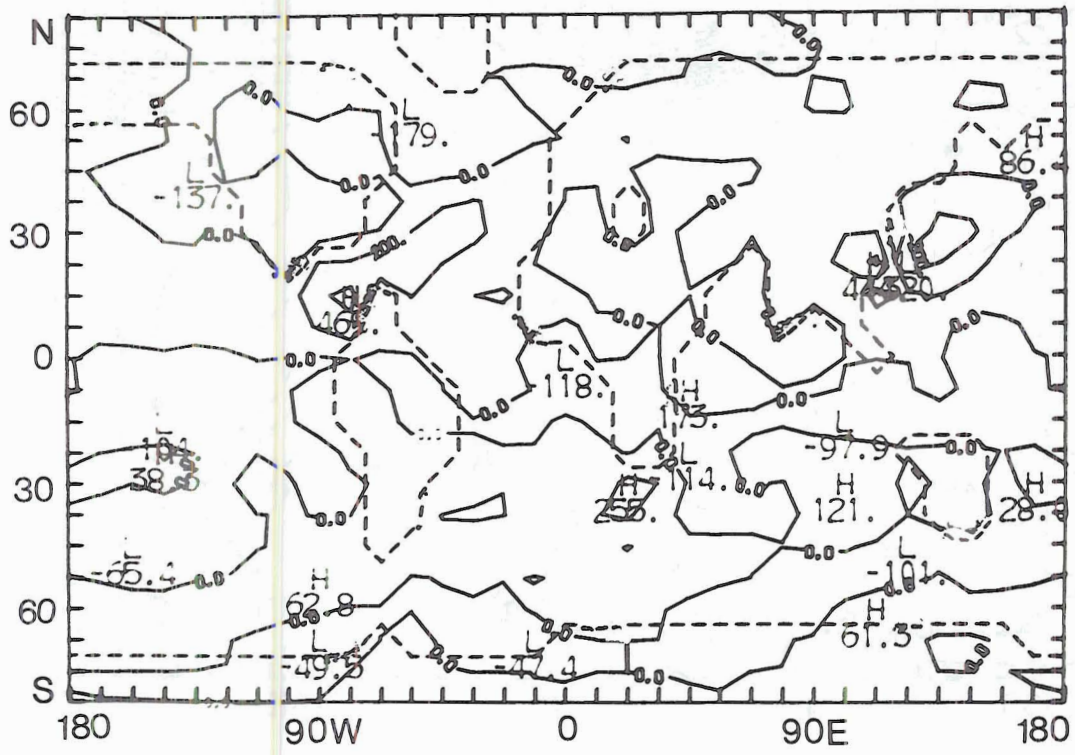

5.24 The surface evaporation rate difference (10^{-3} cm/day) between the anomaly (Experiment 4) and control run for February.

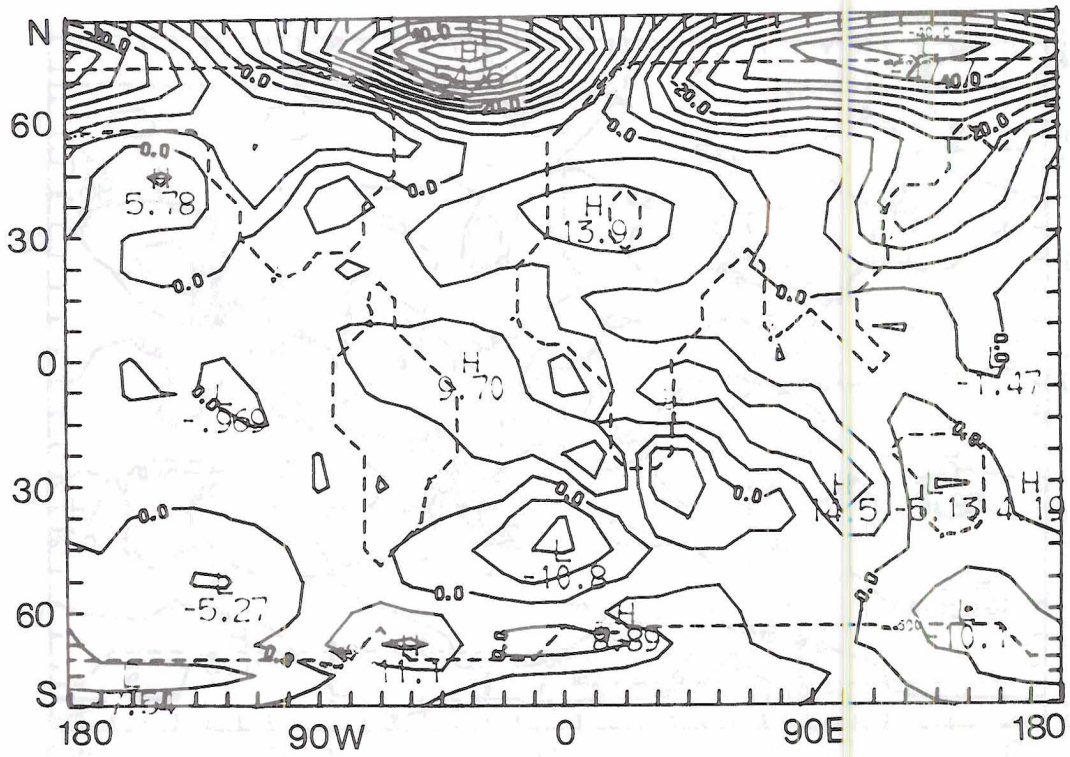

5.25 The mean sea level pressure difference (mb) between the anomaly (Experiment 4) and control run for February.

The differences in the transports and variances (Table 5.4a) indicate that the transport of temperature by the mean meridional circulation is generally southward, dominating the tropical and subtropical regions, whereas in the middle and higher latitudes the southward transport by the stationary eddies is a major influence. The transport of sensible heat by the transient eddies appears to increase poleward. The order of magnitude of the differences in the variances is larger than those calculated in the previous experiments. The variance of temperature resulting from stationary eddies is decreased in the middle and high latitudes, whereas that resulting from transient eddies is increased, especially in the subtropics and the middle latitudes.

The differences in the transport of the potential energy (Table 5.4b) by the mean meridional circulation show a northward component at all latitudes except high latitudes. These estimates indicate the enhancement of the Hadley circulation. The differences in the variances of the geopotential height resembles those of the temperature fields.

In comparison with Experiment 2 (SSTA in the equatorial Pacific), the pesent experiment has a similar locations of maxima and minima. The magnitude of the differences is larger in this experiment due to the larger anomaly amplitude used.

5.2.2 Thermal Tropospheric Anomalies over the Gulf of Bengal

In Experiment 5 the westward-propagating thermal anomaly is located over the Gulf of Bengal at latitude 7.7°N. The latitudinal width of the anomaly wave is nearly half that assumed over the equatorial Pacific (experiment 4). At the same time its lower boundary contains both land and ocean surfaces.

TABLE (5.4)

Experiment 4
Difference (Anomaly minus Control) in the
Zonal Average Variances and Transports

Table (5.4a)

Temperature

Latitude (North)	Eq.	7.7	15.3	23.0	30.6	38.3	45.9	53.6	61.3	68.9	76.5	84.1
Parameter												
Transport by Mean Meridional Circulation ($m\ sec^{-1}\ °C$)	1.079	-.6	-1.7	-1.7	-1.17	-.8	-.849	-.832	-.469	-.034	.273	.269
Transport by Stationary Eddies ($m\ sec^{-1}\ °C$)	.042	-.005	.166	.21	-.243	-.015	1.04	-.089	-3.4	-3.26	-.367	.222
Transport by Transient Eddies ($m\ sec^{-1}\ °C$)	-.017	-.06	-.06	-.07	-.07	-.016	-.038	-.24	-.3	-.294	-.7	-.73
Variances of Stationary Eddies $(°C)^2$	.61	.62	.8	1.1	.53	-1.2	-1.5	-1.8	-4.5	-2.2	3.4	1.9
Variances of Transient Eddies $(°C)^2$	.94	1.13	1.22	1.33	1.62	1.8	1.212	.18	-.02	.35	-.67	-2.48

Table (5.4b)

Geopotential

Latitude (North)	Eq.	7.7	15.3	23.0	30.6	38.3	45.9	53.6	61.3	68.9	76.5	84.1
Parameter												
Transport by Mean Meridional Circulation ($m^2 sec^{-1}$)	-171.6	236.1	462.5	453.4	318.3	198.7	144.5	115.8	64.4	-7.1	-52.4	-39.4
Transport by Stationary Eddies ($m^2 sec^{-1}$)	-.5	.98	.5	-1.6	.378	2.7	5.6	3.23	2.2	3.86	-4.4	-7.6
Transport by Transient Eddies ($m^2 sec^{-1}$)	-.1	.42	.5	-.08	-.021	.17	.31	.5	.287	-.32	.9	1.8
Variances of Stationary Eddies (10^2 m^2)	.3	.35	-.3	-.8	4.1	19.8	35.5	32.7	16.7	3.6	-2.9	-1.8
Variances of Transient Eddies (10^2 m^2)	5.1	5.5	5.8	6.2	7.0	6.3	.65	-5.1	-.5	11.4	16.3	12.6

The response in the 500 mb zonal velocity (Fig. 5.26a) is shown to be almost zonally symmetric. The subtropical jet stream is enhanced, with the maximum westerly component north of the anomaly region. The midlatitude westerlies are decreased in both the eastern and western hemispheres. The maximum differences take place in the extratropical latitudes, with a superimposed westerly component. In the Southern Hemisphere the easterlies in the tropical region and the subtropical westerlies are strengthened. The differences in the 500 mb meridional wind (Fig. 5.26b) show that the western parts of the continents have southward flow, whereas the eastern parts have northward flow. Again the maximum differences appear to be in the higher latitudes.

The differences in the 750 mb temperatures (Fig. 5.27a) show warm tropical and subtropical regions in the vicinity of the anomaly. Northern Hemisphere middle and extratropical latitudes are characterized by colder air over the continents, with the major cooling over northern Eurasia. The Southern Hemisphere does not show any large differences except for the warm pool south of the Indian Ocean. The 250 mb temperature differences (Fig. 5.27b) are mainly zonal in the two hemispheres with a thermal ridge in the equatorial region that extends to South Africa.

The differences in the 750 mb geopotential height (Fig. 5.28a) show high pressure areas to the west of the continents in the Northern Hemisphere for high latitudes. The eastern parts of the continents reveal low pressure anomalies of lesser magnitude. In the lower latitudes the anomalies induce two centers of low pressure towards their northwest and southwest. In the Southern Hemisphere the maximum differences appear as low pressure areas near Antarctica. The 250 mb

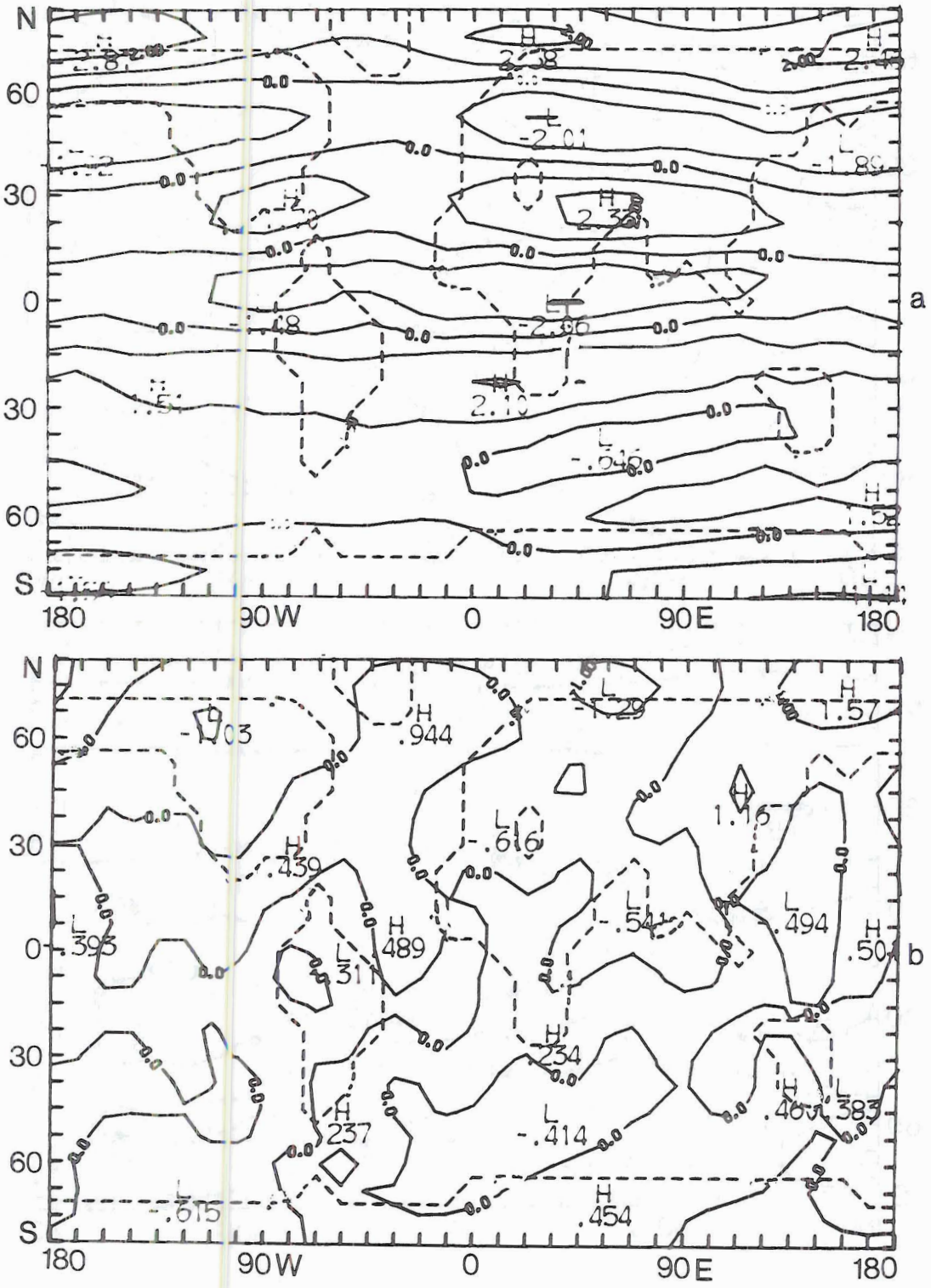

5.26 The horizontal wind difference (m sec^{-1}) at 500 mb between the anomaly (Experiment 5) and control run for February. a) zonal wind; b) meridional wind.

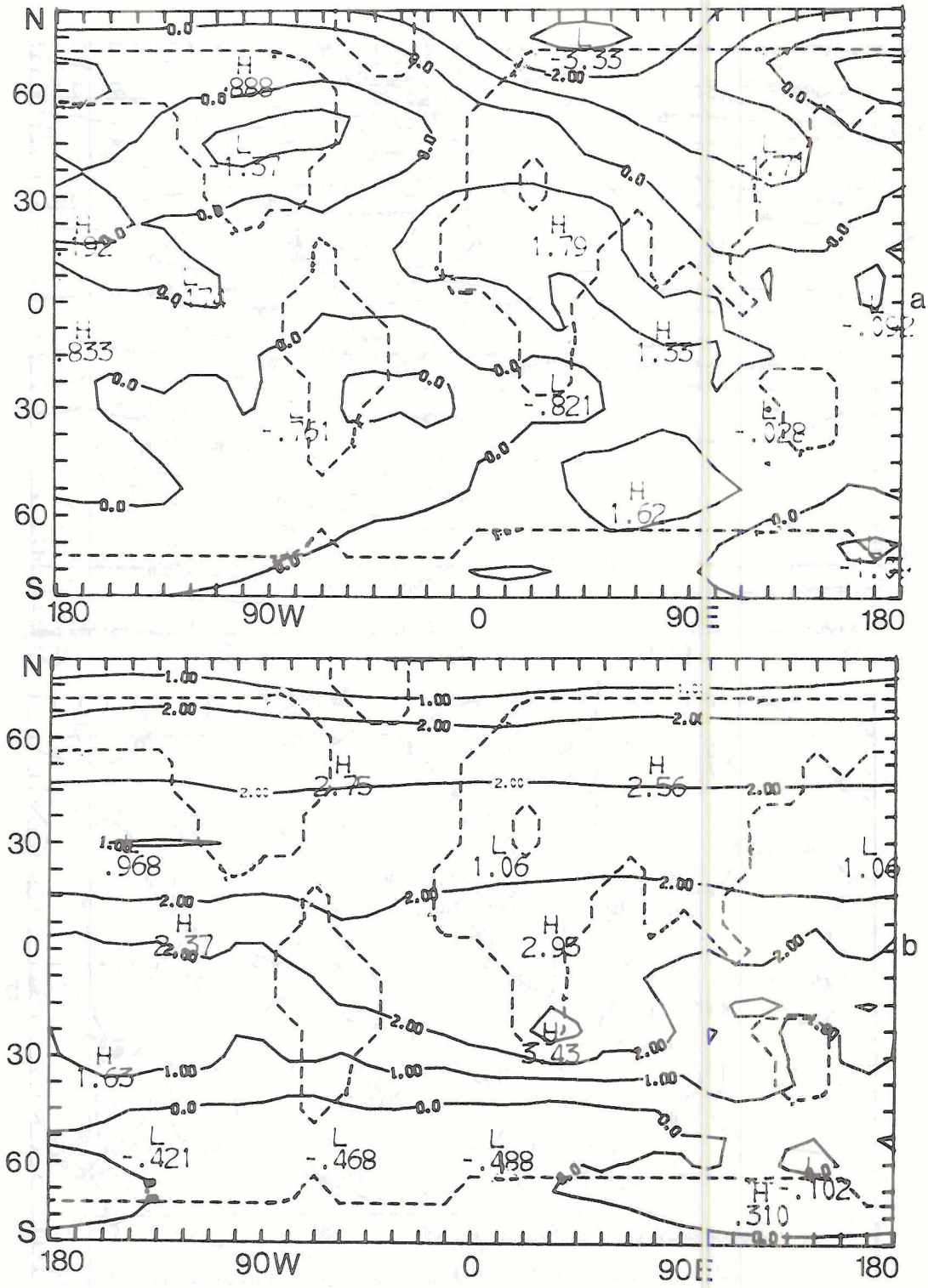

5.27 The temperature difference (°C) between the anomaly (Experiment 5) and control run for February. a) at 750 mb; b) at 250 mb.

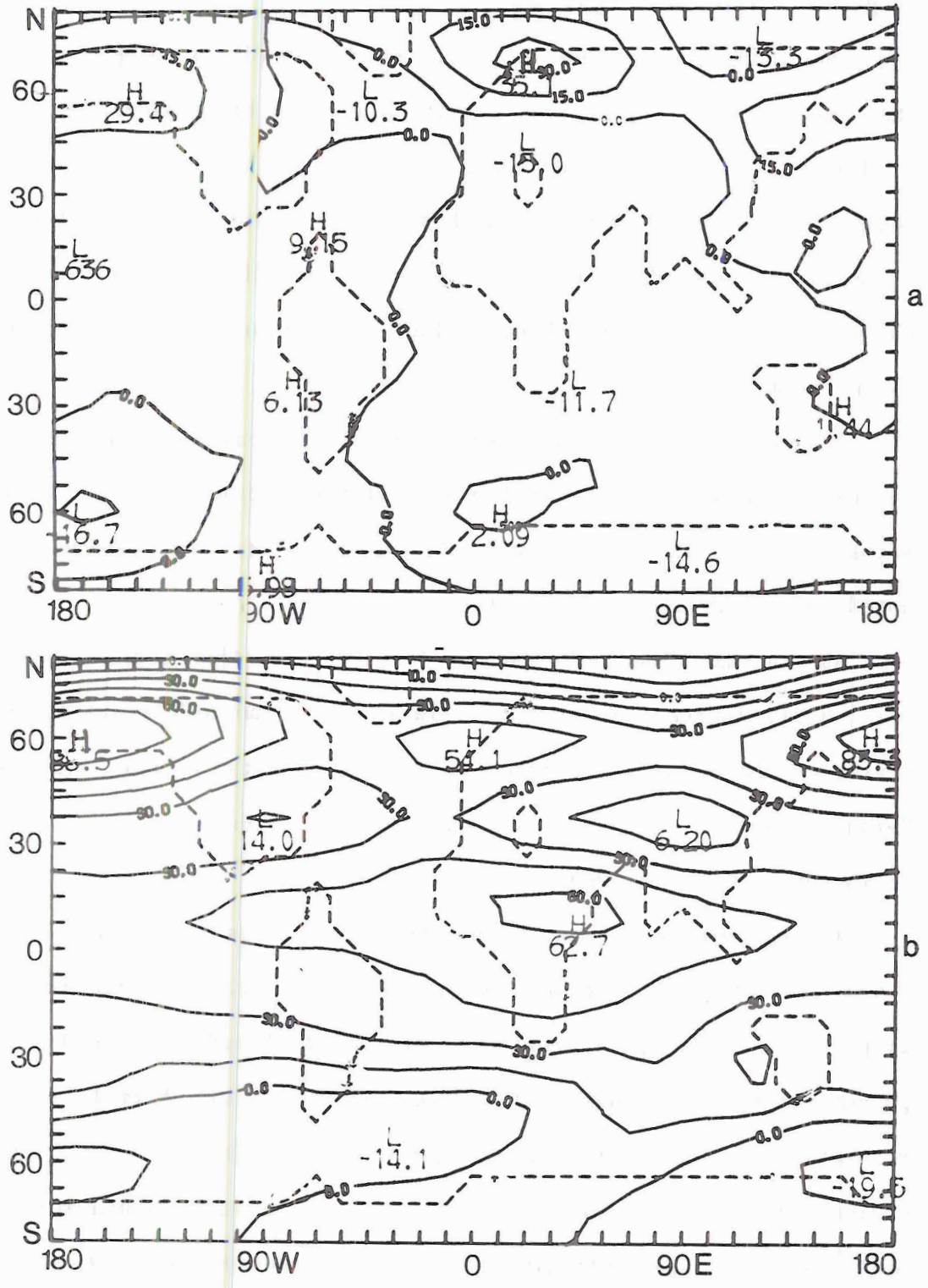

5.28 The geopotential height difference (m) between the anomaly (Experiment 5) and control run for February. a) at 750 mb; b) at 250 mb.

pattern (Fig. 5.28b) shows essentially the same sign in the differences as given by the lower layer.

The difference in the 500 mb pressure velocities (Fig. 5.29) show that the anomalies to the south of the Himalayas force ascending motions in the whole region. Induced subsidence is created in the adjacent regions in the subtropics of both hemispheres. The southerly flow which is initiated across the east-west extent of the Himalayas acts to force the vertical motion. The North Atlantic is characterized by an area of ascending motion.

The evaportion rate differences (Fig. 5.30) indicate that the major decrease of evaporation is in the area of the Indian Ocean, south of the anomaly. The continents have relatively smaller differences, as was noted in the previous experiments.

As in Experiment 4 the differences in the surface pressure (Fig. 5.31) increase towards high latitudes. The middle latitudes are characterized by high pressure over the continents, except over western Eurasia, where a trough of low pressure exists as a result of the warm anomalies. The Siberian high is well developed.

The differences in the temperature transports and variances (Table 5.5a) indicate that the mean meridional circulation dominates in the tropical and subtropical regions. It has northward and southward components to the south and north of the latitude of the thermal anomalies, respectively. In middle and extratropical latitudes, the stationary eddies have a relatively large influence, with mainly southward transport. At a certain latitudinal belt the differences in the variances of temperature resulting from the stationary and transient eddies have a similar sign. Both are negative in high latitudes. The variances

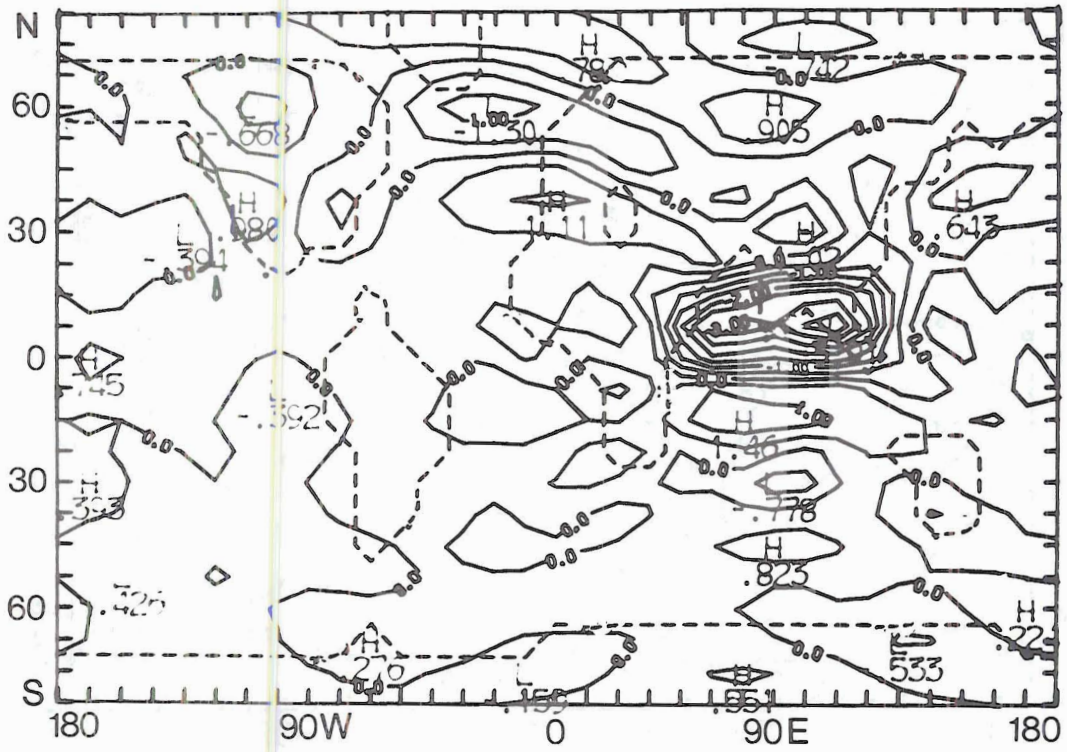

5.29 The vertical pressure velocity difference (10^{-4}mb sec^{-1}) at 500 mb between the anomaly (Experiment 5) and control run for February (negative values upward, positive values downward).

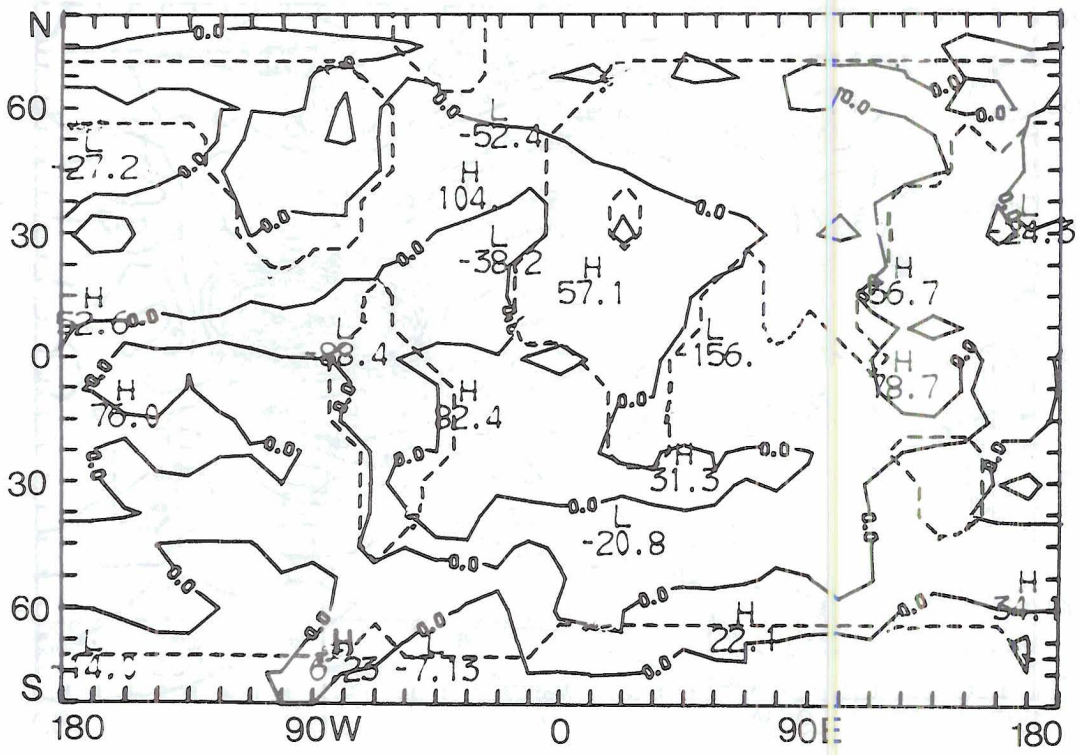

5.30 The surface evaporation rate difference (10^{-3} cm/day) between the anomaly (Experiment 5) and control run for February.

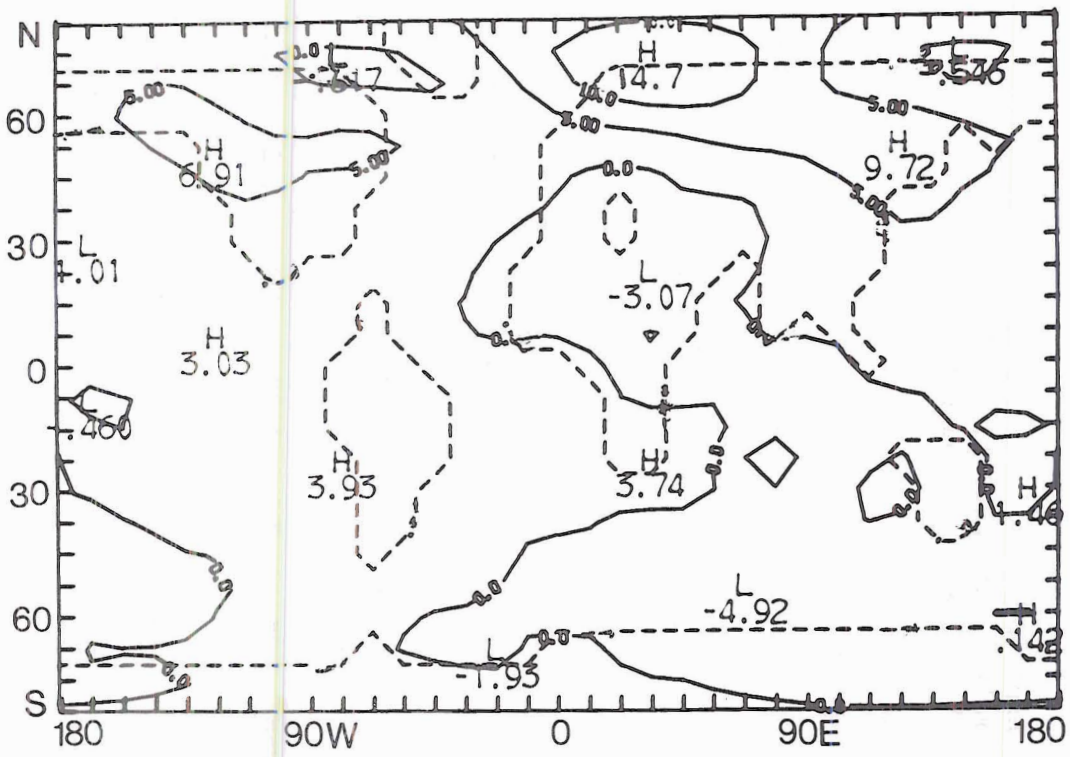

5.31 The mean sea level pressure difference (mb) between the anomaly (Experiment 5) and control run for February.

TABLE (5.5)

Experiment 5
Difference (Anomaly minus Control) in the
Zonal Average Variances and Transports

Table (5.5a)

Temperature

Latitude (North)	Eq.	7.7	15.3	23.0	30.6	38.3	45.9	53.6	61.3	68.9	76.5	84.1
Parameter												
Transport by Mean Meridional Circulation ($m\ sec^{-1}\ °C$)	1.8	.96	-.332	-1.08	-.755	.241	.82	.514	-.004	-.216	-.209	-.105
Transport by Stationary Eddies ($m\ sec^{-1}\ °C$)	.071	.103	-.05	-.233	-.334	-.441	-.314	.327	.658	-.337	-1.68	-1.4
Transport by Transient Eddies ($m\ sec^{-1}\ °C$)	.001	-.002	.006	0	-.028	-.029	-.037	-.148	-.277	-.368	-.578	-.494
Variances of Stationary Eddies $(°C)^2$	.132	.16	.214	.256	.38	.7	1.23	.936	1.23	3.47	3.11	.876
Variances of Transient Eddies $(°C)^2$	.347	.392	.4	.35	.25	.21	.21	.093	-.168	-.6	-.85	-.356

Table (5.5b)

Geopotential

Latitude (North)	Eq.	7.7	15.3	23.0	30.6	38.3	45.9	53.6	61.3	68.9	76.5	84.1
Parameter												
Transport by Mean Meridional Circulation ($m^2 sec^{-1}$)	-394.8	-155.1	130.2	260.8	176.4	5.1	-88.7	-59.7	22.9	74.3	68.2	31.8
Transport by Stationary Eddies ($m^2 sec^{-1}$)	.3	.7	1.3	.8	1.0	.569	-1.3	-.68	1.27	.39	-.375	.328
Transport by Transient Eddies ($m^2 sec^{-1}$)	.04	.096	.17	.086	-.05	-.08	-.06	.151	.193	.05	.259	.428
Variances of Stationary Eddies (10^2 m^2)	-.008	-.005	.07	1.1	3.1	1.8	-1.5	1.9	7.8	4.6	-2.4	-1.71
Variances of Transient Eddies (10^2 m^2)	1.7	1.9	2.1	2.	1.4	.7	.058	-.99	-1.4	.6	6.6	14.8

resulting from the stationary eddies show maxima in middle latitudes. The transient eddy activity is increased significantly in the latitudinal zones adjacent to the anomalies. This result reflects the effect of the Himalayas in enhancing transient eddies caused by the thermal anomalies.

The transport of potential energy (Table 5.5b) by the mean meridional circulation is northward with a maximum in the subtropical region north of the anomaly position. The transport is negative south of the anomaly. This result indicates that the Hadley circulation is generally enhanced as a result of the anomalies. The differences in the transports of potential energy by the stationary and transient eddies are of a lower magnitude. The differences in the variances of potential energy resulting from stationary waves are positive and have a maximum in the high latitudes. The transient eddy effects reveal two inversions, one in the subtropics north of the anomaly location and the other in the polar region.

5.3 "Memory" of Different Anomaly Patterns in the Atmosphere

It is difficult to estimate the way in which the atmosphere will "remember" certain anomalies after they are gone. The difficulty arises from the fact that the oceans in our model, which represent large reservoirs of energy, do not respond, or change as a result of the atmospheric circulation above them. However, we can still gain an idea about the way in which the atmosphere recognizes the effects of the anomalies by itself. A memory parameter is defined to show the geographic locations that display a sustained influence of the circulation caused by the anomalies. The analysis for this purpose is done in two phases using the March circulation (day 121-150). In the first phase

each experiment is conducted through March with the anomalies. In the second phase the experiment is repeated through the same period, but with a gradually decreasing anomalies. The removal of the anomalies is accomplished using an e-folding time of 5 days, which corresponds to the time over which the anomalies were introduced into the January circulation.

At a certain grid point $(_{ij})$, we define the variable $(X_{ij})_2$ to represent the March anomaly run. The same variable without anomalies is $(X_{ij})_{NA}$, whereas its value in the control run representing normal March is $(X_{ij})_1$.

The memory parameter at grid point $(_{ij})$ is given by

$$(Mo)_{ij} = \left| \frac{(X_{ij})_2 - (X_{ij})_{NA}}{(X_{ij})_2 - (X_{ij})_1} - 1 \right| \times 100. \qquad (5.8)$$

This parameter is calculated using the monthly average geopotential height of the 500 mb level at each grid point. In this way, the parameter shows a high value for those locations at which geopotential height is substantially changed by the anomalies as compared to the control run, while the geopotential height did not change much when the anomalies were removed. We are going to consider a significant memory to be above 90%, and it must cover a considerable continuous area, not just a single grid point.

We will first consider the cases representing the surface temperature anomalies (experiments 1 to 3). In experiment 1 when cold SSTA are located in the North Pacific, (Fig. 5.32a) the memory parameter shows large values over the eastern tropical Pacific. This is the area where the El Nino occurs. This result indicates that the atmosphere in this

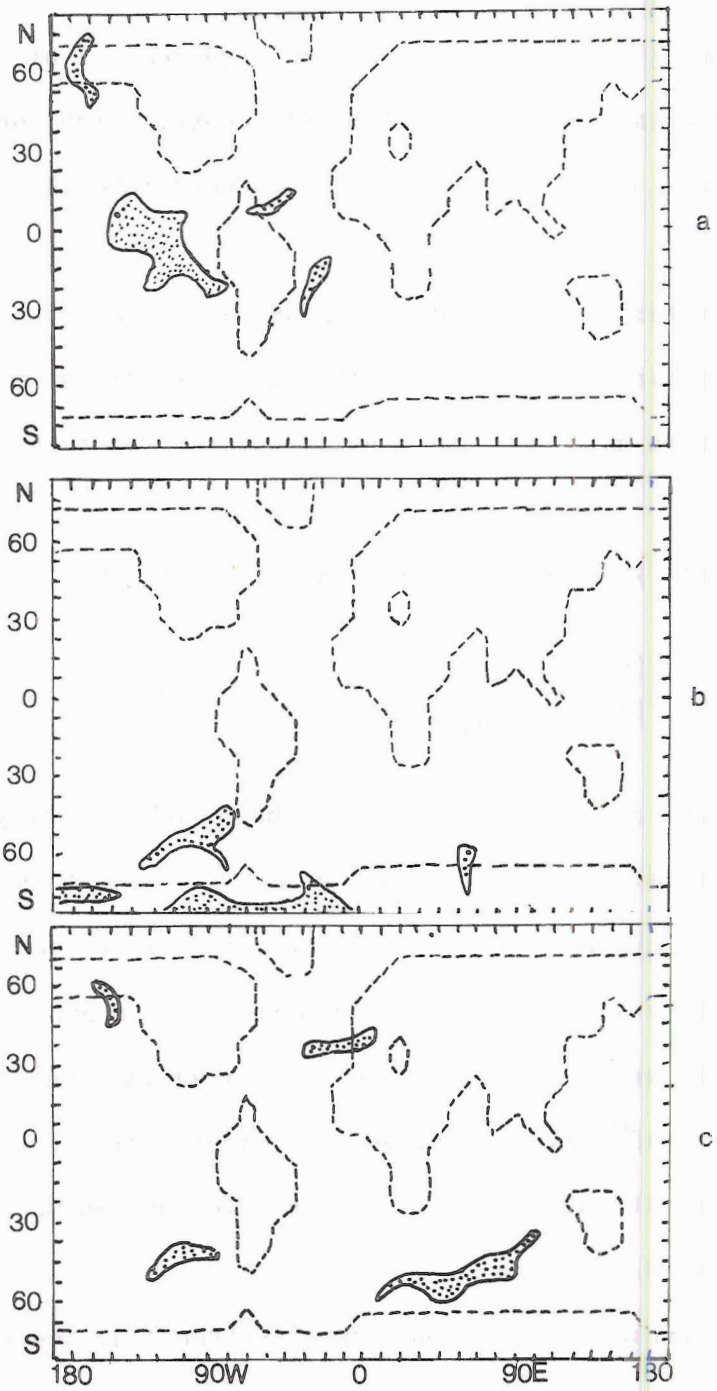

5.32 The memory parameter (%), shaded areas have memory > 90%. a) Experiment 1; b) Experiment 2; c) Experiment 3;

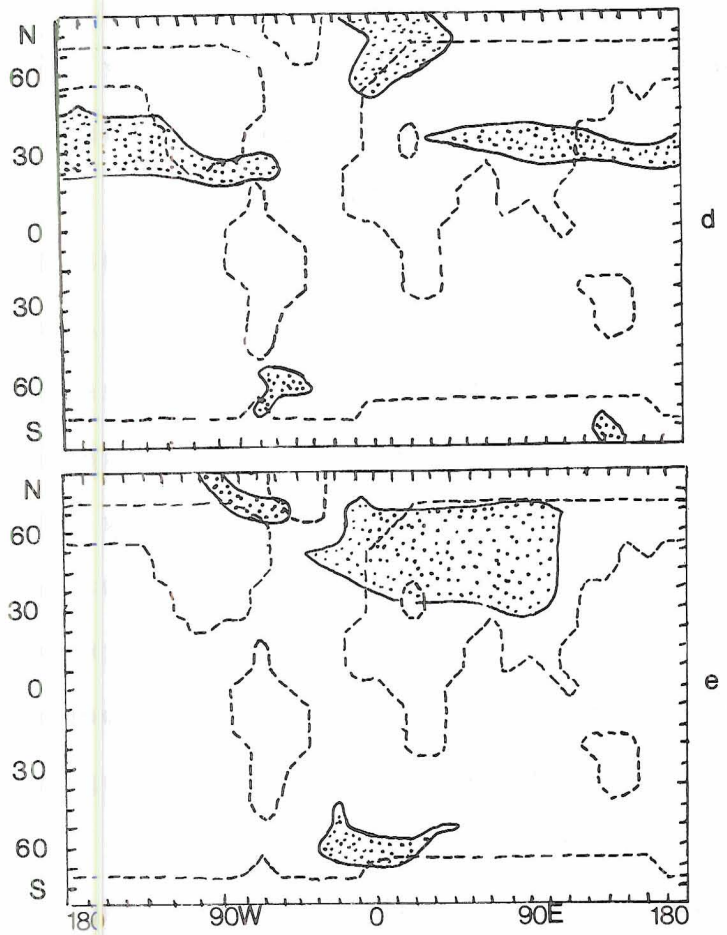

5.32 (cont.) The memory parameter (%), shaded areas have memory > 90%. d) Experiment 4; e) Experiment 5.

region could preserve the effect of the SSTA to their north for longer time periods than could other places over either the oceans or the continents. At the same time the differences in this region, are not large enough to cause a significant response of the atmosphere, as was discussed in section 5.1.1.

In Experiment 2, the SSTAs are located in the eastern tropical Pacific. The response of the atmosphere to these anomalies is of a direct nature and has a recognizable effect on the middle and extratropical latitudes. As Figure 5.32b shows, the effect of the anomaly is not retained in any region after it is removed, except in the polar latitudes of the Southern Hemisphere. The last case in this category is experiment 3, where a dual-type anomaly was located in the northern and equatorial Pacific. The memory of the atmosphere (Fig. 5.32c) seems to be improved relative to the previous case. Again there are small discrete areas of high memory in the Northern Hemisphere and a large area in the Southern Hemisphere. An area of large memory appears west of Canada in high latitudes, but it is not large enough to form an air mass with considerable impact on in the atmosphere.

The thermal anomalies in the middle troposphere (experiments 4 and 5) generally show a more continuous memory pattern (Fig. 5.32d,e), which spreads over large areas. We should remember the relatively large amplitude of the anomaly used in these experiments. In experiment 4, with the thermal heat source propagating in the troposphere of the equatorial Pacific, the maximum memory regions are spread over the subtropics north of the anomaly location, and in the middle latitudes. In Experiment 5 the thermal heat source is located along the Indian Ocean. The high memory appears to the north of the anomaly location in the middle latitudes of Eurasia.

5.4 Determination of the Noise Level

It is necessary to determine the noise level of the model-generated climatological statistics in order to judge the significance of the response calculated by the different experiments. The geographic distribution of the standard deviation of temperature and geopotential height is calculated using the control run and four runs with randomly perturbed initial conditions. The initial perturbations are imposed on the velocity and temperature fields at day 61 (first of January). Perturbed values have a zero average, with standard deviations equal to 1°C and 4 m sec^{-1} for the temperature and wind, respectively (Shukla and Bangaru, 1980). The model runs for January and February, and their standard deviations are calculated using the 30 day averages of the five runs with their different anomaly fields. Analyses of the standard deviations of the temperature and geopotential height fields at 750 mb (Fig. 5.33a,b) show that the variability is mostly in the Northern Hemisphere middle and high latitudes. This is a result of the enhanced transient eddies during winter in these regions. The values decrease equatorward in both hemispheres. The maximum variability of temperature is between 50°N and 70°N to the west of Canada and the east of Asia. This feature is in qualitative agreement with a calculation done by Crutcher and Meserve (1970) for the 850 mb temperatures using data from January of 14 years. The standard deviation of the geopotential height displays the same features as that of the temperature field, but shifted by about 90° to the east. This shift is a result of the baroclinic nature of the disturbances occupying these latitudes.

As was discussed in Chapter 4, a significant atmospheric response, with confidence above 95%, requires the significance ratio to be ≥ 4. A

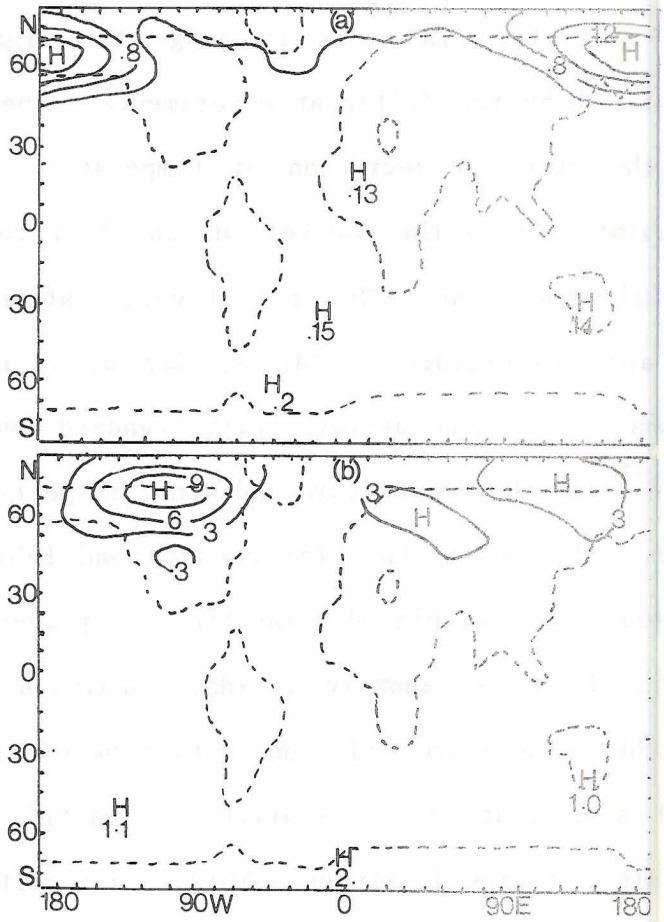

5.33 Geographical distribution of the standard deviations $(St)_{ij}$ from five Februaries (the normal February and four random perturbations of the normal) simulated by the model . a) 750 mb temperature (°C) b) 750 mb geopotential (m).

comparison between the standard deviation values and the resulting differences from the previous experiments shows that this condition is fulfilled for most of the maxima and minima. This guarantees that the differences which result from thermal anomalies exceed (by at least four times) the differences caused by the random variability of the model itself.

6. SUMMARY AND CONCLUSIONS

We intended to investigate the atmospheric response to equatorial and midlatitude thermal anomalies in the form of SSTA's or diabatic heating anomalies in the middle troposphere. Analyses of observational data suggest a possible response of the atmosphere to the Pacific SSTA's in the equatorial and middle latitudes (e.g., Bjerknes, 1969; Namias, 1976, 1980). Horel and Wallace (1981) showed the possible connections between seven warm episodes in the sea surface temperature of the equatorial Pacific and the 700 mb geopotential in the Northern Hemisphere. Linear and nonlinear models were developed to test the possible teleconnections between the atmospheric variables at different latitudes (e.g. Rowntree, 1972; Egger, 1977; Chervin et al., 1976; Chervin et al., 1980; Simpson and Downey, 1975). Most of the numerical studies confirmed the response of the atmosphere to tropical SSTA's. Contrary to the observational evidence, most experiments show no significant response of the atmosphere in middle latitudes, to a midlatitude SSTA of observed amplitude. In some cases super-anomalies were used ($\pm$ 12°C) to obtain a significant atmospheric response.

Hoskins and Karoly (1981) used a linearized steady-state five layer baroclinic model to study the response of the atmosphere to thermal and orographic forcing. The results for the subtropical thermal forcing show the long waves are set up poleward and eastward of the thermal source, whereas shorter wavelengths are trapped equatorward of the jet.

The response is generally less for midlatitude thermal forcing than for the case of subtropical forcing. However, the response is crucially dependent on the vertical distribution of the source.

Since the atmosphere is highly nonlinear, it is difficult to predict the correct positions of the geopotential height extremes using a linear model. For this purpose, a two-level, nonlinear, quasi-geostrophic (linear balance) global model is developed. The dynamic structure of the model is basically that of Lorenz (1960). A moisture budget equation is used in the lower layer. In the horizontal domain a rhomboidal spectral truncation is assumed, using the associated Legendre functions. Pressure is used as a vertical coordinate. The finite difference method is used for vertical approximations.

The forcing and dissipation mechanisms adopted in the model are:

1) Diabatic heating due to short and longwave radiation. The solar energy is specified assuming an average zenith angle.

2) Sensible heat flux between the surface and the lower layer for both land and sea areas.

3) Release of latent heat of condensation in the lower layer in the case of near super-saturation (85%). Convective adjustment is used to adapt the temperature profile in order to avoid supercritical lapse rates.

4) Mechanical forcing by orography as a lower boundary (1000 mb) condition on vertical pressure velocity.

5) Surface friction and friction between the two layers.

6) The sea surface temperature is specified over the oceans assuming the January mean values. A steady state surface energy

equilibrium is assumed over land and ice areas in order to calculate the surface temperature.

The explicit centered scheme (Leap-frog) is used for time integration. For computational stability the frictional and diffusion terms are integrated from the previous time step. A time filter is used to couple odd and even time steps. The time step used is 2 hours (120 minutes). For calculation of one month (30 days) the model requires about 50 seconds on the CRAY-1 machine of the National Center for Atmospheric Research (NCAR).

Integrations are performed to simulate the climate of January, February and March. The model starts from a hypothetical atmosphere at rest with a constant lapse rate. Integration is carried out for 60 days assuming constant insolation (first of January). From day 61 to day 150, the January, February and March simulations are carried on with a daily change of insolation. This period represents the control run for the three months. To deduce the inherent variability of the model (the noise), the control run is repeated four times with different initial random wind and temperature perturbations. The geographic distribution of the standard deviations for the temperature and geopotential height fields are calculated using the five runs.

Comparison of the January climate of the model with the observed circulation shows that the model can simulate the main features of the large scale circulation. The transient eddies are underestimated by the model. This limitation is due to several simplifications in designing the model, such as the low order truncation, the zonally averaged forcing of solar radiation and the time filter operator. In spite of these deficiencies the model is useful for climate sensitivity studies.

Experiments were designed to examine the response of the atmosphere to regional anomalies in the thermal forcing either by a lower boundary SSTA or by a diabatic heating rate existing in the middle troposphere. The main branches of the investigations are:

1) To determine the way in which the atmosphere responds to each anomaly at different locations. For example, how does the atmosphere respond to a cold SSTA in the North Pacific or warm SSTA in the equatorial eastern Pacific, or to both anomalies existing at the same time?

2) To estimate the response of the atmosphere to mid-tropospheric thermal anomalies in the tropics.

3) To determine the atmospheric memory for the thermal anomalies at different locations. In other words, if the thermal anomalies were removed there would be different recognition of their past effects by the atmosphere.

Five experiments are used to test the above arguments. Super-anomalies are assumed in experiment 1 (minimum -12°C) to investigate the effect of SSTA's in the Northern Pacific. Experiment 2 uses the usually observed amplitudes of SSTA to demonstrate the effect of El Nino in the equatorial eastern Pacific. Experiment 3 represents the distributions of both of these anomalies acting together. However, the super SSTA in the Northern Pacific is changed to approximately observed values (minimum -4°C). Experiments 4 and 5 simulate the effect of middle-tropospheric anomalies resulting from the release of latent heat in a propagating easterly wave. In experiment 4 the anomaly wave is propagating through the width of the equatorial Pacific, whereas the wave is located in the Indian Ocean south of the Himalayas in experiment 5.

Experiments with anomalies use the results of day 60 of the control run as an initial state. The effects of the anomalies in each region are imposed gradually using a 5 day e-folding time. The insolation is changed daily and the model is run for January, February and March. To examine the way in which the model "remembers" each type of anomaly, the March run (days 120-150) is repeated after gradually deleting the thermal anomalies.

The main conclusions of the model development and the experiments can be summarized in the following way:

1) The nonlinear quasi-geostrophic (linear balance) model is useful for studying the response of the atmosphere in middle and high latitudes to tropical thermal anomalies. As shown in experiment 2 (SSTA in the tropical East Pacific), the results agree with many primitive equation models examining the same type of anomalies.

2) Nonlinear interactions are important mechanisms in producing the correct phase of the different variables.

3) The mountains have an important influence in modifying the atmospheric circulation caused by the thermal anomalies.

4) Warm SSTA's in the equatorial Pacific induce a mid-tropospheric thermal anomaly. The corresponding response of the atmosphere does not support the linear theory argument by Hoskins and Karoly (1981). This anomaly pattern is not capable of producing the tropospheric geopotential height anomaly suggested by Horel and Wallace (1981).

5) Both warm SSTA's in the tropical Pacific and cold SSTA's in the North Pacific, acting together (experiment 3), are essential in

producing the middle- and upper-tropospheric geopotential pattern suggested by Hoskins and Karoly (1981) and described by Horel and Wallace (1981), which is associated with the negative phase of the Southern Oscillation. The SSTA's in these regions enhance the thermal wind over the subtropical Pacific. With an anomalous easterly component over the North American continent, the northern and southern parts of the United States are under the influence of anticyclonic and cyclonic horizontal wind shears, respectively.

6) The variances of temperature resulting from the stationary eddies were increased in middle latitudes in response to the SSTA's in the north and equatorial Pacific. The variances resulting from transient eddies increased in the case of equatorial SSTA's alone. These results suggest that the cold SSTA's in the North Pacific favor an enhancement of semi-permanent features like blocking, whereas the warm SSTA's in the equatorial Pacific enhance the transient components in middle and high latitudes.

7) Either cold SSTA's in the middle latitudes or warm SSTA's in the equatorial Pacific are capable of causing a local increase of the subtropical jet stream. The north-south temperature gradient produces a westerly thermal wind component in the lower troposphere.

8) The middle tropospheric thermal anomalies have a greater effect on the atmosphere (both local and remote) than the SSTA's.

9) The way in which the atmosphere "remembers" the effects of the anomalies after they have been removed depends on the horizontal and vertical locations of the anomalies. The mid-tropospheric thermal anomalies seem to have a more extended and organized type

of memory; most of the "high memory" areas appear to be in the subtropical and middle latitude regions of the Northern Hemisphere. 10) The SSTA gradient used in experiment 3 (6°C to 8°C per 40° latitude) seems reasonable within the capabilities of current climate monitoring e.g. from satellites and ships.

REFERENCES

Angell, J.K., 1981: Comparison of variations in atmospheric quantities with sea surface temperature variations in the equatorial eastern Pacific. Mon. Wea. Rev., 109, 230-243.

Ashe, S., 1978: The seasonal-mean planetary waves--an introduction. The general circulation, theory, modeling and observations. NCAR/CQ-6+1978-ASP.

Ashe, S., 1979: A nonlinear model of the time-average axially asymmetric flow induced by topography and diabatic heating. J. Atmos. Sci., 36, 109-126.

Asselin, R., 1972: Frequency filter for time integrations. Mon. Wea. Rev., 100, 487-490.

Bates, J.R., 1977: Dynamics of stationary ultra-long waves in middle latitudes. Quart. J. R. Met. Soc., 103, 397-430.

Berkufsky, L., and E.A. Bertoni, 1955: Mean topographic charts for the entire earth. Bull. Amer. Met. Soc., 36, 350-354.

Berlage, H.P., 1966: The Southern Oscillation and world weather. Mededel Verhandel, 88, 152 pp.

Bjerknes, J., 1969: Atmospheric teleconnection from the equatorial Pacific. Mon. Wea. Rev., 97, 163-172.

Boer, G.J., and K. Higuchi, 1980: A study of climatic variability. Mon. Wea. Rev., 108, 1326-1332.

Bolton, D., 1980: The computation of equivalent potential temperature. Mon. Wea. Rev., 108, 1046-1053.

Bourke, W., B. McAvarey, K. Puri, and R. Thuring, 1977: Global modeling of amtospheric flow by spectral methods. Methods in Compt. Phys., 17, 267-324.

Burger, A.P., and H.A. Riphagen, 1979: The lower boundary condition and energy consistency in primitive and filtered models. J. Atmos. Sci., 36, 1436-1449.

Cayan, D.R., 1980: Large-scale relationships between sea surface temperature and surface air temperature. Mon. Wea. Rev., 108, 1293-1301.

Charney, J.G., 1959: On the theory of the general circulation of the atmosphere. The Atmosphere and the sea in motion, New York, The Rockefeller Institute Press, 135-162.

Charney, J.G., and J.G. DeVore, 1979: Multiple flow equilibria in the atmosphere and blocking. J. Atmos. Sci., 36, 1205-1216.

Charney, J.G., J. Shukla, and K.C. Mo, 1981: Comparison of a barotropic blocking theory with observations. J. Atmos. Sci., 38, 762-779.

Chervin, R.M., 1980: On the simulation of climate and climate change with general circulation models. J. Atmos. Sci., 37, 1903-1913.

Chervin, R.M., J.E. Kutzbach, D.D. Houghton, and R.G. Gallimore, 1980: Response of the NCAR general circulation model to prescribed changes in ocean surface temperature. Part II: Midlatitude and subtropical changes. J. Atmos. Sci., 37, 308-332.

Chervin, R.M., and S.H. Schneider, 1976: A study of the response of NCAR GCM climatological statistics to random perturbations: Estimating noise levels. J. Atmos. Sci., 33, 391-404.

Chervin, R.M., W.H. Washington, and S.H. Schneider, 1976: Testing the statistical significance of the response of the NCAR general circulation model to North Pacific Ocean surface temperature anomalies. J. Atmos. Sci., 33, 413-423.

Chiu, W., A. Lo, D.H. Weidler, and D. Fulker, 1981: A study of the possible statistical relationship between the tropical Pacific Sea surface temperature and atmospheric circulation. Mon. Wea. Rev., 109, 1013-1020.

Corby, G.A., A. Gilchrist, and P.R. Rowntree, 1977: United Kingdom Meteorological office five-level general circulation model. Methods in Compt. Phys., 17, 67-110.

Crutcher, H.L. and J.M. Meserve, 1970: Selected level heights, temperatures and dew points for the Northern Hemisphere. NAVAIR 50-IC-52 Rev., Naval Weather Service Command, Washington, D.C.

Curran, R.J., and G. Ohring, 1981: The effects of surface evaporation parameterizations on climate sensitivity to solar constant variations. J. Atmos. Sci., 38, 931-938.

Dole, R.M., 1978: The objective representation of blocking patterns. The General Circulation: theory, modeling and observations. NCAR/CQ-6+1978-ASP, 406-426.

Edmon, H.J., 1980: A study of the general circulation over the Northern Hemisphere during winters of 1976-77 and 1977-78. Mon. Wea. Rev., 108, 1538-1553.

Egger, J., 1977: On the linear theory of the atmospheric response to sea surface temperature anomalies. J. Atmos. Sci., 34, 603-614.

Egger, J., G. Meyers, and P.B. Wright, 1981: Pressure, wind and cloudiness in the tropical Pacific related to the southern oscillation. Mon. Wea. Rev., 109, 1139-1149.

Eliassen, E., and B. Machenhaur, 1969: On the observed large-scale atmospheric wave motions. Tellus, 21, 149-165.

Frederiksen, J.S., and B.L. Sawford, 1981: Topographic waves in nonlinear and linear spherical barotropic models. J. Atmos. Sci., 38, 69-86.

Fritz, S., 1982: Northern Hemisphere 700 mb heights and Pacific Ocean temperatures for winter months. Mon. Wea. Rev., 110, 18-25.

Gates, W.L., 1975: The January global climate simulated by a two-level general circulation model: A comparison with observations. J. Atmos. Sci., 32, 449-477.

Gates, W.L., and M.E. Schlesinger, 1977: Numerical simulation of the January and July global climate with a two-level atmospheric model. J. Atmos. Sci., 34, 36-76.

Gill, A.E., 1980: Some simple solutions for heat induced tropical circulation. Quart. J. R. Met. Soc., 106, 447-462.

Goody, R., 1980: Polar process and world climate (A brief overview). Mon. Wea. Rev., 108, 1935-1942.

Gruber, A., 1972: Fluctuations in the position of the ITCZ in the Atlantic and Pacific Oceans. J. Atmos. Sci., 29, 193-197.

Haltiner, G.J., 1971: Numerical Weather Prediction. John Wiley & Sons, Inc., 317 pp.

Haltiner, G.J., and R.T. Williams, 1980: Numerical Prediction and Dynamic Meteorology. John Wiley & Sons, Inc., 477 pp.

Harold, J.E., Jr., 1980: A study of the general circulation over the Northern Hemisphere during the winters of 1976-77 and 1977-78. Mon. Wea. Rev., 108, 1538-1553.

Hart, J.E., 1979: Barotropic quasi-geostrophic flow over an isotropic mountains. J. Atmos. Sci., 36, 1736-1746.

Hastenrath, S., 1976: Variations in low-latitude circulation and extreme climatic events in the tropical Americas. J. Atmos. Sci., 33, 202-215.

Hastenrath, S., and L. Heller, 1977: Dynamics of climatic hazards in Northeast Brazil. Quart. J. Roy. Meteor. Soc., 103, 77-92.

Held, I.M., D.L. Linder, and M.J. Suarez, 1981: Climate sensitivity: Results from dynamic and diffusive models. J. Atmos. Sci., 38, 1911-1927.

Held, I.M., and M. Suarez, 1978a: A two level primitive equation atmospheric model designed for climate sensitivity experiments. J. Atmos. Sci., 35, 206-228.

Held, I.M., and M. Suarez, 1978b: The tropospheric lapse rate and climatic sensitivity: Experiments with a two-level atmospheric model. J. Atmos. Sci., 35, 2083-2098.

Herman, G.F., 1981: Cloud-radiation experiments conducted with GLAS general circulation models clouds in climate: Modeling and satellite observational studies. Report Workshop, NASA, 88-92.

Holloway, J.L., and S. Manabe, 1971: Simulation of climate by a global general circulation model. Mon. Wea. Rev., 99, 335-370.

Holton, J.R., 1975: The dynamic meteorology of the stratosphere and mesosphere. Met. Mono., 37, 216 pp.

Horel, J.D., and J.M. Wallace, 1981: Planetary-scale atmospheric phenomena associated with the southern oscillation. Mon. Wea. Rev., 109, 813-829.

Hoskins, B.J., and D.J. Karoly, 1981: The steady linear response of a spherical atmosphere to thermal and orographic forcing. J. Atmos. Sci., 38, 1179-1196.

Hoskins, B.J., and A.J. Simmons, 1974: The development of spectral models in the U.K. Universities atmospheric modelling group. The GARP programme on numerical experimentation. Report No. 7, 94-99.

Houghton, D.D., J.E. Kutzbach, M. McClintock, and D. Suchman, 1974: Response of a general circulation model to a sea temperature perturbation. J. Atmos. Sci., 31, 857-868.

Julian, P.R., and R.M. Chervin, 1978: A study of the southern oscillation and Walker circulation phenomenon. Mon. Wea. Rev., 106, 1433-1451.

Kikuchi, Y., 1969: Numerical simulation of the blocking process. J. Met. Soc. Japan, 47, 29-54.

Kikuchi, Y., 1979: The influence of orography and land-sea distribution on winter circulation. Pap. Meteor. Geophys., 30, 1-32.

Kraus, E.B., 1972: Atmospheric-ocean interaction oxford. Meteor. Mono., Clarendon Press, Oxford.

Kraus, E.B., 1977: Subtropical droughts and cross-equatorial energy transports. Mon. Wea. Rev., 105, 1009-1018.

Kraus, E.B., and E.N. Lorenz, 1966: Numerical experiments with large-scale seasonal forcing. J. Atmos. Sci., 23, 3-23.

Kubota, I., 1972: Calculation of seasonal variation in the lower tropospheric temperature with heat budget equations. J. Met. Soc. of Japan, 50, 18-35.

Kutzbach, J.E., 1970: Large-scale features of monthly mean Northern Hemisphere anomaly maps of sea-level pressure. Mon. Wea. Rev., 98, 708-710.

Kutzbach, J.E., R.M. Chervin and D.H. Houghton, 1977: Response of the NCAR general circulation model to prescribed changes in ocean surface temperature, Part I: Mid-latitude changes.

Lau, K.W., 1979: A numerical study of tropical large scale air-sea interaction. J. Atmos. Sci., 36, 1467-1489.

Lau, K.W., 1981: Oscillations in a simple equatorial climate system. J. Atmos. Sci., 38, 235-247.

Leith, C.E., 1973: The standard error of time-average estimates of climatic means. J. of Appl. Met., 12, 1066-1069.

Lindzen, R.S., and B. Farrell, 1980: The role of polar regions in global climate, and a new parameterization of global heat transport. Mon. Wea. Rev., 108, 2064-2079.

Lorenz, E., 1951: Seasonal and irregular variations of the Northern Hemispgere sea-level pressure profile, J. Meteor., 8, 52-59.

Lorenz, E., 1955: Available potential energy and the maintenance of the general circulation. Tellus, 7, 157-167.

Lorenz, E., 1960: Energy and numerical weather prediction. Tellus, 12, 364-373.

Lorenz, E., 1961: Simplified dynamic equations applied to the rotating-basin experiments. J. Atmos. Sci., 19, 39-51.

Lorenz, E., 1968: Climatic determinism. Met. Mono., 8, 1-3.

Machenhauer, B., 1974: On the present state of spectral methods in numerical integrations of global atmospheric models. The GARP programming on numerical experimentation, Report No. 7, 1-21.

Machenhauer, B., and E. Rasmussen, 1972: On the integration of the spectral hydrodynamical equations by a transform method. Univ. of Copenhagen, Rpt. No. 3, 44 pp.

Manabe, S., D.G. Hahn, and J.L. Holloway, 1974: The seasonal variation of the tropical circulation as simulated by a global model of the atmosphere. J. Atmos. Sci., 31, 43-83.

Manabe, S., J. Smagorinsky, and R.F. Strickler, 1965: Simulated climatology of a general circulation model with a hydrologic cycle. Mon. Wea. Rev., 93, 769-798.

Milankivitch, M., 1941: Kanon der Erdbestrahlung und seine Anwendung auf des Eiszeitproblem. Royal Serbian Academy, Belgrade.

Namias, J., 1969: Seasonal interactions between the North Pacific Ocean and the atmosphere during the 1960's. Mon. Wea. Rev., 97, 173-192.

Namias, J., 1973: Thermal communication between the sea surface and the lower troposphere. J. Phys. Oceanogr., 3, 373-378.

Namias, J., 1976: Negative ocean-air feedback systems over the North Pacific in the transition from warm to cold seasons. Mon. Wea. Rev., 104, 1107-1121.

Namias, J., 1980: Causes of some extreme northern hemisphere climatic anomalies from summer 1978 through the subsequent winter. Mon. Wea. Rev., 108, 1333-1346.

Namias, J., 1981: Large-scale air-sea interactions and short period climatic fluctuations. Science, 214, 869-876.

Newell, R.E., J.W. Kidson, D.G. Vincent, and G.J. Boer, 1972: The general circulation of the tropical atmosphere and interactions with extratropical latitudes., Vol. 1., MIT Publisher Press, XIII, 258 pp.

Oort, A.H., and E.M. Rasmusson, 1971: Atmospheric circulation statistics. NOAA Professional Paper No. 5., 323 pp.

Opsteegh, J.D., and H.M. Van Den Dool, 1980: Seasonal differences in the stationary response of a linearized primitive equation model: prospects for long-range weather forecasting. J. Atmos. Sci., 37, 2169-2185.

Orszag, S.A., 1970: Transform method for the calculation of vector-coupled sums: Application to the spectral form of the vorticity equation. J. Atmos. Sci., 27, 890-895.

Pfeffer, R.L., 1981: Wave-mean flow interactions in the atmosphere. J. Atmos. Sci., 38, 1340-1359.

Phillips, N.A., 1956: The general circulation of the atmosphere: a numerical experiment. Quart. J. R. Met. Soc., 82, 123-164.

Phillips, N.A., 1959: An example of non-linear computational instability. The atmosphere and the sea in motion, New York, The Rockefeller Institute Press, 501-504.

Phillips, N.A., 1963: Geostrophic motion. Rev. Geophys., 1, 123-176.

Posey, J.W., and P.F. Clapp, 1964: Global distribution of normal surface albedo. Geofisica Internacional, 4, 33-43.

Potter, G.L., H.W. Ellsaesser, M.C. MacCracken, and C.S. Mitchell, 1981: Climate change and cloud feedback: The possible radiative effects of latitudinal redistribution. J. Atmos. Sci., 38, 489-493.

Puri, K., and W. Bourke, 1974: Implications of horizontal resolution in spectral model integrations. Mon. Wea. Rev., 102, 333-347.

Ramage, C.S., 1975: Preliminary discussion of the 1972-73 El Nino. Bull. Amer. Meteor. Soc., 56, 234-242.

Ramage, C.S., 1977: Sea surface temperature and local weather. Mon. Wea. Rev., 105, 540-544.

Ramage, C.S., and A.M. Hori, 1981: Meteorological aspects of El-Nino. Mon. Wea. Rev., 109, 1827-1835.

Ramage, C.S., and T. Murakami, 1973: Comment on the paper by R.P. Rowntree: "The influence of tropical east Pacific Ocean temperatures on the atmosphere". Quart. J. Roy. Meteor. Soc., 99, 393-394.

Reiter, E.R., 1978: Long-term wind variability in the tropical Pacific, its possible causes and effects. Mon. Wea. Rev., 106, 324-330.

Reiter, E.R., 1981: Surges of tropical Pacific rainfall and teleconnections with extratropical circulation patterns. To be published in the proceedings of the third Scientific Assemble IAMAP held 17-28 Aug. 1981, Oxford.

Reiter, E.R., and D. Westhoff, 1981: A planetary wave climatology. J. Atmos. Sci., 38, 732-750.

Roads, J.O., 1978: Numerical experiments on the climatic sensitivity of an atmospheric hydrologic cycle. J. Atmos. Sci., 35, 753-773.

Roads, J.O., 1980: Stable near-resonant states forced by orography in a simple baroclinic model. J. Atmos. Sci., 37, 2381-2395.

Rogers, J.G., 1981: Spatial variability of seasonal sea level pressure and 500 mb height anomalies. Mon. Wea. Rev., 109, 2093-2106.

Rowntree, P.R., 1972: The influence of tropical east Pacific Ocean temperatures on the atmosphere. Quart. J. Roy. Met. Soc., 98, 290-321.

Rowntree, P.R., 1976a: Tropical forcing of atmospheric motions in a numerical model. Quart. J. Roy. Met. Soc., 102, 583-605.

Rowntree, P.R., 1976b: Response of the atmosphere to a tropical Atlantic Ocean temperature anomaly. Quart. J. Roy. Met. Soc., 102, 607-625.

Rowntree, P.R., 1979: The effects of changes in ocean temperature on the atmosphere. Dyn. Atmos. Oceans, 3, 373-390.

Salmon, R., and M.C. Hendershott, 1976: Large scale air-sea interactions with a simple general circulation model. Tellus, 18, 228-242.

Saltzman, B., 1957: Equations governing the energetics of the larger scales of atmospheric turbulance in the domain of wave number. J. Met., 14, 513-523.

Saltzman, B., 1970: Large-scale atmospheric energetics in the wave-number domain. Rev. of Geophys. and Space Sci., 8, 289-302.

Sankar-Rao, M., 1965: Continental elevation influence on the stationary harmonics of the atmospheric motion. Pure Appl. Geophys., 60, 141-159.

Sankar-Rao, and B. Saltzman, 1969: On a steady theory of global monsoons. Tellus, 21, 308-330.

Schneider, S.H., and R.E. Dickinson, 1974: Climate modelling. Rev. Geophys. Space Phys., 12, 447-493.

Sela, J.G., 1980: Spectral modeling at the national meteorological center. Mon. Wea. Rev., 108, 1279-1292.

Sellers, W.D., 1976: A two dimensional global climatic model. Mon. Wea. Rev., 104, 233-248.

Shukla, J., and B. Bangaru, 1981: Effect of a Pacific sea surface temperature anomaly on the circulation over North America: A numerical experiment with the GLAS model. (in press).

Shukla, J., and Y. Sud, 1981: Effect of cloud-radiation feedback on the climate of a general circulation model. J. Atmos. Sci., 2337-2353.

Simmons, A.J., and B. Hoskins, 1980: Barotropic influence on the growth and decay of nonlinear baroclinic waves. J. Atmos. Sci., 37, 1679-1684.

Simpson, R.W., and W.R. Downey, 1975: The effect of a warm midlatitude sea surface temperature anomaly on a numerical simulation of the general circulation of the southern hemisphere. Quart. J. Roy. Met. Soc., 101, 847-867.

Smith, E.A., T.H. Vonder Haar, and J.R. Hickey, 1982: The nature of the short period fluctuations in solar irradiance received by the earth. to be published in J. of Climatic Change.

Starr, V.P., 1951: Applications of energy principles to the general circulation. Compendium of Meteorology, Malone, T.F., (ed.), Amer. Met. Soc., Boston, Mass., 568-574.

Stephens, G.L. G.G. Campbell, and T.H. Vonder Haar, 1981: Earth radiation budgets. J. of Geophys. Res., 86, 9739-9760.

Stephens, G.L., and P.J. Webster, 1981: Clouds and climate: sensitivity of simple systems. J. Atmos. Sci., 38, 235-247.

Stoekenius, T., 1981: Interannual variations of tropical precipitation patterns. Mon. Wea. Rev., 109, 1233-1247.

Stone, A.M., and S. Manabe, 1968: Comparison among various numerical models designed for computing infrared cooling. Mon. Wea. Rev., 96, 735-74[illegible].

Swanson, G.S., and K.E. Trenberth, 1981a: Trends in the southern hemisphere tropospheric circulation. Mon. Wea. Rev., 109, 1879-1889.

Swanson, G.S., and K.E. Trenberth, 1981b: Interannual variability in the southern hemisphere troposphere. Mon. Wea. Rev., 109, 1890-1897.

Trenberth, K.E., 1976: Spatial and temporal variations of the southern oscillation. Quart. J. R. Met. Soc., 102, 639-653.

Trenberth, K.E., 1980a: Atmospheric quasi-biennial oscillations. Mon. Wea. Rev., 108, 1370-1377.

Trenberth, K.E., 1980b: Planetary waves at 500 mb in the southern hemisphere. Mon. Wea. Rev., 108, 1378-1389.

Trenberth, K.E., 1981: Interannual variability of the southern hemisphere 500 mb flow: Regional characteristics. Mon. Wea. Rev., 109, 127-136.

Troup, A.J., 1965: The Southern Oscillation. Quart. J. Roy. Meteor. Soc., 98, 490-506.

Tung, K.K., and R.S. Lindzen, 1979: A theory of stationary long waves. Part I: A simple theory for blocking. Mon. Wea. Rev., 107, 714-734.

Van Loon, H., and R.A. Madden, 1981: The southern oscillation. Part I: Global associations with pressure and temperature in northern winter. Mon. Wea. Rev., 109, 1150-1162.

Van Loon, H., and J.C. Rogers, 1978: The seasaw in winter temperatures between Greenland and Northern Europe. Part I: General description. Mon. Wea. Rev., 106, 296-310.

Van Loon, H., and J.C. Rogers, 1981a: The southern oscillation. Part II: Associations with changes in the middle troposphere in the northern winter. Mon. Wea. Rev., 109, 1163-1168.

Van Loon, H., and J.C. Rogers, 1981b: Remarks on the circulation over the southern hemisphere in FGGE and on its relation to the phases of the southern oscillation. Mon. Wea. Rev., 109, 2255-2259.

Vernekar, A.D., 1975: A calculation of normal temperature at the earth's surface. J. Atmos. Sci., 32, 2067-2081.

Vernekar, A.D., 1981: Response of the steady state model for quasi stationary perturbations to simulated anomalies at the earth's surface. J. Atmos. Sci., 38, 531-543.

Walker, G.T., 1923: Correlation in seasonal variations of weather VIII. Mem. Ind. Meteor. Dept., 24, 75-131.

Walker, G.T., 1924: World weather IX. Mem. Ind. Meteor. Dept., 24, 275-332.

Walker, G.T., 1928: World weather III. Mem. Ind. Meteor. Dept., 17, 97-106.

Walker, G.T., and E.W. Bliss, 1932: World Weather V. Mem. Roy. Meteor. Soc., 4, 53-84.

Wallace, J.M., and D.S. Gutzler, 1981: Teleconnections in the geopotential height field during the Northern hemisphere winter. Mon. Wea. Rev., 109, 784-812.

Wang, W.C., W.B. Rossow, M.W. Yao, and M. Wolfson, 1981: Climate sensitivity of a one-dimensional radiative convective model with cloud feedback. J. Atmos. Sci., 38, 1167-1178.

Webster, P.J., 1981: Mechanisms determining the atmospheric response to sea surface temperature anomalies. J. Atmos. Sci., 38, 554-571.

Webster, P.J., 1982: Seasonality in the local and remote atmospheric response to sea surface temperature anomalies. J. Atmos. Sci., 39, 41-52.

Wetherald, R.T., and S. Manabe, 1972: Response of the joint ocean-atmospheric model to the seasonal variation of the solar radiation. Mon. Wea. Rev., 100, 42-59.

Wetherald, R.T., and S. Manabe, 1980: Cloud cover and climate sensitivity. J. Atmos. Sci., 37, 1485-1510.

Wielicki, B. and M. Hendershott, 1979: Further development of a spectrally truncated model atmosphere for climate studies. Dyn. Atmos. and Oceans, 3, 453-464.

Wyrtki, K. 1975: El Nino - the dynamic response of the equatorial Pacific Ocean to atmospheric forcing. J. Phys. Oceanogr., 5, 572-584.

APPENDIX I

The Solution of the Surface Thermal Energy Balance Equation

The steady-state surface thermal energy balance is represented by (2.39)

$$S_s = \varepsilon_s B T_g^4 + Q_s + Q_e + I(T_g - 271.2),$$

where

$$Q_s = \rho_s c_p c_d |v_s| (T_g - T_a),$$

and $Q_e = L \rho_s c_d |v_s| GW(q_s(T_g) - h\, q_s(T_a))$.

We define I_1 and I_2 such that

$$I_1 = \rho_s c_p c_d |v_s|$$

and

$$I_2 = L \rho_s c_d |v_s|.$$

The above equation can be written in the form

$$F(T_g) = S_s - \varepsilon_s B T_g^4 - I_1(T_g - T_a) - I_2(q_s(T_g) - hq_s(T_a)) - I(T_g - 271.2). \qquad (A1.1)$$

(A1.1) is solved for T_g, using Newtons iteration method.

Differentiating (A1.1) with respect to T_g we obtain

$$F'(T_g) = -4\varepsilon_s B T_g^3 - I_1 - I_2 - q_s(T_g) - I. \qquad (A1.2)$$

To calculate the saturation mixing ratio, $q_s(T_g)$, and its derivative, $q'(T_g)$, we use a formula for the saturation vapor pressure, e_s (Bolton, 1979). This formula provides an accuracy of 0.1% in the range -30°C < T_g < 35°C.

$$e_s(T_g) = 6.112 \exp (17.67 (T_g - 273.15)/(T_g - 29.65)) \qquad (A1.3)$$

$$q_s(T_g) = \frac{.622\ e_s(T_g)}{p - e_s(T_g)} \qquad (A1.4)$$

Differentiating (A1.4) with respect to T_g,

$$q_s'(T_g) = \frac{q_s p e_s'(T_g)}{(P - e_s)} \qquad (A1.5)$$

and using (A1.3), one obtains

$$e_s'(T_g) = \frac{17.67 \times 243.15}{(T_g - 29.65)^2} \quad . \qquad (A1.6)$$

Substituting (A1.5) into (A1.2), we arrive at

$$F'(T_g) = - 4\varepsilon_s B T_g^3 - I_1 - I_2 \frac{q_s P \times 4302.645}{(p-e_s(T_g))(T_g-29.65)^2} - I. \qquad (A1.7)$$

Using (A1.1) and (A1.7), the solution is convergent in the form

$$T_g^{v+1} = T_g^{v} - \frac{F(T_g^{v})}{F'(T_g^{v})}, \qquad (A1.8)$$

where the superscripts v and v+1 indicate successive iteration steps. Iteration is performed until $F(T_g)$ is less than a small, predetermined value.

APPENDIX II

Spectral Transform of $(\nabla \cdot f\nabla\chi)$

The term $(\nabla \cdot f\nabla\chi)$ can be expanded in the form

$$\nabla \cdot f\nabla\chi = \nabla f \cdot \nabla\chi + f\nabla^2\chi.$$

Since $f = 2\Omega\mu$,

$$\nabla \cdot f\nabla\chi = \frac{2\Omega}{a^2}(1-\mu^2)\frac{\partial\chi}{\partial\mu} + 2\Omega\mu\nabla^2\chi. \tag{A2.1}$$

If we expand χ in terms of spherical harmonics defined by (2.60), then

$$\nabla \cdot f\nabla\chi = \frac{2\Omega}{a^2}\sum_m\sum_n \chi_n^m (1-\mu^2)\frac{\partial Y_n^m}{\partial\mu} - \frac{2\Omega}{a^2}\sum_m\sum_n n(n+1)\chi_n^m \mu Y_n^m, \tag{A2.2}$$

or

$$\nabla \cdot (f\nabla\chi) = \frac{2\Omega}{a^2}\sum_m\sum_n \chi_n^m \{-(n^2-1)D_n^m Y_{n-1}^m - n(n+2) D_{n+1}^m Y_{n+1}^m\}, \tag{A2.3}$$

where we have used the two recurrence relations

$$(1-\mu^2)\frac{\partial Y_n^m}{\partial\mu} = (n+1) D_n^m Y_{n-1}^m - n D_{n+1}^m Y_{n+1}^m, \tag{A2.4}$$

and

$$\mu Y_n^m = D_{n+1}^m Y_{n+1}^m + D_n^m Y_{n-1}^m, \tag{A2.5}$$

with

$$D_n^m = \left(\frac{n^2-m^2}{4n^2-1}\right)^{\frac{1}{2}}$$

Applying the transform operator (2.63) on (A2.3), we obtain

$$(\nabla \cdot f\nabla\chi)_n^m = \frac{-2\Omega}{a^2}(n(n+2) D_{n+1}^m \chi_{n+1}^m + (n^2-1) D_n^m \chi_{n-1}^m). \tag{A2.6}$$

APPENDIX III

The Simulated Zonal Wind for February

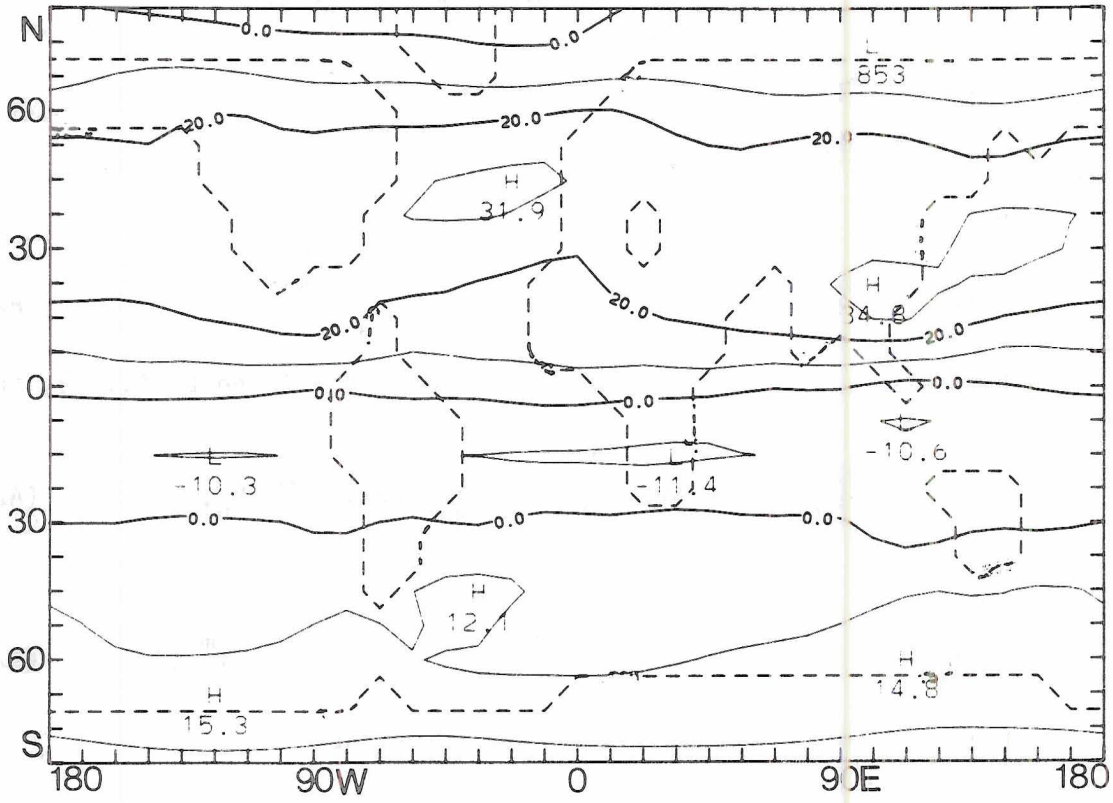

A.1 The simulated zonal wind (m sec^{-1}) for February.